Multiparticle Correlations in π^+p and K^+p Interactions at 250 GeV / c

Martine Charlet

Multiparticle Correlations in π^+p and K^+p Interactions at 250 GeV/c

Multiparticle Correlations in π^+p and K^+p Interactions at 250 GeV/c

Een wetenschappelijke proeve op het gebied
van de Natuurwetenschappen.

Proefschrift

ter verkrijging van de graad van doctor
aan de Katholieke Universiteit Nijmegen,
volgens besluit van het College van Decanen
in het openbaar te verdedigen
op dinsdag 31 mei 1994,
des namiddags te 3.30 uur precies,

door

Martine Charlet

geboren op 27 oktober 1966 te Deurne (België).

CopyPrint 2000, Enschede
1994

Promotor: Prof. Dr. E.W. Kittel

ISBN 90-9007108-3

Bij dezen wens ik eenieder die op enerlei wijze heeft bijgedragen tot het totstandkomen van dit proefschrift te bedanken. In het bijzonder:

- Frans Verbeure, voor de geboden kans om te promoveren;
- Wolfram Kittel, voor de hulp bij het waarmaken van deze kans;
- Eddi De Wolf en Frank Botterweck, voor de vele zinvolle discussies en suggesties;
- Annelies Oosterhof, voor het aangename gezelschap tijdens het schrijfwerk;
- Erna Dikmans en Marjo van Wees, voor de administratieve hulp;
- Mijn collega's, voor de leuke babbels;
- "Gang 64", voor de gezelligheid in de late uurtjes;
- "De Waereld In", voor de muzikale vrijdagavonden en de instandhouding van mijn Antwerpse geplogenheden;
- Mijn ouders, bomma en tante Mona, voor de morele steun.

Contents

1

Introduction

At present, the four basic forces acting on matter are known to be: gravitation, electromagnetic interaction, weak intereaction and strong interaction. The mediators of these forces are: the graviton, the photon, weak vector bosons (3) and gluons (8); respectively. In situations considered in high-energy physics, gravity is very weak compared to the other forces and is, therefore, left aside. The electromagnetic force acts on all particles carrying an electric charge. Hadrons (particles built from quarks q and/or antiquarks $\bar{q}$) and leptons (electron e^-, muon μ^-, tau lepton τ^-; neutrinos ν_e, ν_μ and ν_τ; and the corresponding antiparticles) undergo the weak interactions, whereas hadrons in addition feel the strong forces. The electromagnetic and the weak interactions are described by electroweak dynamics, the strong interactions by quantum chromodynamics (QCD). Electroweak dynamics and quantum chromodynamics together form the standard model of high-energy physics.

Although experiments continue to confirm the standard model, there are still a number of problems left. The formalism of QCD is very complex and usually exact calculations are impossible. Perturbative calculations are only valid in the region of large momentum transfer. If, for example, an electron and a positron collide and annihilate into a quark-antiquark pair, this $q\bar{q}$-pair will cause the creation of new partons ($q\bar{q}$-pairs and gluons) in a shower-like manner. This so-called parton shower can be analyzed perturbatively. The next stage in the multiparticle production process is hadronization, where hadrons are formed from the partons. In this phase, unfortunately, perturbative QCD is not valid.

In this thesis, interactions of two hadrons are considered. Such an interaction can be pictured as the collision of two bags filled with partons. Although it is not clear how the quarks of the two hadrons interact in detail, one expects that at a certain level of the multiparticle production process a situation occurs very much alike that at the end of a parton shower. After this level is reached, hadronization sets in and observable particles are formed.

Since QCD does not yield a full understanding of the multiparticle production process, phenomenological methods have to be used to gain insight. Correlation studies are very well suited for this task, since correlations reflect the detailed dynamics involved. In early days (ca. 1973) this kind of studies booked a number of successes in establishing fundamental concepts of hadrodynamics. After some period of stagnation, the field was revived by the introduction of the concept "intermittency" in particle physics.

The story of intermittency in high-energy physics starts with the discovery of the exceptional JACEE cosmic-ray event in 1983 [JACE83]. This Si + AgBr event (4 TeV/nucleon), observed in a balloon-borne emulsion chamber, has the unusually high multiplicity of 1015 charged particles. The highest peak in the pseudo-rapidity distribution of this event (Fig. 1.1a) is three times as high as the average value. This high density of particles in such a small phase-space domain is called a spike. Exited by the occurrence of this special event, Białas and Peschanski [BPNP86, BPNP88] proposed a method to investigate density fluctuations and showed how dynamical fluctuations could be separated from statistical noise. The authors are, however, not the first ones to analyse event-to-event fluctuations. Already in 1973 Lundlam and Slansky [TLRS73] compared rapidity distributions of single events with the sample averaged distribution. This had yielded evidence for strong clustering effects in longitudinal phase space. Fluctuations in individual events were also considered in the context of Reggeon theory [ABRA73].

Białas and Peschanski [BPNP86, BPNP88] suggested that spikes could be a manifestation of "intermittency", a term borrowed from fluid dynamics. Fully developed turbulance, for example, occurs with self-similar energy dissipation at ever-decreasing regions of phase space. According to [BPNP86, BPNP88] the occurence of intermittency in particle production leads to large density fluctuations exhibiting self-similarity with respect to the size of the phase-space volume.

With the discovery of its own spike event [NA2287], NA22 joined the intermittency venture in an early stage. This event has charged multiplicity 25 while the average multiplicity is only eight. Ten out of the 25 charged particles form a dense cluster contained in a rapidity bin of 0.1. This shows up in the rapidity distribution (Fig. 1.1b) as a peak of height 60 (!) times the average.

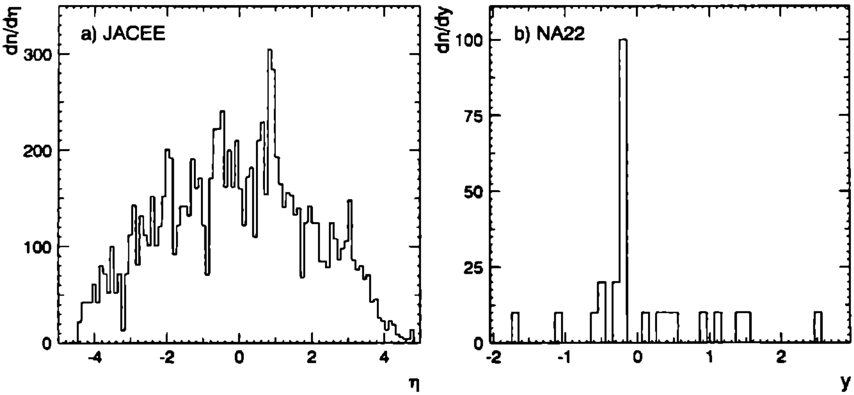

Figure 1.1: *(Pseudo-) rapidity distibution of two events with unusually high local density, the JACEE cosmic-ray event and the NA22* π^+p *event.*

This thesis is a journey along the intermittency route followed by NA22. Some results earlier obtained by Botterweck [FBTH92] are included briefly where neccesary to maintain the continuity of the story. The different phases of the evolution of the subject are presented in a chronological order. After the presentation of the experimental environment in chapter 2, the formalism in one dimension and its application to the NA22 data are covered in chapter

3. The extension to higher dimensions is treated in chapter 4. Chapter 5 contains the improvement of the original formalism to an optimal framework for the analysis of densities and correlations. A comprehensive review including results from other experiments on all types of interactions can be found in [WDKR93].

Bibliography

[ABRA73] V.A. Abramovskii, V.N. Gribov, O.V. Kancheli, Yad. Fiz. **18** (1973) 595; V.A. Abramovskii, V.N. Gribov, O.V. Kancheli, Sov. J. Nucl. Phys. **18** (1974) 308.

[BPNP86] A. Białas and R. Peschanski, Nucl. Phys. **B273** (1986) 703.

[BPNP88] A. Białas and R. Peschanski, Nucl. Phys. **B308** (1988) 857.

[FBTH92] F. Botterweck, Ph.D. Thesis, Univ. of Nijmegen (1992).

[JACE83] T. Burnet et al. (JACEE), Phys. Rev. Lett. **50** (1983) 2062.

[NA2287] M. Adamus et al. (NA22), Phys. Lett. **B185** (1987) 200.

[TLRS73] T. Lundlam and R. Slansky, Phys. Rev. **D8** (1973) 1408;
J. Hanlon et al., Phys. Lett. **B46** (1973) 415;
R. Slansky, Phys. Rep. **C11** (1974) 99.

[WDKR93] E. De Wolf, I. Dremin and W. Kittel, "Scaling laws for density correlations and fluctuations in multiparticle dynamics", HEN-362 (1993), IIHE-93.01, FIAN/TD-09/93.

2

Experimental environment

This chapter gives an outline of the experimental set-up, shortly describes the data reconstruction and explains the event and track selection criteria.

2.1 Experimental set-up

The experimental data used for the analysis presented in this thesis, were obtained by the NA22 collaboration in the European Hybrid Spectrometer (EHS). The experimental set-up was situated in the North Area (NA) of the Super Proton Synchrotron (SPS) at CERN. It was active during two running periods: the first period (run A) in June and July of 1982 and the second one (run B) in July and August of 1983.

The adjective hybrid in the name EHS refers to two characteristics of the spectrometer:

- the visual detection of the interaction with a bubble chamber (RCBC),
- the use of counter devices for the measurement of the incident beam particle and the particles produced in the collision in RCBC.

The set-up consists of the following important components:

- upstream wire chambers and Čerenkov counters,
- RCBC,
- a two-lever-arm momentum spectrometer,
- particle identification detectors,
- a superconducting magnet M1 and a conventional C-shaped magnet M2,
- a trigger system.

The main part of the EHS layout is shown schematically in Fig. 2.1. The positive x-axis of the right-handed coordinate system points along the beam direction and the y-axis upwards.

In the following sections, a brief description of the main parts of EHS is given. More details can be found in the proposal [PROPOS] and in [AGBE83].

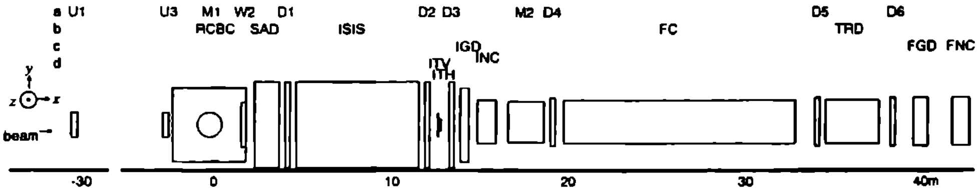

Figure 2.1: *The layout of the NA22 experiment. The top line (marked with a), indicates the devices used for charged-particle momentum reconstruction. Line b shows the charged-particle identification detectors, line c the neutral-particle detectors, and the last line, d, marks the trigger devices. The coordinate system, and the beam direction are indicated on the left.*

2.1.1 The beam

The primary SPS beam of 400 GeV/c protons is collided on a beryllium target, positioned 600 m upstream of EHS, from which a 250 GeV/c positive beam is extracted. This secondary beam has a statistical spread of $\Delta p/p = 0.3\%$ and an uncertainty in the nominal value of $\Delta p/p = 0.5\%$. To enrich the meson content, the beam is passed through a filter of 5.5 m polyethylene with an absorption length shortest for protons and longest for kaons. Unfortunately, this procedure also increases the muon background to 27%. The hadronic beam component (73%) is turned into 45.8% protons, 38.9% pions and 15.3% kaons. Behind the polyethylene filter, the beam is focused in the z-direction such that the minimum width is obtained 12.5 m behind the bubble chamber where the trigger elements ITH and ITV (see below) are installed.

The beam particles are tagged by two differential Čerenkov counters (CEDARs) positioned 150 m upstream (not shown on Fig. 2.1). One of them is adjusted to give a signal for 250 GeV/c kaons, the other for 250 GeV/c pions. Part of the time, the second one was adjusted to tag 250 GeV/c protons. Data on pp interactions were mainly taken for calibration purposes [FMTH87, VHTH87, POWE82, LSTH88, DRTH88] and are not used in this analysis. The discrimination efficiency of the CEDARs is 100% and their detection efficiency 75%.

The beam coordinates are obtained from two small upstream multiwire proportional chambers U1, U3 and from the bubble chamber RCBC.

The intensity of the secondary beam at the entrance of RCBC is 20 000 particles/second. In order to obtain clear pictures, one has to minimize the number of irrelevant tracks passing through RCBC. Therefore, a kicker magnet is used to deflect the beam particles after a collision trigger took place and the bubble chamber is still sensitive. A chopper is placed in the beam line to reduce the background during the insensitive time of RCBC.

Further details on the beam can be found in [ATYR80].

2.1.2 RCBC

The abbreviation RCBC stands for Rapid Cycling Bubble Chamber. The advantages of using a bubble chamber are:

- since the nuclei of the liquid (see below) can be used to study interactions on them, the bubble chamber serves as target,
- 4π angular acceptance,
- good track resolution around the vertex, ensuring the number of tracks leaving the vertex and the vertex position itself to be well known,
- good momentum resolution of slow tracks,
- detection of decays of neutral (strange) particles by their decay mode,
- detection of γ-conversions,
- identification of slow charged particles from the ionization strength.

So, a bubble chamber serves as a target, a vertex detector, a track detector and an identification detector.

The RCBC is a vessel filled with liquid H_2 kept under an overpressure at a temperature of 25°K, slightly below the boiling temperature. The pressure is released by an expansion mechanism and the liquid becomes superheated. When a charged particle passes through the hydrogen, it ionizes the atoms along its track. During the expansion time, the liquid starts to boil around these ions and bubbles are formed along the ionized track. The bubbles are allowed to grow till they are large enough, about 0.25 mm, to be detected by the optical system. At this moment, three stereographic pictures are taken, the hydrogen is recompressed and the bubbles collapse.

The bubble chamber is called rapid cycling because the cycle can be repeated 30 times per second. The running frequency during data taking, however was only 15 Hz to optimize synchronization with the camera system. In one cycle, the bubble chamber is sensitive during 0.5 ms for run A and 1.0 ms for run B.

The RCBC has the form of a cylinder, with the axis along the z-axis. Its diameter is 85 cm, from which 70 cm is fiducial volume, and the depth is 40 cm. The exit window of RCBC consists of 1.6 mm stainless steel, the vacuum tank window of 1 mm Al and 2 mm glass reinforced plastic. The chamber is equipped with three cameras under a 21° stereo angle, to allow a three-dimensional reconstruction of the interaction. The cameras are positioned behind a glass shield, at 16° with respect to the z-axis.

The main target in the experiment are the nuclei of the H_2 liquid in the bubble chamber. Such a nucleus is just a single proton. For the study of interactions on nuclei, two thin metal foils, one of 1.6 mm Al one of 0.4 mm Au (consistent with about 0.5% of an interaction length), are installed inside the bubble chamber, 15.5 cm behind the entrance window. In this thesis, only interactions on protons are investigated.

The RCBC is embedded in the magnetic field of the superconducting magnet M1 of 2.0 T, the magnetic field points in the negative z-direction. This causes a momentum dependent curvature of the charged tracks. For slow tracks, $p_{lab} < 2$ GeV/c, this curvature is strong enough to allow a precise momentum measurement. To measure higher momenta, additional information from the downstream spectrometer (Sect. 2.1.3) is needed.

The energy loss of a charged particle in the hydrogen of the bubble chamber, due to the electromagnetic interaction of the moving particle with the atoms in matter, depends on the velocity of the particle and can be determined from the density of the bubbles along the track. Particles with the same momentum but different mass have different velocity and consequently a different bubble density. In RCBC these differences are large enough to distinguish

- electrons from other particles if $p_{lab} < 0.2$ GeV/c
- pions, kaons and protons if $p_{lab} < 0.7$ GeV/c
- pions and kaons from protons if $p_{lab} < 1.2$ GeV/c

The two-track resolution in the bubble chamber is determined by the size of the bubbles and equals the size of two bubbles next to each other, i.e. 0.5 mm. However, if fast tracks are exactly overlapping in the bubble chamber, they appear as one track with ionization twice minimum or more. In the data reconstruction (Sect. 2.2) high-momentum tracks with ionization two or more are allowed to be matched with more than one track in the downstream spectrometer (Sect. 2.1.3). This procedure leads to a very good two-track resolution, necessary for the analysis described in this thesis.

2.1.3 The downstream spectrometer

The collision probabilities for π^+, K^+, p^+ on p in the 70 cm fiducial volume are respectively 6.3%, 5.3%, 10.5%. In total 65% of the produced particles enter the downstream part of the spectrometer.

The downstream spectrometer is designed to improve the momentum measurement of tracks faster than 2 GeV/c. For these momenta the curvature in RCBC is not strong enough to allow an accurate momentum measurement with solely the information from the bubble chamber.

The spectrometer consists of two lever arms, separated by a conventional C-shaped magnet M2. During run A (B) M2 had a magnetic field of 1.5 T (0.75 T) in same (opposite) direction as the field of M1. The change between the two runs was made to improve geometrical acceptance for tracks of intermediate momentum (between 20 and 50 GeV/c), although it slightly deteriorated the momentum resolution of fast tracks (more than 50 GeV/c).

The first lever arm contains a multiwire proportional chamber W2 and three drift chambers D1, D2 and D3. W2 is used to match the tracks leaving RCBC with those passing through the drift chambers.

In the center of the magnet M2, an aperture allows particles with momentum above 20 GeV/c to enter the second lever arm. This consists of the three drift chambers D4, D5 and D6.

Together with RCBC, the spectrometer gives an average momentum resolution $\Delta p/p$ varying from a maximum of 2.5% at 30 GeV/c to around 1.5% above 100 GeV/c. For most of the charged particles $\Delta p/p < 3\%$.

2.1.4 Particle identification devices

2.1.4.1 Charged particle identification

The identity of a charged particle is determined from an independent measurement of velocity and momentum of that particle.

1. The velocity can be obtained from electromagnetic processes as:
   - Čerenkov radiation (when a charged particle moves faster than the speed of light in the material it traverses, it emits photons at an angle depending on the velocity of the particle and the refractive index of the medium),
   - velocity dependent energy loss of a charged particle traversing a medium,
   - transition radiation (when a highly relativistic charged particle crosses the boundary between two media with different dielectric constant, it will emit an amount of energy depending on the velocity of the particle).
2. The momentum of the charged particle is calculated from its deflection measured in a magnetic field.

With the knowledge of the momentum and the velocity of the particle, different mass hypotheses can be tested.

Besides RCBC (see Sect. 2.1.2), four devices are used for the identification of charged particles in different momentum ranges.

1. **SAD** ([FERN84]) is a silicon aerogel Čerenkov Counter placed just behind M1. It is used to identify charged particles with momentum between 0.5 and 4 GeV/c. Faster particles can pass undisturbed through its central hole. The silicon refractive index of 1.031 corresponds to threshold momenta of 0.56 2.0 and 3.8 GeV/c for π, K and p, respectively.
2. **ISIS** ([ALLI84]) stands for Identification of Secondaries by Ionization Sampling. It is a large pictorial drift chamber used for charged particle identification in the momentum range 2 to 30 GeV/c by sampling the ionization of each track many times along this track, simultaneously for a large number of tracks. The main task of ISIS is particle identification, but its information can also be used for the geometrical reconstruction of the tracks. With ISIS, the following particles can be separated:
   - e/π in the momentum range 2 to 25 GeV/c,
   - π/K in the momentum range 4 to 30 GeV/c,
   - K/p in the momentum range 7 to 30 GeV/c.
3. **FC** ([ALBE84]), the abreviation of Forward Čerenkov, positioned just behind D4, is a large hot multicell Čerenkov counter filled with He. The refractive index of the heated He equals 1.000018, corresponding to the high-momentum threshold values of 24, 82 and 156 GeV/c for π, K and p, respectively.
4. **TRD** ([COMM80]) is a Transition Radiation Detector posted right behind D6. The TRD contains stacks of loosely packed carbon fibres as radiator, each stack followed by a Xenon proportional wire chamber to measure the amount of energy. A separation between π/K and p from 80 GeV/c onwards, improving with increasing momentum, is provided.

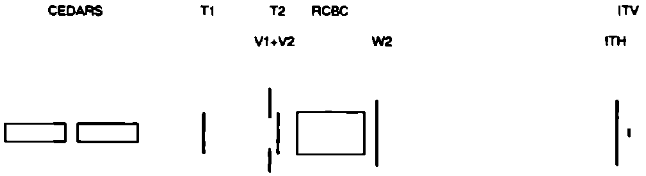

Figure 2.2: *The NA22 trigger components, seen from above.*

2.1.4.2 Neutral particle identification

To detect neutral particles, the EHS is equipped with four calorimeters. Such a device measures the energy of a particle from the shower it initiates when interacting with material.

In each lever arm, one calorimeter is dedicated to the detection of photons (γ-detectors) and, right behind it, one to the detection of hadrons.

The γ-detectors are called IGD and FGD [POWE82], intermediate and forward gamma detector, and consist of lead-glass blocks. The hadron calorimeters are called INC and FNC [AGBE80], intermediate and forward neutral calorimeter, and are made of iron-scintillator sandwiches. The calorimeters are designed in such a way that they allow both energy and position measurement.

The intermediate calorimeters are positioned in front of M2 and are provided with a central hole to allow fast particles to pass undisturbed into the second lever arm. The hole is covered by the forward calorimeters at the end of the spectrometer.

Since the γ-detectors are positioned just in front of the hadron calorimeters, it is possible for a hadron to interact with the corresponding γ-detector. However, the interaction length for this process is much longer than that for the photon interaction. Therefore, only part of the hadrons will start showering and even then usually only part of the energy will be absorbed by the γ-calorimeter. Nevertheless, for the reconstruction of the hadron energy one needs to combine the information of both the photon and the hadron calorimeter.

Also charged hadrons interact with the hadron calorimeters. Since their tracks are reconstructed very accurately through the wire and drift chambers and no improvement can be expected, this extra information is used only to veto calorimeter showers for non-neutral particles.

2.1.5 The interaction trigger

To minimize the collection of useless data and to reduce the scanning task, a trigger is applied which discriminates non- and wrongly-interacting beam particles from those interacting inside the vertex detector. If an interaction is considered interesting, the optical control system is ordered to take pictures of the bubble chamber and the information of the electronic devices is stored on magnetic tapes.

The trigger ([DRLV82, ADAM86, BERG81]) (Fig. 2.2) is designed to be sensitive to most of the total cross section and is, therefore, called a minimum-bias trigger. It consists of four levels with a hierarchical structure.

- The **Level 0** trigger consists of two parts: The experiment-ready signal equaling "true" when all essential detectors and readout systems are ready and the beam trigger composed of four scintillation counters (T1, T2, V1 and V2) placed upstream. The beam is defined by coincident hits in T1 and T2. The veto counters V1 and V2 reject upstream interactions. The logical condition for this level is given by

$$T_1 \wedge T_2 \wedge \overline{(V_1 \vee V_2)} \wedge \text{Exp. Ready} \quad . \tag{2.1}$$

- The **Level 1** trigger checks if the beam particle has indeed interacted. It contains the hodoscopes ITH and ITV, placed 12.5 m downstream, at the horizontal focus of the beam. ITH is an array of horizontal scintillator strips. ITV consists of two scintillator planes separated by a vertical scintillator strip and is installed such that most of the non-interacting beam particles will hit the central strip ITV(2). An event is accepted when at least two tracks are seen in ITH or no track is seen in ITV(2). When a lot of particles are produced it might happen that only one or no particle is fast enough to reach the hodoscopes. Then ITV(2) is not hit and the interaction is accepted. The logical condition for an interaction looks like

$$\overline{ITV(2)} \vee ITH(n \geq 2) \quad . \tag{2.2}$$

- The **Level 2** trigger vetoes interactions downstream of W2 and uses the CEDAR signals C1 and C2, that arrive too late for level 0 and 1. If an interaction took place downstream of W2, very few hits are seen in W2 (less than three in planes 1 and 6), but a lot more in ITH (more than one). The logic of this trigger can be written as

$$\overline{(ITH(n > 1) \wedge \sum_{1,6} W2(n < 3))} \wedge (C1 \vee C2) \quad . \tag{2.3}$$

- The **Level 3** trigger is an Optical Fiducial Volume Trigger (OFVT) [ANDE84]. It limits the maximum number of beam tracks entering the bubble chamber to 20, in order to obtain cleaner pictures without biasing the sample. This level of the trigger was not necessary for run B.

Detailed studies have been performed to calculate the trigger efficiencies depending on the event shape [DRFV83, SEVE86]. The main losses occur for low-multiplicity events (two and four prongs) with only one fast particle. A procedure to correct for these losses is described in [VHTH87, DRTH88].

2.2 Data reconstruction

Even with the use of an interaction trigger, the total amount of data obtained during the two experimental runs is enormous: 170 high-density magnetic tapes and about 150 km bubble-chamber film. These raw data have to be converted into (six) Data Summary Tapes (DST), containing only physical parameters of interest. Therefore, a long and complex chain of programs is used to reconstruct the events completely and to determine the four-momentum vector for each detected particle ([VHTH87, FMTH87, DRTH88]).

2.2.1 Scanning and measuring

The bubble-chamber film is divided into 85 parts, called rolls. A frame is defined as the set of three stereo views of an event. Each frame is examined by eye, a process called scanning [NA2283, NA2284]. This scanning happens in a restricted fiducial volume of 70 cm on at least two views. On each event, two independent scans are performed and in case of disagreement, a third decisive scan.

From the information of the upstream wire chambers U1 and U3, the program PREDICT is able to reconstruct the triggering beam track. The program predicts the y- and z-coordinates for a fixed x-position and calculates the projection on the three views. Using this result, the scanner first searches for the interacting beam track.

If, after all, the track turns out to stem from a beam particle not interacting in the fiducial volume, the frame is rejected. Other classes of discarded pictures are: upstream interactions, bad quality pictures (too dark or too faint), interactions inside the small area around the Al and Au foils, pictures with too many beam tracks passing through RCBC, frames of which less than two views are measurable.

For each event accepted for further processing, roll and frame number are recorded, the primary vertex is measured precisely and the scan topology is determined. The scan topology contains information on the number of charged tracks leaving the primary vertex, decays of (neutral or charged) secondary tracks, γ-conversions, and so on.

Furthermore, a track can show a certain characteristic and is given a corresponding label:

S	possibly stopping track	I	interaction on a charged track
P	stopping track, mostly very slow protons	N	interaction on a neutral track
R	π-μ-e decay	D	decaying charged particle track (kink)
E	electron (or positron)	X	track from a confused region
V	neutral decay		

After scanning, the event is measured [HGFC84]. For each view, two-dimensional coordinates are recorded for 18 fiducial marks, for the vertices and for (on average) 20 points along each track.

The programs SCANLOAD and SCANSYNCHRO transform the data obtained from scanning and measuring to the HYDRA event structure used.

2.2.2 Geometrical reconstruction

The program PRECIS reads the raw scanning and measuring data from tape. The information from the spectrometer and from all detectors, except ISIS, belonging to a particular event is selected and added to the HYDRA event structure.

The signals of ISIS are transformed into ISIS tracks by the pattern recognition program SPIRES. Also this information is added to the event structure.

The HYDRA event structure is used as input for GEOHYB, the largest and most complex program of the chain. It is responsible for the three-dimensional reconstruction of vertices and tracks in RCBC and and the spectrometer. For each detected particle, the trajectory and the momentum have to be determined.

The GEOHYB program consists of following parts:

A) Vertices in RCBC are geometrically reconstructed from the measurements on the different views. Track fits are performed on the points on each view to determine the track curvature, RMS of the measured points, etc. Furthermore, these fits allow to improve the knowledge of the vertex position and to hook (match) bubble-chamber tracks with spectrometer tracks.

B) The beam track is reconstructed.

C) The downstream spectrometer tracks are reconstructed. If the spectrometer track can be linked with an RCBC track, a global hybrid fit is performed. The track itself is called a hybrid track.

If no connection with a bubble-chamber track is found, the track is labeled hanging track. It could be a daughter of a neutral particle having decayed outside the visible region of RCBC.

D) RCBC tracks without an association to the spectrometer are reconstructed. To tracks with momentum $p_{lab} < 2$ GeV/c a mass-dependent fit is applied. For stopping tracks the momentum is obtained from the range-momentum relation.

Non-associated RCBC tracks are given two more chances to find a link with a spectrometer track. In the swim procedure, non-associated tracks are extrapolated from RCBC to the first lever arm wire chambers. Hits in the neighborhood of this prediction are picked up and part C is rerun with larger tolerances. If still no connection can be made, the rescue procedure tries to associate the extrapolated tracks with hanging tracks.

E) The HANGAR procedure checks if a hanging track could originate from a vertex downstream of RCBC. This information is input for the program HANG (see below).

F) The output is written on GST (Geometry summary tape) [CRIJ84].

The HANG program searches for additional neutral decays and conversions outside the bubble chamber. Two hanging tracks that seem to come from a common vertex are used in a mass-dependent kinematic fit [FCWF85].

2.2.3 Post geometrical reconstruction programs

All results obtained up till now are input for the program QUAL. In this procedure an event can be "improved" in two ways. Firstly, a bad or very suspicious track will be dropped if the number of reconstructed outgoing tracks is larger than the number of measured tracks. Secondly, in an event with wrong charge balance the charge of a track will be flipped if the error on curvature allows for this correction.

Furthermore, quality factors are assigned to the beam and all vertices and tracks. A beam labeled bad means that the measured event may not correspond to the beam track. The track quality factor depends on parameters as: track fit probability, $\Delta p/p$, RMS, etc. The quality of the vertices depends on the quality of tracks leaving the vertex. Precise rules for the assignment of quality factors are given in [HMSN84].

For the reconstruction of the electromagnetic avalanches in the γ-detectors, a program named GAMIN is used [VHTH87]. The signals of IGD and FGD are first treated separately and then combined to form possible decaying π^0's and η's.

The program NC analyses the information obtained from FNC and INC, and combines it with the information of the γ-detectors, since a hadron shower can already start in IGD or FGD. Signals from showers caused by charged tracks are removed and neutral-hadron showers are reconstructed.

Kinematic fits for neutral and charged strange particle decays and γ-conversions inside the bubble chamber are performed by the program called KINEM [LSTH88]. Also low-topology primary vertices are handled by this program for kinematic fitting.

The program PARTID uses the information of the identification detectors to determine confidence levels for the different mass hypotheses. In this procedure, a-priori probabilities (or particle densities) in the specific kinematic region are taken into account [FMTH87].

After reconstruction, the resulting event is compared with the event on film once more in the OUTPUT/IONIZATION SCAN [VHNN84]. The purpose of this action is twofold. On the one hand, the ionization strength of low-momentum tracks ($p_{lab} < 1.2$ GeV/c) is compared to that expected on the basis of various mass hypotheses in the geometry program (see also Sect. 2.1.2). On the other hand, this scan serves to clean up the sample and to detect biases due to possible shortcomings in the reconstruction program. At this point, it can be decided to remeasure an event or to consider the event to be unmeasurable. Sometimes, labels have to be changed or added if the characteristics were not or wrongly interpreted in the previous scans.

The last step in the data reconstruction chain is performed by the DSTMAKER. It produces the Data Summary Tape from the GST and merges the information obtained from the output/ionization scan.

2.3 Data sample

On basis of the qualities given by QUAL, different event samples can be selected [VHTH87, HMSN84]. The one used in the analyses presented is called p0bad and is briefly described in the following paragraphs. Another important sample, named pMbad, differs from p0bad in the number of tracks allowed to be lost in an event due to the selection criteria and thus in the number of events accepted for analysis. The influence of this difference on the intermittency analysis is investigated carefully in [FBTH92].

2.3.1 Event selection

The selection criteria are applied in the following ordered steps.

- **General cuts on event quality:** An event should be measured and reconstructed. The reasons for an event not to be measured, are given in Sect. 2.2.1. This is the largest part of rejected events, only a small number of events is lost in the reconstruction procedure.

- **Cuts on the beam quality:** Only events with a good beam track are accepted. The beam-track quality is considered to be good if the beam is reconstructed in the upstream wire chambers U1 and U3 and if at least 2 bubble-chamber track images are used in the fit procedure. Furthermore, the fit-probability parameter has to be better than 10^{-5} and the RMS should be less than 400 μm.

- **Cuts associated with the topology:** The number of tracks scanned and tracks reconstructed has to be the same. However, if there is just one reconstructed track too much and if it is of a very bad quality, it is allowed to be dropped in order to satisfy the first condition. No other track loss is allowed.

  Events with odd topology are rejected.

  The charge balance has to be correct. However, if the charge balance can be restored by flipping the charge of a track with large error on the curvature, the event is accepted.

  Events with an identified electron or positron ($p_{lab} < 200$ MeV/c see Sect. 2.1.2) are rejected. The reason for this rejection is that electrons can only occur in e^+e^- pairs. Usually, e^+e^- pairs originate from Dalitz decays or γ-conversions close to the vertex and should be excluded from the track sample. If one electron (positron) is detected, it is unknown which of the other tracks is the partner positron (electron); therefore, the entire event is discarded. However, if the electrons have a momentum higher than 0.2 GeV/c, they cannot be identified and the γ-conversion or Dalitz decay will survive. The influence of this bias is estimated in [FBTH92] and Sect. 5.2.2.3.

  The event should be free of bad tracks (see Sect. 2.3.2). However, a good track of momentum higher than 350 GeV/c can survive all the quality cuts. In that case, the event will be used, but this "un-physical" track will be dropped.

- **Selections on the event type:** Depending on specific physical characteristics, three event classes can be distinguished: elastic, single-diffractive and normal events. Only the third class, called inelastic non-single-diffractive events, is accepted for the analysis. Because of the different interaction mechanisms involved, the first two classes should be studied separately.

  An elastic event is defined as a two-prong event with missing-momentum restrictions $\Delta p_T < 0.1$ GeV/c and $\Delta p_L^{lab} < 9$ GeV/c.

  A single-diffractive events is defined as an event with a positive track of $x_F > 0.88$[1] with mass of the beam particle or of $x_F < -0.88$ with mass of the target particle. Furthermore, the total number of particles is less than eight.

After all the event cuts, the combined π^+p and K^+p sample consists of 59232 events.

2.3.2 Track selection

The six quality labels a track can be given are: Good, Acceptable, Interacting, Suspicious, Very Suspicious, Very Bad [NA2289]. Tracks belonging to the last four classes are called bad tracks.

The quality factor assigned to a track largely depends on the type of track. For tracks having received a special label during scanning and measuring (see Sect. 2.2.1), the following rules are applied.
R and E tracks are always accepted.
Heavily ionized *negative* S and P tracks are required to have $\Delta p/p < 0.10$.
I, D and X tracks have to have either $\Delta p/p < 0.10$ or $\Delta p/p < 0.25$ and sagitta $s > 4.5*\mathrm{RMS}$ to be accepted.

---

[1] Feynman x, $x_F = p_z/p_{max}$

A normal track is accepted when either $\Delta p/p < 0.10$ or $\Delta p/p < 0.25$ and sagitta $s >$ 4.5*RMS. Furthermore, it should be hybridized within strict matching criteria, unless it is completely measured in RCBC.

The reason tracks below "Acceptable" are rejected, is to make sure the sample is not biased by ghost tracks. GEOHYB can create two tracks out of one by combining two pairs of views separately. Usually, problems arise with the hybridization in this case, though badly measured tracks can be matched with anything. Slow tracks cannot be hybridized, therefore additional cuts on charge balance, event topology etc., are required. In this way, double counting of tracks can be virtually excluded.

2.3.3 Mass assignment

Since the intermittency analysis makes use of CMS variables, the mass of the particle has to be known to perform a correct transformation from the LAB frame to the CMS system. The particle identification devices described in sec. 2.1.4 in general work on a statistical basis. This does not matter for the investigation of inclusive single particle distributions. However, for correlation analysis their information would have to be used on a track-to-track basis. Therefore, in the investigation presented here, only the RCBC information is used for the particle identification. Particle masses are assigned according to the following ordered rules:

- negative particles:
    - if the track is given an electron scan label or if the ionization scan result gives a unique electron ⟶ electron mass
    - else ⟶ pion mass
- positive particles:
    - $p_{lab} > 150$ GeV/c ⟶ mass of beam particle
    - $p_{lab} > 1.2$ GeV/c ⟶ pion mass
    - $p_{lab} < 1.2$ GeV/c :
        - ionization scan is available[2]:
            - unique positron ⟶ positron mass
            - meson/proton ambiguity ⟶ pion mass
            - unique proton ⟶ proton mass
            - meson/proton ambiguity ⟶ automatic procedure
        - ionization scan is not available ⟶ automatic procedure:
            - track label is positron ⟶ positron mass
            - track label is pion decay ⟶ pion mass
            - track label is possible proton and a proton mass-fit exists ⟶ proton mass
            - $p_{lab} > 0.7$ GeV/c ⟶ pion mass
            - proton probability is 5% larger than pion probability ⟶ proton mass
            - anything else ⟶ pion mass

---

[2] ionizaton scan results are available for the full K^+p sample and for 62% of the π^+p sample

2.3.4 Weights

As mentioned before (Sect. 2.1.5), events are lost because of a "wrong" trigger signal. To correct for these losses, mainly due to the first two levels, trigger weights are introduced [VHTH87]. The first level trigger affects events with one fast track. Monte Carlo simulations provide x_F and p_T dependent weights to correct for this bias. Events with two or three fast tracks suffer from the second level trigger. For this event class, a trigger weight depending on the vertical position of fast track pairs at W2 is calculated.

Besides trigger weights also multiplicity weights C_n are used. They account for the overall passing rate and are calculated, after all event cuts have been applied, according to the topological inelastic cross section σ_n [ADAM86].

Let $W_{T,i}^n$ be the trigger weight of event i with multiplicity n and σ_n the cross section for multiplicity n (topological cross section). With N_n the number of events of multiplicity n, one defines

$$W_n = \sum_{i=1}^{N_n} W_{T,i}^n \tag{2.4}$$

and

$$\sigma = \sum_n \sigma_n \quad , \tag{2.5}$$

then the topology weight C_n is determined by

$$C_n = \frac{\sigma_n}{\sigma} \frac{\sum_n W_n}{W_n} \quad . \tag{2.6}$$

The event weight assigned to event i of multiplicity n in the intermittency analysis, is calculated as:

$$W_i^n = C_n W_{T,i}^n \quad . \tag{2.7}$$

2.3.5 Variables

To conclude this chapter, the variables used for the analysis are introduced.

- **Rapidity:**

$$y = \frac{1}{2} \ln(\frac{E + p_x}{E - p_x}) \quad , \tag{2.8}$$

  with E being the energy of the particle and p_x the momentum component in the beam direction. Formula (2.8) determines the cms rapidity if E and p_x are given in the center of mass system.

- **Azimuthal Angle:**

$$\varphi = \arctan(\frac{p_z}{p_y}) \quad . \tag{2.9}$$

  Since there is no preferred transverse direction for unpolarized incoming particles, the distribution in φ is uniform.

- **Transverse Momentum:**

$$p_T = \sqrt{p_y^2 + p_z^2} \quad . \tag{2.10}$$

- **The Squared Invariant Mass:**

$$M_{inv}^2 = (p_1 + p_2)^2 \quad , \tag{2.11}$$

where p_i denotes the four-momentum vector of particle i.

- **The Squared Four-Momentum Difference:**

$$Q^2 = -(p_1 - p_2)^2 \quad , \tag{2.12}$$

related to the invariant mass by

$$Q^2 = M_{inv}^2 - 2m_1^2 - 2m_2^2 \quad . \tag{2.13}$$

Bibliography

[ADAM86] M. Adamus et al., Z. Phys. **C32** (1986) 475.

[AGBE80] M. Aguilar-Benitez et al., "Addendum to the Proposal for the European Hybrid Spectrometer, Part D, The Hadron Calorimeters", CERN/SPS 80/50.

[AGBE83] M. Aguilar-Benitez et al., Nucl. Instr. Meth. **205** (1983) 79.

[ALBE84] J. Alberdi et al.,"The Forward Čerenkov Calibration for the Different Experiments in EHS", CERN/EP/LEDA 84-6.

[ALLI84] W.W.M. Allison et al., Nucl. Instr. Meth. **224** (1984) 396.

[ANDE84] B.H. Anders et al., Nucl. Instr. Meth. **219** (1984) 66.

[ATYR80] H.W. Atherton et al., Yellow Report CERN 80-79.

[BERG81] A. Bergier et al., "Triggering for experiments at EHS", CERN/EP/EHS/PH 81-14.

[COMM80] V. Commichau et al., Nucl. Instr. Meth. **176** (1980) 325.

[CRIJ84] F. Crijns, "The NA22 GEOHYB output structure", Nijmegen Note HEN240 (1984).

[DRLV82] A. De Roeck, Licentiaatsverhandeling, UIA (1982).

[DRFV83] A. De Roeck and F. Verbeure, "Acceptance Calculations of K^+p Events at 250 GeV/c in EHS with RCBC", CERN/EP/EHS/PH83-6 (1983).

[DRTH88] A. De Roeck, Ph.D. Thesis, UIA (1988).

[FBTH92] F. Botterweck, Ph.D. Thesis, Univ. of Nijmegen (1992).

[FCWF85] F. Crijns and W. Friebel, "Reconstruction of V^0's decaying in the spectrometer", Nijmegen Note HEN255 (1984).

[FERN84] C. Fernandez et al., Nucl. Instr. Meth. **225** (1984) 313.

[FMTH87] F. Meijers, Ph.D. Thesis, Univ. of Nijmegen (1987).

[HGFC84] H. Grässler and F. Crijns, NA22 measuring instructions, Nijmegen note (1984).

[HMSN84] P. Van Hal, F. Meijers, L. Scholten, "Note on the fixup/quality program", Nijmegen Note (1984).

[LSTH88] L. Scholten, Ph.D. Thesis, Univ. of Nijmegen (1988).

[NA2283] NA22 Scanning Instructions, Nijmegen Note (1983).

[NA2284] Y. Belokopytov, Scanload General Rules, Update, Serpukhov Note (1984).

[NA2289] Minutes of the 15th NA22 Collaboration Meeting, Serpukhov, May 1989, addendum 15.

[POWE82] B. Powell et al., Nucl. Instr. Meth. **198** (1982) 217.

[PROPOS] CERN/SPSC/75-15, EHS Proposal. CERN/SPSC/76-43, Addendum Part A. CERN/SPSC/79-117, Addendum Part B. CERN/SPSC/78-91, Addendum Part C. CERN/SPSC/80-43, Addendum Part D.

[SEVE86] D. Severeijns, "EHSML, An EHS Simulation Program User's Guide", Nijmegen Note HEN272 (1986).

[VHNN84] P. Van Hal, "Note on the ionization scan", Nijmegen Note (1984).

[VHTH87] P. Van Hal, Ph.D. Thesis, Univ. of Nijmegen (1987).

3

One-dimensional analysis

After the discovery of very large multiplicity events [JACE83, UA5P84], Białas and Peschanski proposed a method to investigate these fluctuations in the particular case of events with fixed multiplicity [BPNP86] . A generalization of the method to inclusive distributions followed two years later in [BPNP88]. By then the existence of events with a dense cluster in rapidity was established [JACE83, UA5C84, UA5P87, NA2287]. The proposition of the authors is based on the noise-suppressing feature of factorial moments, which makes them preferable to ordinary moments. The investigation of normalized factorial moments in decreasing rapidity domains is, therefore, believed to reveal interesting properties of the multiparticle production process. More precisely, if the dependence turns out to be a power law, it indicates the existence of self-similar fluctuations at all scales.

The derivation of these factorial moment properties is explained in sec. 3.1. The closely related factorial cumulant moments, very well suited for the investigation of genuine higher-order correlations and introduced into high-energy physics by Carruthers [PCPL91], are described in sec. 3.2. Besides the single variate factorial moments, Białas and Peschanski also proposed the bivariate factorial correlators [BPNP88]. They are introduced in sec. 3.3. Another tool to study the properties of the multiparticle production process came from Hwa [RHWA91]: the G-moments. A first definition of the G-moments is given in sec. 3.4 and an improvement in 3.5. Each section is accompanied by experimental results.

3.1 Factorial moments

3.1.1 Formalism

3.1.1.1 Normalized moments of a theoretical density distribution

In any one-dimensional phase-space variable y one can consider an initial interval Δ and divide that into M bins of size $\delta = \Delta/M$. If a single event has infinite particle multiplicity n, with n_m particles in bin m, the probability p_m to find a particle in bin m is given by

$$p_m = \lim_{n\to\infty} \frac{n_m}{n} = \lim_{n\to\infty} \frac{\rho_m \delta}{n} \ . \tag{3.1}$$

This also defines the particle density ρ_m in bin m for a single event.

The probability for an event to have a certain particle configuration, is given by the theoretical multivariate density probability distribution

$$P(\rho_1,\ldots,\rho_m,\ldots,\rho_M) \ . \tag{3.2}$$

This is the distribution one would find if gifted with an infinite number of events, all with infinite multiplicity.

The moment of order q is defined as

$$\langle\rho_m^q\rangle_P = \int_0^\infty \cdots \int_0^\infty P(\rho_1,\ldots,\rho_m,\ldots,\rho_M)\rho_m^q \mathrm{d}\rho_1 \ldots \mathrm{d}\rho_m \ldots \mathrm{d}\rho_M \tag{3.3}$$

and can be obtained from the moment generating function [KENSTU, VKSPPC, WMDICT]

$$\begin{aligned}
\mathcal{M}(s_1,\ldots,s_M) &= \left\langle \exp(\sum_{m=1}^{M} s_m\rho_m) \right\rangle & (3.4)\\
&= \int_0^\infty \cdots \int_0^\infty \prod_{m=1}^{M} e^{s_m\rho_m}\, P(\rho_1,\ldots,\rho_M) \prod_{m=1}^{M} \mathrm{d}\rho_m \\
&= \int_0^\infty \cdots \int_0^\infty \left(\prod_{m=1}^{M} \sum_{q_m=0}^{\infty} \frac{(s_m\rho_m)^{q_m}}{q_m!} \right) P(\rho_1,\ldots,\rho_M) \prod_{m=1}^{M} \mathrm{d}\rho_m \\
&= \sum_{q_1=0}^{\infty} \cdots \sum_{q_M=0}^{\infty} \left(\int_0^\infty \cdots \int_0^\infty \prod_{m=1}^{M} \rho_m^{q_m}\, P(\rho_1,\ldots,\rho_M) \prod_{m=1}^{M} \mathrm{d}\rho_m \right) \prod_{m=1}^{M} \frac{s_m^{q_m}}{q_m!} \\
&= \sum_{q_1=0}^{\infty} \cdots \sum_{q_M=0}^{\infty} \left\langle \prod_{m=1}^{M} \rho_m^{q_m} \right\rangle_P \prod_{m=1}^{M} \frac{s_m^{q_m}}{q_m!} \ . & (3.5)
\end{aligned}$$

Now, one can easily see that

$$\langle\rho_m^q\rangle_P = \left. \frac{\partial^q \mathcal{M}(s_1,\ldots,s_m,\ldots,s_M)}{\partial s_m^q} \right|_{all\ s_i=0} \ . \tag{3.6}$$

The normalized moment of order q in bin m is defined as

$$Z_q^{(m)} = \frac{\langle\rho_m^q\rangle_P}{\langle\rho_m\rangle_P^q} \tag{3.7}$$

and the bin-averaged form looks like

$$Z_q(\delta) = \frac{1}{M}\sum_{m=1}^{M} Z_q^{(m)} = \frac{1}{M}\sum_{m=1}^{M} \frac{\langle\rho_m^q\rangle_P}{\langle\rho_m\rangle_P^q} \ . \tag{3.8}$$

In their first paper [BPNP86], Białas and Peschanski proposed to study the moments

$$C_q(\delta) = \left\langle \frac{1}{M}\sum_{m=1}^{M} (Mp_m)^q \right\rangle \ . \tag{3.9}$$

They become equal to the moments $Z_q(\delta)$ in the limit (3.1) for a flat inclusive distribution in y.

3.1.1.2 Factorial moments of an experimental multiplicity distribution

Unfortunately, in experiments one never has an infinite number of events, nor do they have infinite multiplicity. The bias caused by the first experimental shortcoming will be dealt with in chapt. 5, but is neglected in all other chapters. How to handle statistical fluctuations introduced by the second deficiency is shown below.

Let n_m be the number of particles in bin m for a certain event. One can consider this number to be obtained by n_m independent realizations of the probability p_m to find a particle in bin m. The probability to find n_m particles in bin m then follows a Poisson distribution with average $\rho_m\delta$. Accepting this assumption, the multivariate particle number probability distribution is a convolution of the underlying dynamical density distribution and a multi-Poissonian noise [BPNP88, RPSF90]

$$Q(n_1,\dots,n_M) = \int P(\rho_1,\dots,\rho_M) \prod_{m=1}^{M} \frac{(\rho_m\delta)^{n_m}}{n_m!} e^{-\rho_m\delta} \mathrm{d}\rho_m \ . \tag{3.10}$$

The probability generating function of a discrete multivariate distribution like $Q(n_1,\dots,n_M)$ is defined as [KENSTU, VKSPPC, WMDICT]

$$\begin{aligned} \mathcal{F}(s_1,\dots,s_M) &= \left\langle \prod_{m=1}^{M} s_m^{n_m} \right\rangle_Q \\ &= \sum_{n_1=0}^{\infty} \cdots \sum_{n_M=0}^{\infty} \prod_{m=1}^{M} s_m^{n_m} \, Q(n_1,\dots,n_M) \ , \end{aligned} \tag{3.11}$$

so

$$n_1! \dots n_M! \, Q(n_1,\dots,n_M) = \left. \frac{\partial^{\sum_i n_i} \mathcal{F}(s_1,\dots,s_M)}{\prod_i \partial s_i^{n_i}} \right|_{all\ s_i=0} \tag{3.12}$$

This generating function can also be used to calculate the factorial moments

$$\left\langle n_m^{[q]} \right\rangle_Q = \langle n_m(n_m-1)\dots(n_m-q+1)\rangle_Q \ , \tag{3.13}$$

which will be shown in this particular case to be linked with the moments $\langle n_m^q \rangle_P$.

First one can rewrite (3.11) as

$$\begin{aligned} \mathcal{F}(s_1,\dots,s_M) &= \sum_{n_1=0}^{\infty} \cdots \sum_{n_M=0}^{\infty} \prod_{m=1}^{M} (s_m-1+1)^{n_m} \, Q(n_1,\dots,n_M) \\ &= \sum_{n_1=0}^{\infty} \cdots \sum_{n_M=0}^{\infty} \left(\prod_{m=1}^{M} \sum_{q_m=0}^{n_m} (s_m-1)^{q_m} \frac{n_m^{[q_m]}}{q_m!} \right) Q(n_1,\dots,n_M) \\ &= \sum_{q_1=0}^{\infty} \cdots \sum_{q_M=0}^{\infty} \left(\sum_{n_1=q_1}^{\infty} \cdots \sum_{n_M=q_M}^{\infty} \prod_{m=1}^{M} n_m^{[q_m]} Q(n_1,\dots,n_M) \right) \prod_{m=1}^{M} \frac{(s_m-1)^{q_m}}{q_m!} \\ &= \sum_{q_1=0}^{\infty} \cdots \sum_{q_M=0}^{\infty} \left\langle \prod_{m=1}^{M} n_m^{[q_m]} \right\rangle_Q \prod_{m=1}^{M} \frac{(s_m-1)^{q_m}}{q_m!} \ , \end{aligned} \tag{3.14}$$

implying that

$$\left\langle n_m^{[q]} \right\rangle_Q = \left. \frac{\partial^q \mathcal{F}(s_1,\dots,s_m,\dots,s_M)}{\partial s_m^q} \right|_{all\ s_i=1} \ . \tag{3.15}$$

Applying this formalism to the particular case (3.10), which is in fact a Poisson transform, one finds for the generating function

$$\begin{aligned}
\mathcal{F}(s_1,\ldots,s_M) &= \sum_{n_1=0}^{\infty}\cdots\sum_{n_M=0}^{\infty}\int P(\rho_1,\ldots,\rho_M)\prod_{m=1}^{M}\left(\frac{(\rho_m\delta s_m)^{n_m}}{n_m!}e^{-\rho_m\delta}\mathrm{d}\rho_m\right)\\
&= \int P(\rho_1,\ldots,\rho_M)\prod_{m=1}^{M}\left(\sum_{n_m=0}^{\infty}\frac{(\rho_m\delta s_m)^{n_m}}{n_m!}e^{-\rho_m\delta}\mathrm{d}\rho_m\right)\\
&= \int P(\rho_1,\ldots,\rho_M)\exp\left(\sum_{m=1}^{M}\rho_m\delta(s_m-1)\right)\prod_{m=1}^{M}\mathrm{d}\rho_m\\
&= \sum_{q_1=0}^{\infty}\cdots\sum_{q_M=0}^{\infty}\left(\int P(\rho_1,\ldots,\rho_M)\prod_{m=1}^{M}(\rho_m^{q_m}\mathrm{d}\rho_m)\right)\prod_{m=1}^{M}\left(\frac{\delta^{q_m}(s_m-1)^{q_m}}{q_m!}\right)\\
&= \sum_{q_1=0}^{\infty}\cdots\sum_{q_M=0}^{\infty}\left\langle\prod_{m=1}^{M}\rho_m^{q_m}\delta^{q_m}\right\rangle_P\prod_{m=1}^{M}\frac{\delta^{q_m}(s_m-1)^{q_m}}{q_m!}\quad . \qquad (3.16)
\end{aligned}$$

Comparing this result with (3.14), one can conclude

$$\left\langle n_m^{[q]}\right\rangle_Q = \langle\rho_m^q\rangle_P\,\delta^q\quad . \qquad (3.17)$$

After normalizing and bin averaging, this leads to

$$F_q(\delta) = \frac{1}{M}\sum_{m=1}^{M}\frac{\left\langle n_m^{[q]}\right\rangle_Q}{\langle n_m\rangle_Q^q} = \left[\frac{\langle\rho_m^q\rangle_P}{\langle\rho_m\rangle_P^q}\right] = Z_q(\delta)\quad . \qquad (3.18)$$

Where [ ] stands for the bin averaging.

If one neglects the influence of the finiteness of the number of events in an experiment, the average over the distribution Q can be replaced by an ordinary event average, denoted by $\langle\ \rangle$.

For a flat inclusive distribution

$$\langle n_m\rangle = \frac{1}{M}\left\langle\sum_{m=1}^{M}n_m\right\rangle = \frac{\langle n\rangle}{M} \qquad (3.19)$$

and (3.18) can be rewritten as

$$F_q(\delta) = M^{q-1}\frac{\left\langle\sum_{m=1}^{M}n_m^{[q]}\right\rangle}{\langle n\rangle^q}\quad . \qquad (3.20)$$

Since (3.20) demands less computer memory, it is also used for distributions that are approximately flat. Moments (3.20) are called horizontally normalized moments, moments (3.18) vertically normalized moments. The influence of a non-flat inclusive rapidity distribution on (3.20) is studied on NA22 data in [FBTH92]. Definition (3.18) is used throughout this whole thesis, unless explicitly mentioned.

3.1.1.3 Intermittency and fractality

Originally, intermittency in particle physics was defined as the power-law behavior of the normalized factorial moments

$$F_q(\delta) \propto \delta^{-\phi_q} \ , \ \phi_q > 0 \ , \tag{3.21}$$

with ϕ_q called intermittency strength or intermittency index. Nowadays, this is the strictest definition of intermittency. In a broader sense, intermittency refers to the rise of the normalized factorial moments with decreasing bin size δ.

A power-law dependence like (3.21) is typical for fractals [MAND82]. Fractals are self-similar objects of a non-integer dimension. Well known examples are the Cantor set and the Koch curve. The first steps of their self-similar construction procedure are shown in Fig. 3.1. At each step, the new figure consists of copies of the previous one, but at a smaller scale. After an infinite number of steps, one ends up with something between a point and a line in case of the Cantor set. For the Koch curve, one is left with something between a line and a plane. The resulting objects have a fractal dimension.

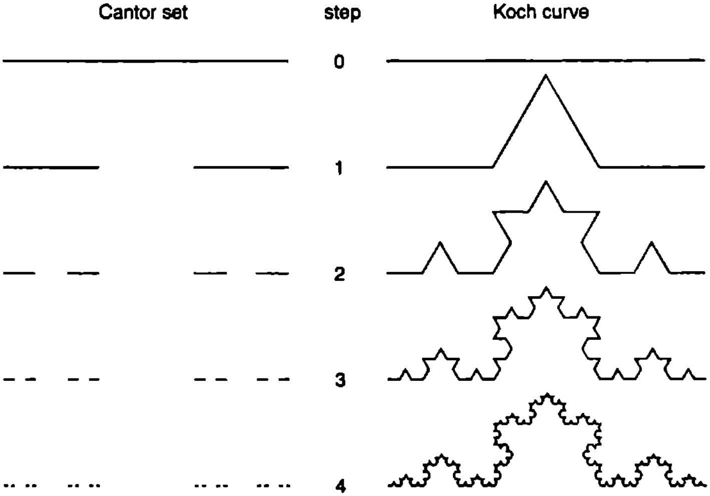

Figure 3.1: *The Cantor set and the Koch curve.*

In the following, these two fractals with topological dimension equal to one, are used to illustrate the link between the intermittency index ϕ_q and the fractal dimension D_F. An extension to higher dimensions is given in Sect. 4.

Call $N(\delta)$ the number of line pieces of size δ needed to cover the object. For the probability $p_m(\delta)$ of a point of the object to be in a line piece $N_m(\delta)$ holds

$$[p_m(\delta)] = \delta^{D_F} \ , \tag{3.22}$$

where the brackets denote the averaging over the $N(\delta)$ line pieces. One can see that

$$D_F = \lim_{\delta \to 0} \frac{\ln \sum_{m=1}^{N(\delta)} N^{-1}(\delta) p_m(\delta)}{\ln \delta} = - \lim_{\delta \to 0} \frac{\ln N(\delta)}{\ln \delta} \ , \tag{3.23}$$

where the second equality holds since $p_m(\delta) = N^{-1}(\delta)$. Form. (3.23) leads to $D_F = \ln 2/\ln 3$ for the Cantor set and $D_F = \ln 4/\ln 3$ for the Koch curve.

For monofractals (as Cantor set and Koch curve), by definition

$$[p_m^q(\delta)] = \delta^{qD_F} \quad , \tag{3.24}$$

with D_F independent of q.

The generalization to multifractals proceeds as follow [RENY70, JFED88]

$$\sum_{m=1}^{N(\delta)} p_m^q(\delta) = \left[p_m^{q-1}(\delta)\right] \propto \delta^{(q-1)D_q} \quad , \tag{3.25}$$

where the D_q are called the Rényi dimensions. They can be obtained from

$$D_q = \frac{1}{q-1} \lim_{\delta \to 0} \frac{\ln \sum_{m=1}^{N(\delta)} p_m^q(\delta)}{\ln \delta} \quad . \tag{3.26}$$

For some values of q the Rényi dimension has been given a special name: $D_0 = D_F$ is called the fractal dimension, D_1 the information dimension and D_2 the correlation dimension. Generally, for multifractals D_q decreases with increasing q.

In the intermittency analysis $N(\delta)$ corresponds to the number of bins M and $\delta = 1/M$ to the bin size; $p_m(\delta)$ is the probability to find a particle in bin m. The brackets [ ] in (3.25) then stand for the bin averaging. Suppose now the proportionality (3.25) still holds after event averaging. If, furthermore, one is dealing with a flat inclusive distribution, $Z_q(\delta) = C_q(\delta)$ and the power-law behavior (3.21) of $F_q(\delta)$ is connected with the same behavior of $C_q(\delta)$. One then can write [LBPL89, PLTH90]

$$\begin{aligned} C_q(\delta) &= \left\langle \frac{1}{M} \sum_{m=1}^{M} (M p_m(\delta))^q \right\rangle \\ &= M^{(q-1)} \left\langle \sum_{m=1}^{M} (p_m(\delta))^q \right\rangle \\ &\propto M^{\phi_q} \\ &\propto M^{q-1} M^{(1-q)D_q} \quad , \end{aligned} \tag{3.27}$$

which means that

$$D_q = 1 - \frac{\phi_q}{q-1} = 1 - d_q \quad . \tag{3.28}$$

The anomalous dimension d_q measures the deviation from the support (i.e. topological) dimension, equal to one in this case.

Even in the case of non-flat inclusive distributions, (3.28) is used for the connection between the anomalous dimension and the intermittency index.

3.1.1.4 The random-cascade model: a toy model

The first model used in High Energy Physics to demonstrate a power-law behavior of the normalized moments, is the random-cascade model [BPNP86, BPNP88].

Assume an initial density $\rho(\Delta)$ in an initial one-dimensional interval Δ. In the first step of the cascade, Δ is divided into λ bins and each part receives a weight W according to a random distribution with ensemble average $\{W\}$ equal to unity. At each step, all bins are split into λ new bins, again each assigned a weight W. After ν steps, one is left with $M = \lambda^\nu$ intervals of size $\delta = \Delta/M$. Each bin can be represented by a set of numbers $\{\alpha_1, \dots, \alpha_\nu\}$, with $\alpha_i = 1, \dots, \lambda$.

In Fig. 3.2 the Random-Cascade Model is shown for the special case $\lambda = 2$, called the α-model. The random variable W is now only allowed to take two values $\beta_- < 1$ and $\beta_+ > 1$ with probabilities a and b, respectively. These four parameters are constrained by

$$a\beta_- + b\beta_+ = 1 \qquad \text{and} \qquad a + b = 1 \quad . \tag{3.29}$$

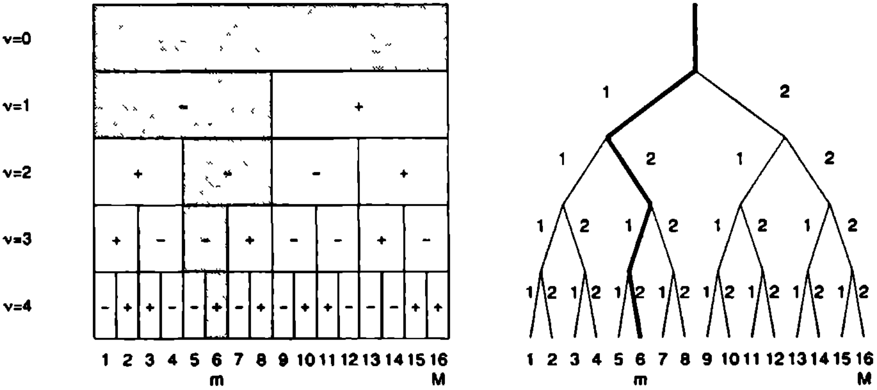

Figure 3.2: *The α-model of intermittency. At each step of the cascade, the interval is divided into two pieces. The density in each part is increased or decreased by a factor β_- or β_+ (with probabilities a and b, respectively), indicated by a "$-$" or a "$+$" sign. A typical path is marked in grey. It corresponds to the dark path in the so-called Cayley tree. The bin $m = 6$ is represented by the sequence $\{\alpha_1, \alpha_2, \alpha_3, \alpha_4\} = \{1, 2, 1, 2\}$.*

Since the cascade is a random process, it is sufficient to follow a path to one particular bin and then bin indices are superfluous. Call W_i the weight given in step i, then, after ν steps, the density in the bin of size δ is

$$\rho(\delta) = W_\nu W_{\nu-1} \dots W_1 \rho(\Delta) \quad . \tag{3.30}$$

Because of the independent weight assignment in the different steps of the cascade, the event average can be replaced by the product of ν ensemble averages. The moments of $\rho(\delta)$ are then given by

$$\langle \rho^q(\delta) \rangle = \{W^q\}^\nu \langle \rho^q(\Delta) \rangle \tag{3.31}$$

and the normalized ones by

$$Z_q(\delta) = \frac{\langle \rho^q(\delta) \rangle}{\langle \rho(\delta) \rangle^q} = \{W^q\}^\nu \frac{\langle \rho^q(\Delta) \rangle}{\langle \rho(\Delta) \rangle^q} \quad . \tag{3.32}$$

This yields the power-law behavior

$$Z_q(\delta) \propto M^{\frac{\ln\{W^q\}}{\ln\lambda}} \propto \delta^{-\frac{\ln\{W^q\}}{\ln\lambda}} \quad , \tag{3.33}$$

whence the intermittency index in case of the random-cascade model is given by

$$\phi_q = \frac{\ln\{W^q\}}{\ln\lambda} \quad . \tag{3.34}$$

Define now the quantity ξ as

$$\xi = \ln\left(\frac{\rho(\delta)}{\rho(\Delta)}\right) = \sum_{i=1}^{\nu} \ln W_i \quad , \tag{3.35}$$

where the second equality follows from (3.30). Since ξ is a sum of ν independent random variables, in the limit of large ν its distribution will be a normal distribution (central limit theorem)

$$P(\xi)\mathrm{d}\xi = \left(2\pi\nu\sigma^2\right)^{-\frac{1}{2}} \exp\left(-\frac{(\xi-\nu\mu)^2}{2\nu\sigma^2}\right)\mathrm{d}\xi \quad , \tag{3.36}$$

$$\text{with} \qquad \mu = \{\ln W\} \qquad \text{and} \qquad \sigma^2 = \left\{(\ln W)^2\right\} - \mu^2 \quad . \tag{3.37}$$

The corresponding distribution for $\rho(\delta)/\rho(\Delta)$ is called the log-normal distribution [BPNP88, PVPR87, ABZP91]. Performing a straightforward integration yields

$$Z_q(\delta) = \exp\left(\frac{1}{2}q(q-1)\nu\sigma^2\right) \quad , \tag{3.38}$$

i.e.

$$\phi_q = \left(\frac{1}{2}q(q-1)\sigma^2\right)\Big/\ln\lambda \tag{3.39}$$

$$= \frac{1}{2}q(q-1)\phi_2 \quad . \tag{3.40}$$

One should remark that the initial density $\rho(\Delta)$ is not conserved in the random-cascade model, this results into a total density fluctuating from event to event.

3.1.1.5 Link with the experimental q-particle densities

The inclusive density distribution for q particles in a variable y is defined as

$$\rho_q(y_1, y_2, \ldots, y_q) = \frac{1}{\sigma_{inel}} \frac{\mathrm{d}^q\sigma_{incl}}{\mathrm{d}y_1\mathrm{d}y_2\ldots\mathrm{d}y_q} \quad , \tag{3.41}$$

with σ_{inel} and σ_{incl} the total inelastic and inclusive cross sections. This can also be written as

$$\rho_q(y_1, y_2, \ldots, y_q) = \left\langle \sum_{n_1\neq n_2\neq\cdots\neq n_q}^{n} \delta(y_1 - y_{n_1})\delta(y_2 - y_{n_2})\ldots\delta(y_q - y_{n_q}) \right\rangle \quad , \tag{3.42}$$

where the sum runs over all q-tuples in an event of multiplicity n, the event average is denoted by $\langle\ \rangle$.

For identical particles, the q-particle density distribution is linked with the unnormalized factorial moment of order q by means of the following integration

$$\begin{aligned}\left\langle n_m^{[q]}\right\rangle &= \int_{y_{m-1}}^{y_m}\int_{y_{m-1}}^{y_m}\cdots\int_{y_{m-1}}^{y_m}\rho_q(y_1,y_2,\ldots,y_q)\mathrm{d}y_1\mathrm{d}y_2\ldots\mathrm{d}y_q \\ &= \int_{\Omega_m^q}\rho_q(y_1,y_2,\ldots,y_q)\mathrm{d}y_1\mathrm{d}y_2\ldots\mathrm{d}y_q\quad, \qquad (3.43)\end{aligned}$$

where y_{m-1} and y_m are the borders of bin m (y_0 and y_M define the initial interval Δ). The normalized factorial moments can then be written as

$$\begin{aligned}F_q(\delta) &= \frac{1}{M}\sum_{m=1}^{M}\frac{\int_{\Omega_m^q}\rho_q(y_1,y_2,\ldots,y_q)\mathrm{d}y_1\mathrm{d}y_2\ldots\mathrm{d}y_q}{\left(\int_{\Omega_m}\rho_1(y)\mathrm{d}y\right)^q} \\ &= \frac{1}{M\delta^q}\sum_{m=1}^{M}\int_{\Omega_m^q}\frac{\rho_q(y_1,y_2,\ldots,y_q)\mathrm{d}y_1\mathrm{d}y_2\ldots\mathrm{d}y_q}{\bar{\rho}_m^q}\quad. \qquad (3.44)\end{aligned}$$

If all particles are uncorrelated, the q-particle density distribution factorizes

$$\rho_q(y_1,\ldots,y_q)=\prod_{j=1}^{q}\rho_1(y_j)\quad. \qquad (3.45)$$

One can, therefore, consider the normalization in (3.44) to be a normalization to the uncorrelated background.

3.1.2 Experimental results

A detailed analysis of the one-dimensional factorial moments in rapidity, including the study of the experimental resolution, can be found in [FBTH92]. In this section, the main results are summarized and some new predictions of the FRITIOF Monte Carlo model [FRIT87] are included.

3.1.2.1 Factorial moments for all charged particles

If the factorial moments $F_q(\delta y)$ exhibit a power-law behavior (3.21), this would show up as a linear behavior on a double logarithmic plot.

In Fig. 3.3 $\ln F_q(\delta y)$ is shown versus $-\ln\delta y$, i.e. versus decreasing bin size. The data are represented by the black dots and contain all charged particles in the initial rapidity interval $\Delta y=[-2,2]$. This region is the "plateau" of the rapidity distribution and within this region almost all particles are pions.

It is clear that the power law only holds approximately: after an initial sharp increase, $\ln F_q(\delta y)$ flattens at smaller bin sizes. Therefore, the intermittency indices are only determined in a restricted δy-region. To do so, a linear fit

$$\ln F_q(\delta y)=a_q-\phi_q\ln\delta y \qquad (3.46)$$

is applied to the data in the region $0.1\le\delta y\le 1$, the lower limit being a restriction of statistics, the upper one is set to avoid possible trivial effects e.g. from resonance decays.

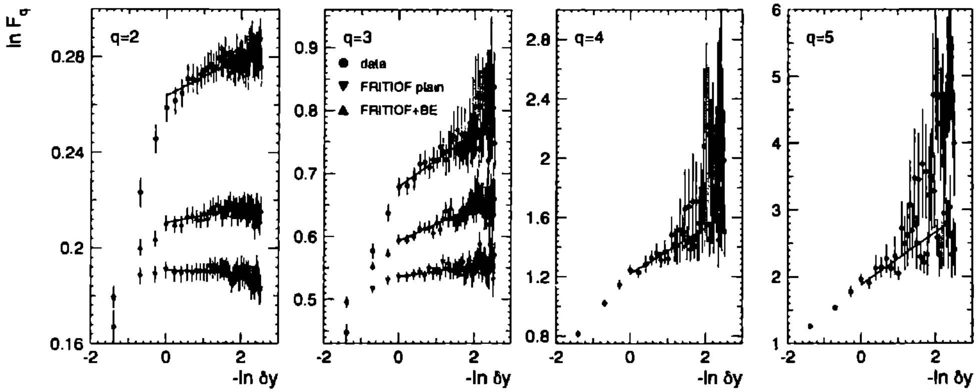

Figure 3.3: *Factorial moments of order $q = 2, \ldots, 5$ for the all-charged-particle sample, compared with predictions from FRITIOF2.0 with and without BE-interference.*

Correlations between the data points at different bin sizes (bin-size correlations) are not taken into account here[1].

The factorial moments of fourth and fifth order show large fluctuations at small bin sizes. This is due to bin splitting, i.e. particles of a spike all contained in one bin for a certain value of M may be divided over two bins for $M+1$, since the position of the bin borders depends on the number of divisions M.

The intermittency strength increases with increasing order (see Tab. 3.1), indicating a multifractal structure in the multiparticle production process.

	ϕ_2	ϕ_3	ϕ_4	ϕ_5
data	0.008 ± 0.002	0.043 ± 0.006	0.16 ± 0.02	0.39 ± 0.06
FRITIOF plain	-0.001 ± 0.001	0.009 ± 0.003	0.068 ± 0.009	0.17 ± 0.02
FRITIOF + BE	0.003 ± 0.001	0.027 ± 0.003	0.12 ± 0.01	0.33 ± 0.03

Table 3.1: *Intermittency indices for all charged particles compared to predictions from FRITIOF2.0 with and without BE-interference.*

In Fig. 3.3 the $q = 2, 3$ data (black dots) are compared to predictions obtained from FRITIOF2.0 with (black triangles up) and without (black triangles down) Bose-Einstein correlations (see Sect. 3.1.2.2). For higher orders the pictures become unclear due to large

---

[1] Different fit procedures, including those taking into account bin-size correlations, are extensively discussed in [FBTH92], but it turned out that this linear fit gives visually the best result and should be used as indication of the rise of the moments.

errors and fluctuations. Nevertheless, the intermittency indices are collected for all orders in Tab. 3.1.

Here, FRITIOF version 2.0 is used, although more recent versions are now available. The reason is that this version has been tuned to the NA22 data in terms of single particle inclusive distributions. A description of the parameter settings can be found in [NA2292]. In addition, the ρ, η and η' production rates are reduced, since they have been found to be overestimated in the default version [NA2292, WWPL92, ALEP92]. The influence of this overproduction on factorial moments is treated in [EDWP92]. The model used with these parameter values will be referred to as FRITIOF plain. It is clear from Fig. 3.3 that, except for full phase space, the predictions for the F_q values are too low. This results in an underestimation of the intermittency index. The situation improves when introducing BE correlations (see Sect. 3.1.2.2) in FRITIOF, though the experimental values are not reached. At higher order, the difference between experimental and predicted values decreases.

3.1.2.2 The influence of Bose-Einstein correlations

Bose-Einstein (BE) correlations are a quantum-mechanical effect. The symmetrization of the wave function of identical bosons leads to an enhanced probability to find two identical bosons close in phase space. Since most of the analyzed particles are pions, the BE-correlations are expected to play an important role in the rise of the factorial moments. In fact, if intermittency would be purely due to BE-interference, the intermittency index has been predicted [MGYU92] to increase by a factor two when instead of the all-charged sample a like-charged sample is used.

In FRITIOF2.0, the BE correlations are incorporated according to the algorithm developed by Sjöstrand for JETSET7.3 [TSJO82, TSMB87]. In case presented, an exponentional parametrization $(1+\lambda\exp(-rQ))$ is used, with $\lambda = 0.72$ and $r = 4.0\ \mathrm{GeV}^{-1}$. These parameters are obtained from a fit to the NA22 data.

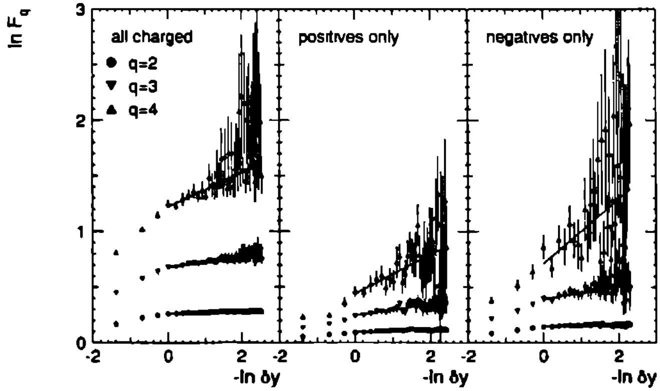

Figure 3.4: *Factorial moments of order* $q = 2,\ldots,4$ *for the all-charged sample, and the restriction to the positives-only and negatives-only samples.*

		ϕ_2	ϕ_3	ϕ_4
positives only	data	0.010 ± 0.002	0.050 ± 0.009	0.18 ± 0.03
	FRITIOF plain	-0.003 ± 0.002	-0.020 ± 0.006	-0.12 ± 0.03
	FRITIOF + BE	0.003 ± 0.002	0.028 ± 0.006	0.10 ± 0.03
negatives only	data	0.007 ± 0.003	0.06 ± 0.02	0.29 ± 0.06
	FRITIOF plain	0.001 ± 0.002	-0.031 ± 0.008	-0.18 ± 0.03
	FRITIOF + BE	0.010 ± 0.002	0.08 ± 0.01	0.73 ± 0.07

Table 3.2: *Intermittency indices for positives and negatives only, compared with predictions of FRITIOF2.0 with and without BE-interference.*

Fig. 3.4 and Tab. 3.2 demonstrate what happens when instead of the all-charged sample a like-charged sample is used. The values of the moments are smaller, but the increase with decreasing bin sizes is stronger. However, the predicted factor two is not reached. The difference between the positives-only and the negatives-only samples is due to the influence of the positive beam particle.

For the like-charged sample FRITIOF plain predicts negative intermittency strengths. The intermittency indices predicted by FRITIOF+BE stay the same when restricting to positives, but increase by *more* than a factor two when restricting to negatives. In the latter case the model even overestimates the strength for $q = 4$.

3.1.2.3 Transverse momentum dependence

In search for an understanding of the origin of intermittency, the sample has been divided into subsamples depending on the transverse momentum p_T of the particles. The strongest rise of the moments is observed for the low p_T-sample $p_T < 0.15$ GeV/c, the weakest rise for the high-p_T sample $p_T > 0.30$ GeV/c (Fig. 3.5 and Tab. 3.3). This low p_T-effect will be reconsidered in Sect. 5.2.2.2.

However, it should be noted that the most significant spike event, which has five of its ten spike tracks (see Fig. 1.1a) at $p_T < 0.15$ GeV/c, has a large influence in this analysis. One should, therefore, be cautious when drawing conclusions.

Neither the plain version of FRITIOF nor the version including BE-correlations does reproduce the p_T-dependence of the data (Tab. 3.3). For particles with $p_T < 0.15$ GeV/c the intermittency signal is even predicted to vanish.

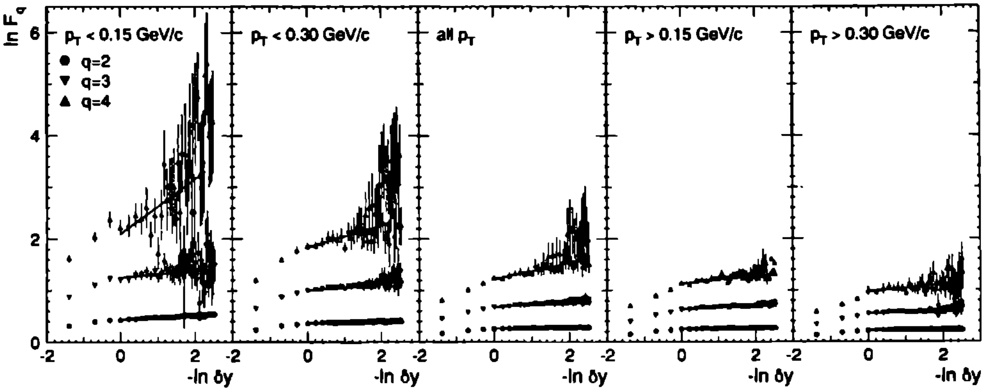

Figure 3.5: *Factorial moments of order $q = 2, \ldots, 4$ for different p_T regions.*

		ϕ_2	ϕ_3	ϕ_4
$p_T < 0.15$ GeV/c	data	0.039 ± 0.007	0.07 ± 0.04	0.5 ± 0.1
	FRITIOF plain	0.001 ± 0.005	0.05 ± 0.03	-0.1 ± 0.2
	FRITIOF + BE	0.014 ± 0.005	0.01 ± 0.02	-0.1 ± 0.1
$p_T < 0.30$ GeV/c	data	0.016 ± 0.003	0.07 ± 0.01	0.21 ± 0.05
	FRITIOF plain	0.006 ± 0.002	0.024 ± 0.008	0.00 ± 0.03
	FRITIOF + BE	0.018 ± 0.002	0.104 ± 0.009	0.35 ± 0.03
$p_T > 0.15$ GeV/c	data	0.010 ± 0.002	0.036 ± 0.006	0.10 ± 0.02
	FRITIOF plain	-0.001 ± 0.001	0.014 ± 0.004	0.08 ± 0.01
	FRITIOF + BE	0.003 ± 0.001	0.034 ± 0.004	0.16 ± 0.02
$p_T > 0.30$ GeV/c	data	0.007 ± 0.002	0.029 ± 0.009	0.07 ± 0.03
	FRITIOF plain	-0.003 ± 0.002	0.010 ± 0.005	0.04 ± 0.02
	FRITIOF + BE	0.001 ± 0.002	0.032 ± 0.006	0.19 ± 0.02

Table 3.3: *Intermittency indices for different p_T regions, compared with predictions of FRITIOF2.0 with and without BE-interference.*

3.2 Factorial cumulant moments

3.2.1 Formalism

3.2.1.1 Correlation functions and factorial cumulant moments

Although intermittency as originally considered by Białas and Peschanski was formulated in terms of particle densities, it is known from many branches of physics, that the inclusive density distributions $\rho_q(y_1,\ldots,y_q)$ are often ill-suited to reveal higher-order dynamical effects. Besides genuine q-particle correlations, the ρ_q contain contributions from random associations of lower-order correlated and uncorrelated q'-particle groups ($q' \leq q$). For most applications, it is more convenient to eliminate the latter and to concentrate the analysis on connected correlation functions.

This is easily accomplished via a cluster expansion familiar from statistical mechanics [KHSM63]. The correlation functions $C_q(y_1,\ldots,y_q)$ for $q = 1,\ldots,5$ are given by

$$\begin{aligned}
C_1(y_1) &= \rho_1(y_1)\\
C_2(y_1,y_2) &= \rho_2(y_1,y_2) - \rho_1(y_1)\rho_1(y_2)\\
C_3(y_1,y_2,y_3) &= \rho_3(y_1,y_2,y_3) - \rho_1(y_1)\rho_2(y_2,y_3) - \rho_1(y_2)\rho_2(y_3,y_1) - \rho_1(y_3)\rho_2(y_1,y_2)\\
&\quad +2\rho_1(y_1)\rho_1(y_2)\rho_1(y_3)\\
C_4(y_1,\ldots,y_4) &= \rho_4(y_1,\ldots,y_4) - \sum_{(4)}\rho_1(y_1)\rho_3(y_2,y_3,y_4) - \sum_{(3)}\rho_2(y_1,y_2)\rho_2(y_3,y_4)\\
&\quad +2\sum_{(6)}\rho_1(y_1)\rho_1(y_2)\rho_2(y_3,y_4) - 6\rho_1(y_1)\rho_1(y_2)\rho_1(y_3)\rho_1(y_4)\\
C_5(y_1,\ldots,y_5) &= \rho_5(y_1,\ldots,y_5) - \sum_{(5)}\rho_1(y_1)\rho_4(y_2,\ldots,y_5) - \sum_{(10)}\rho_2(y_1,y_2)\rho_3(y_3,y_4,y_5)\\
&\quad +2\sum_{(10)}\rho_1(y_1)\rho_1(y_2)\rho_3(y_3,y_4,y_5) + 2\sum_{(15)}\rho_1(y_1)\rho_2(y_2,y_3)\rho_2(y_4,y_5)\\
&\quad -15\sum_{(4)}\rho_1(y_1)\rho_1(y_2)\rho_1(y_3)\rho_2(y_4,y_5)\\
&\quad +24\rho_1(y_1)\rho_1(y_2)\rho_1(y_3)\rho_1(y_4)\rho_1(y_5)\ . \qquad (3.47)
\end{aligned}$$

These correlation functions exhibit the nice feature that they become zero whenever one of their arguments is independent of the other ones, i.e. when not all particles of the q-tuple are correlated.

After integration over a suitable q-dimensional phase-space region (see (3.42)), (3.47) leads to a set of equations relating the factorial moments to their connected counterparts, the factorial cumulant moments [KENSTU, MUEL71]. For orders $q = 1,\ldots,5$ one finds

$$\begin{aligned}
k_1^{(m)} &= \langle n_m\rangle\\
k_2^{(m)} &= \left\langle n_m^{[2]}\right\rangle - \langle n_m\rangle^2\\
k_3^{(m)} &= \left\langle n_m^{[3]}\right\rangle - 3\left\langle n_m^{[2]}\right\rangle\langle n_m\rangle + 2\langle n_m\rangle^3\\
k_4^{(m)} &= \left\langle n_m^{[4]}\right\rangle - 4\left\langle n_m^{[3]}\right\rangle\langle n_m\rangle - 3\left\langle n_m^{[2]}\right\rangle^2 + 12\left\langle n_m^{[2]}\right\rangle\langle n_m\rangle^2 - 6\langle n_m\rangle^4
\end{aligned}$$

$$\begin{aligned} k_5^{(m)} &= \left\langle n_m^{[5]} \right\rangle - 5 \left\langle n_m^{[4]} \right\rangle \langle n_m \rangle - 10 \left\langle n_m^{[3]} \right\rangle \left\langle n_m^{[2]} \right\rangle + 20 \left\langle n_m^{[3]} \right\rangle \langle n_m \rangle^2 \\ &\quad +30 \left\langle n_m^{[2]} \right\rangle^2 \langle n_m \rangle - 60 \left\langle n_m^{[2]} \right\rangle \langle n_m \rangle^3 + 24 \langle n_m \rangle^5 \quad . \end{aligned} \tag{3.48}$$

The relations between factorial cumulant moments and factorial moments can also be obtained from the link between their generating functions. If

$$k_q^{(m)} = \left. \frac{\partial^q \mathcal{H}(s_1, \ldots, s_m, \ldots, s_M)}{\partial s_m^q} \right|_{all\ s_i=1} \tag{3.49}$$

then

$$\mathcal{H}(s_1, \ldots, s_M) = \ln \mathcal{F}(s_1, \ldots, s_M) \tag{3.50}$$

with $\mathcal{F}(s_1, \ldots, s_M)$ the factorial moment generating function (3.14). After restriction to a particular bin m this leads to [MUEL71]

$$k_q^{(m)} = q! \sum_{i_p} \left\{ (-1)^{(i_1-1)} (i_1 - 1)!\, \delta(q - \sum_{p=1}^{q} i_p) \prod_{p=1}^{q} \frac{1}{(i_p - i_{p+1})!} \left(\frac{\left\langle n_m^{[p]} \right\rangle}{p!} \right)^{(i_p - i_{p+1})} \right\} \quad , \tag{3.51}$$

where the first sum runs over all $i_p \geq i_{p+1}$, $i_1 \geq 1$ and $p = 1, \ldots, q$ and $i_{q+1} = 0$.

Analogously to the normalized factorial moments (3.18) and (3.44), the normalized factorial cumulant moments are defined as

$$K_q(\delta) = \left[\frac{k_q^{(m)}}{\langle n_m \rangle^q} \right] \tag{3.52}$$

$$\begin{aligned} &= \frac{1}{M} \sum_{m=1}^{M} \frac{\int_{\Omega_m^q} C_q(y_1, y_2, \ldots, y_q) \mathrm{d}y_1 \mathrm{d}y_2 \ldots \mathrm{d}y_q}{\left(\int_{\Omega_m^q} \rho_1(y) \mathrm{d}y \right)^q} \\ &= \frac{1}{M\delta^q} \sum_{m=1}^{M} \int_{\Omega_m^q} \frac{C_q(y_1, y_2, \ldots, y_q) \mathrm{d}y_1 \mathrm{d}y_2 \ldots \mathrm{d}y_q}{\bar{\rho}_m^q} \quad , \end{aligned} \tag{3.53}$$

For the second and third order, the following relations hold between the normalized factorial cumulant moments and the normalized factorial moments

$$\begin{aligned} K_2(\delta) &= F_2(\delta) - 1 \\ K_3(\delta) &= F_3(\delta) - 3F_2(\delta) + 2 \quad , \end{aligned} \tag{3.54}$$

for higher orders no exact relations exist due to bin averaging.

Just as the factorial moments, the factorial cumulant moments remove the influence of multi-Poissonian noise. They are linked to the ordinary cumulant moments $\kappa_q^{(m)}$ of the theoretical density distribution P by

$$\left(k_q^{(m)} \right)_Q = \left(\kappa_q^{(m)} \right)_P \delta^q \quad , \tag{3.55}$$

where $(\ )_X$ denote the distribution over which the averages have been performed.

In analogy to the factorial quantities, the generating function of the cumulant moments is given by

$$\mathcal{K}(s_1, \ldots, s_M) = \ln \mathcal{M}(s_1, \ldots, s_M) \quad , \tag{3.56}$$

with $\mathcal{M}(s_1, \ldots, s_M)$ as defined in (3.4). It is clear that the relations between κ_q and $\langle \rho^q \rangle$ have exactly the same structure as (3.48) and (3.51).

3.2.1.2 Contributions from lower-order correlations

Inverting the set of equations (3.48) gives

$$\begin{aligned}
\left\langle n_m^{[2]} \right\rangle &= \left(k_1^{(m)}\right)^2 + k_2^{(m)} \\
\left\langle n_m^{[3]} \right\rangle &= \left(k_1^{(m)}\right)^3 + 3k_2^{(m)}k_1^{(m)} + k_3^{(m)} \\
\left\langle n_m^{[4]} \right\rangle &= \left(k_1^{(m)}\right)^4 + 6k_2^{(m)}\left(k_1^{(m)}\right)^2 + 3\left(k_2^{(m)}\right)^2 + 4k_3^{(m)}k_1^{(m)} + k_4^{(m)} \\
\left\langle n_m^{[5]} \right\rangle &= k_5^{(m)} + 5k_4^{(m)}k_1^{(m)} + 10k_3^{(m)}k_2^{(m)} + 10k_3^{(m)}(k_1^{(m)})^2 + 15(k_2^{(m)})^2k_1^{(m)} \\
&\quad +10k_2^{(m)}(k_1^{(m)})^3 + (k_1^{(m)})^5 \ .
\end{aligned} \tag{3.57}$$

The general formula can be obtained from

$$\mathcal{F}(s_1,\ldots,s_M) = \exp\mathcal{H}(s_1,\ldots,s_M) \ , \tag{3.58}$$

which leads to [MUEL71]

$$\left\langle n_m^{[q]} \right\rangle = q! \sum_{i_p}^{q} \left\{ \delta(q - \sum_{p=1}^{q} i_p) \prod_{p=1}^{q} \frac{1}{(i_p - i_{p+1})!} \left(\frac{k_p^{(m)}}{p!} \right)^{(i_p - i_{p+1})} \right\} \ , \tag{3.59}$$

where the first sum runs over all $i_p \geq i_{p+1}$ and $p = 1,\ldots,q$ and $i_{q+1} = 0$.

The substitution $k_q^{(m)} = 0$ for $q > 2$ in the above relations gives the contribution from two-particle correlations to the factorial moments. After normalization and bin averaging, one obtains

$$\begin{aligned}
F_3^{(2)}(\delta) &= 1 + 3K_2(\delta) \\
F_4^{(2)}(\delta) &= 1 + 6K_2(\delta) + 3\left[\left(K_2^{(m)}(\delta)\right)^2\right] \ .
\end{aligned} \tag{3.60}$$

The combination of two and three-particle contributions to F_4 is obtained by setting $k_q = 0$ for $q > 3$, which leads to

$$F_4^{(3)}(\delta) = 1 + 6K_2(\delta) + 3M\left[\left(K_2^{(m)}(\delta)\right)^2\right] + 4K_3(\delta) \ . \tag{3.61}$$

Contributions to higher-order moments can be obtained via analogous procedures.

3.2.1.3 Linked-pair approximation

In order to understand the nature of the higher-order multiparticle correlations, a number of attempts have been made to express the higher-order normalized correlation functions in terms of linked second-order normalized correlation functions [HETH91, PCPL91, PCPR89, DWAP90, ACWS90, PBPL91]. The normalized correlation functions are defined as

$$c_q(y_1,\ldots,y_q) = \frac{C_q(y_1,\ldots,y_q)}{\rho_1(y_1)\ldots\rho_1(y_q)} \ . \tag{3.62}$$

Here, the linking procedure proposed by Carruthers et al. [PCPR89, PCPL91], known as the linked-pair approximation (LPA), is discussed. The authors make the ansatz

$$c_q(y_1,\ldots,y_q) = \frac{A_q}{(q!/2)} \sum_{\text{perm.}} c_2(y_1,y_2)c_2(y_2,y_3)\ldots c_2(y_{q-1},y_q) \ , \tag{3.63}$$

where the parameters A_q are a set of constants.

After combining (3.53) and (3.62), the normalized factorial cumulant moment for a particular bin can be expressed as

$$\begin{aligned} K_q^{(m)}(\delta) &= \frac{1}{\delta^q \bar{\rho}_m^q} \int_{\Omega_m^q} c_q(y_1,\ldots,y_q)\rho_1(y_1)\ldots\rho_1(y_q)\mathrm{d}y_1\ldots\mathrm{d}y_q \\ &\approx \frac{1}{\delta^q} \int_{\Omega_m^q} c_q(y_1,\ldots,y_q)\mathrm{d}y_1\ldots\mathrm{d}y_q \ , \end{aligned} \tag{3.64}$$

where the approximation holds if one assumes that the single particle density distribution $\rho_1(y)$ changes slowly within each bin. Inserting the linking ansatz (3.63), this leads to

$$K_q^{(m)}(\delta) = \frac{A_q}{\delta^q} \int_{\Omega_m^q} c_2(y_1,y_2)c_2(y_2,y_3)\ldots c_2(y_{q-1},y_q)\mathrm{d}y_1\mathrm{d}y_2\ldots\mathrm{d}y_q \ . \tag{3.65}$$

Assuming that within each bin

$$c_2(y_1,y_2) \approx c_2(|y_1-y_2|) \tag{3.66}$$

and applying the transformation

$$\begin{aligned} \zeta_p &:= y_{p+1} - y_p \quad (p = 1,\ldots,(q-1)) \\ \Upsilon &:= \frac{1}{q}\sum_{p=1}^{q} y_p \ , \end{aligned} \tag{3.67}$$

the following expression appears after integration over the variable Υ

$$K_q^{(m)}(\delta) = \frac{A_q}{\delta^{(q-1)}} \int_{\Omega_m^q} c_2(\zeta_1)c_2(\zeta_2)\ldots c_2(\zeta_{q-1})\mathrm{d}\zeta_1\mathrm{d}\zeta_2\ldots\mathrm{d}\zeta_{q-1} \ . \tag{3.68}$$

Since the integration domain Ω_m^q is expressed as a function of the original variables y_p, the integral in (3.68) does not factorize. Therefore the so-called strip approximation is applied, consisting of a change in the integration domain. In Fig. 3.6 this approximation is demonstrated for $M = 6$ and $q = 2$. In this case, the full integration domain consists of six squares Ω_m, each square corresponding to one bin. Replacing the squares by the dotted rectangles, the area is kept constant and one can expect this new integration domain to give approximately the same result as the original one.

Generally, the strip approximation domain is defined by

$$\begin{aligned} -\delta/2 \le \ &\zeta_p \le \delta/2 \quad (p = 1,\ldots,(q-1)) \\ (m-1)\delta \le \ &\Upsilon \le m\delta \ . \end{aligned} \tag{3.69}$$

This allows to write

$$K_2^{(m)}(\delta) \approx \frac{1}{\delta}\int_{-\delta/2}^{\delta/2} c_2(\zeta)\mathrm{d}\zeta \tag{3.70}$$

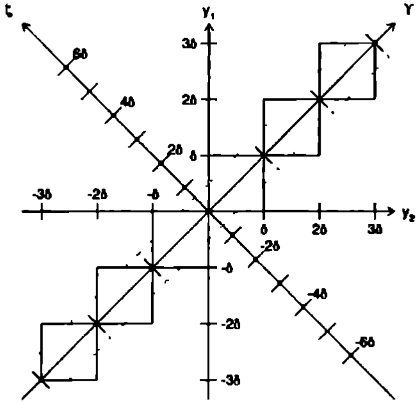

Figure 3.6: *Illustration of the strip approximation for second order.*

and (3.68) factorizes into

$$K_q^{(m)}(\delta) = A_q \left(K_2^{(m)}(\delta)\right)^{q-1} \tag{3.71}$$

After bin averaging, this becomes

$$K_q(\delta) = A_q \left[\left(K_2^{(m)}\right)^{q-1}\right] , \tag{3.72}$$

with [ ] standing for the bin averaging and A_q independent of δ.

3.2.1.4 Negative binomial distribution

During the last decade, the Negative Binomial Distribution (NBD) has proven its usefulness as a description of the multiplicity distribution in a variety of interactions [UA5P85, NBDR88], including the NA22 data [NA22PL, NA22ZP]. It is, therefore, worthwhile to look at some of its properties connected with the material presented here.

The NBD probability is given by

$$P_n(\bar{n}, k) = \frac{\Gamma(n+k)}{\Gamma(n+1)\Gamma(k)} \left(\frac{k}{k+\bar{n}}\right)^k \left(\frac{\bar{n}}{k+\bar{n}}\right)^n , \tag{3.73}$$

where $\bar{n}$ equals the average multiplicity and k is linked to the dispersion D of the distribution via

$$\frac{D^2}{\bar{n}} = 1 + \frac{\bar{n}}{k} . \tag{3.74}$$

Its factorial moment generating function is

$$\mathcal{F}(s) = \left(1 - (s-1)\frac{\bar{n}}{k}\right)^{-k} , \tag{3.75}$$

from which one finds (see (3.15)) the normalized factorial moments

$$F_q^{\mathrm{NBD}} = \frac{\left\langle n^{[q]} \right\rangle}{\bar{n}^q} = \frac{k^{[q]}}{k^q} \tag{3.76}$$

to be independent of the average multiplicity.

From the factorial cumulant moment generating function

$$\mathcal{H}(s) = \ln \mathcal{F}(s) \tag{3.77}$$

one obtains for the normalized factorial cumulant moments

$$K_q^{\mathrm{NBD}} = \frac{k_q}{\bar{n}} = \frac{(q-1)!}{k^{q-1}} \quad . \tag{3.78}$$

It is then clear that

$$K_q^{\mathrm{NBD}} = (q-1)! \left(K_2^{\mathrm{NBD}} \right)^{q-1} \tag{3.79}$$

and

$$A_q^{\mathrm{NBD}} = (q-1)! \quad . \tag{3.80}$$

This linking feature of the NBD was first noticed by De Wolf [DWAP90].

3.2.2 Experimental results

3.2.2.1 Factorial cumulant moments

Inspite of their theoretically interesting properties, an experimental analysis of the factorial cumulant moments suffers from serious drawbacks.

It is already clear from the relations (3.48) that the errors on $\left\langle n_m^{[q]} \right\rangle$ can accumulate to large errors on $k_q^{(m)}$.

Furthermore, genuine higher-order correlations can be generated artificially if the average number of particles is small compared to the number of correlated particles. This can be understood if one looks at formula (3.50) in more detail. Inverting this formula and restricting to a single bin gives

$$\mathcal{F}(s) = \exp\left(\mathcal{H}(s)\right) \quad . \tag{3.81}$$

If the multiplicity in the bin equals n, the factorial moment generating function $\mathcal{F}(s)$ is just a polynomial in s,

$$\sum_{q=0}^{n} n^{[q]} \frac{(s-1)^q}{q!} \quad , \tag{3.82}$$

and requires the exponent in (3.81) to be an infinite series in s. This means that higher-order factorial cumulants are needed to cancel lower-order ones in order to make $\left\langle n^{[q]} \right\rangle$ vanish for $q > n$.

These fake particle correlations are observed experimentally for small bin sizes as large fluctuations, involving sign flips of $K_q(\delta y)$. Empirically, it turns out that the $K_q(\delta y)$ are trustable for bin sizes for which $F_q(\delta y)$ has a relative error less than 50% and for which $F_{q+1}(\delta y) \neq 0$ holds.

As can be seen in Fig. 3.7, the errors on the $K_q(\delta y)$ are very large, especially for higher orders at small bin sizes. However, these errors are overestimated: The $\left\langle n_m^{[q]} \right\rangle$ for different q-values are correlated, these correlations have not been taken into account in the error calculation. Although it would be straightforward to do so, it is a tremendous job involving matrices exceeding the available memory space on the computer used. Neglecting these order-order correlations is clearly the worse the higher the order. From Fig. 3.7 it is clear that genuine two- and three-particle correlations indeed exist and that they increase with decreasing bin sizes. For strong conclusions on the higher orders more precise measurements and/or higher statistics are needed, though also they tend to increase with decreasing bin sizes.

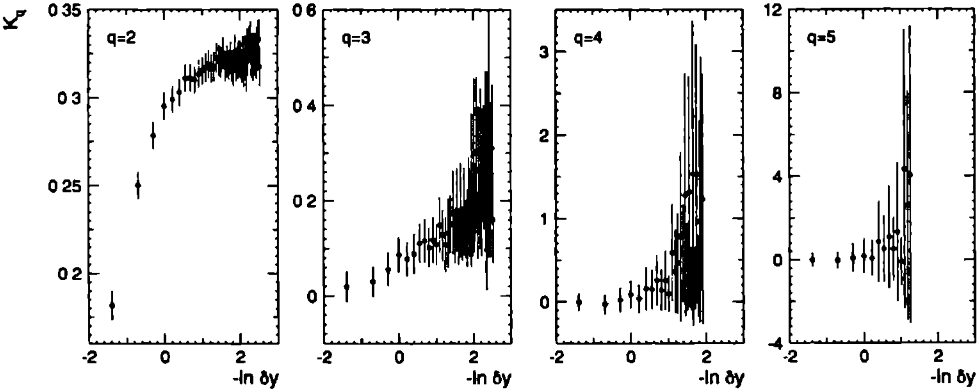

Figure 3.7: *The normalized factorial cumulant moments for orders $q = 2, \ldots, 5$.*

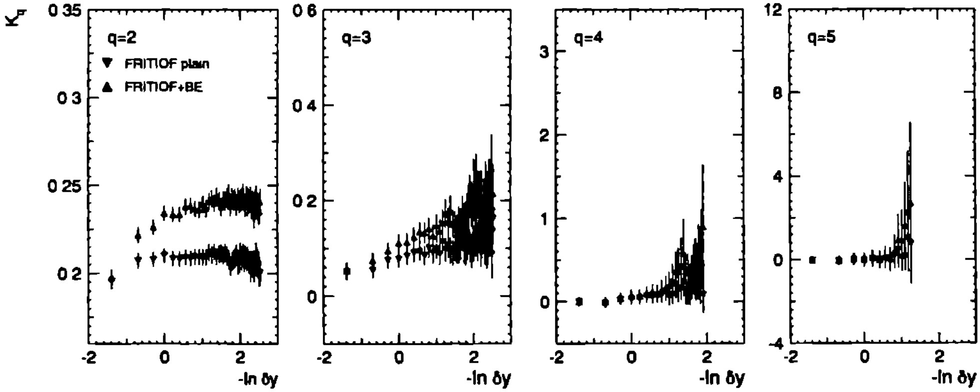

Figure 3.8: *The normalized factorial cumulant moments predicted by FRITIOF plain (triangles down) and FRITIOF with BE-correlations (triangles up).*

The FRITIOF predictions for the normalized factorial cumulant moments are shown in Fig. 3.8. The genuine q-particle correlations are underestimated, both by the plain version and the version including Bose-Einstein correlations (see Sect. 3.1.2).

In [HETH91, PCPL91] it has been pointed out that it may be the normalized factorial cumulant moments that have the feature of scaling, rather than the normalized factorial moments. In order to test this hypothesis, $\ln K_q(\delta y)$ is plotted as a function of $-\ln \delta y$ for $q = 2, 3, 4$ (Fig. 3.9) and a linear fit according to

$$\ln K_q(\delta y) = a_q - \psi_q \delta y \tag{3.83}$$

is applied to the data (solid lines in Fig. 3.9). The fit parameters ψ_q obtained are collected in Tab. 3.4, together with those for FRITIOF. As in the case of the normalized factorial moments, the fit region is restricted to $0.1 \leq \delta y \leq 1$, except for $q = 4$ where fake correlations (see above) limit the smallest δy-value to 0.148. In Tab. 3.4 the fit range is expressed in the number of divisions $M = \Delta y/\delta y$.

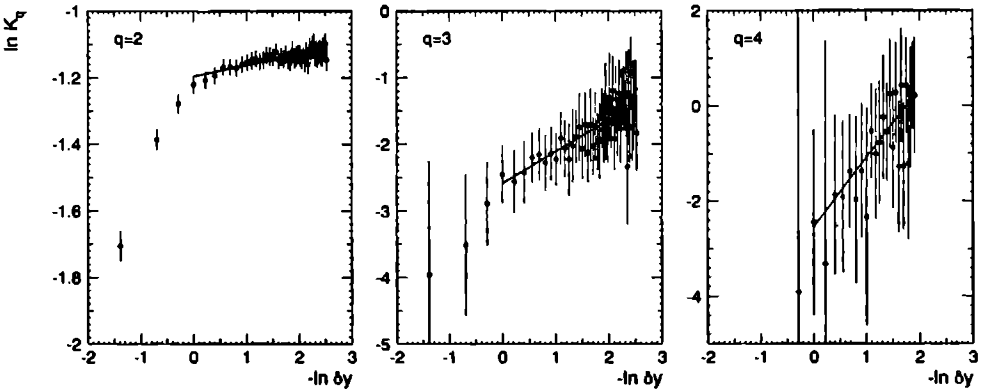

Figure 3.9: *Test of the power-law behavior of the normalized factorial cumulant moments.*

	ψ_2	ψ_3	ψ_4
fit range in M	$4-40$	$4-40$	$4-27$
data	0.033 ± 0.008	0.5 ± 0.1	1.5 ± 0.6
FRITIOF plain	-0.005 ± 0.007	0.20 ± 0.07	1.2 ± 0.5
FRITIOF + BE	0.015 ± 0.007	0.27 ± 0.05	1.3 ± 0.3

Table 3.4: *The slopes ψ_q obtained from the normalized factorial cumulant moments.*

While $K_2(\delta y)$ still flattens for smaller bin sizes, $K_3(\delta y)$ and $K_4(\delta y)$ are much more linear than the $F_q(\delta y)$ of the same order, but the errors are large. The consequently large errors on the slopes ψ_q (Tab. 3.4) do not allow to draw strict conclusions, but the ψ_q obtained from the data are systematically larger than those predicted by FRITIOF.

3.2.2.2 Contribution of multiparticle correlations

Formulae (3.60) and (3.61) can be used to investigate contributions of the lower-order particle correlations to the normalized factorial moments. In Fig. 3.10 $\ln F_q(\delta y)$ and $\ln F_q^{(p)}(\delta y)$ are shown as a function of $-\ln \delta y$. The errors on $\ln F_q^{(p)}(\delta y)$ are dropped for clearity.

The difference of $F_q(\delta y)$ and $F_q^{(p)}(\delta y)$ is a measure for the importance of higher-order correlations. The relative contribution of $F_q^{(p)}$ to F_q is shown in Fig. 3.11.

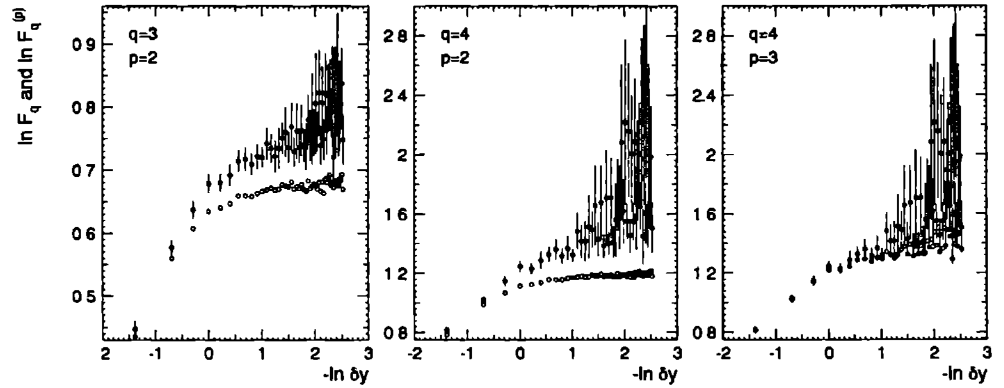

Figure 3.10: *Contribution of genuine lower-order correlations to normalized factorial moments.*

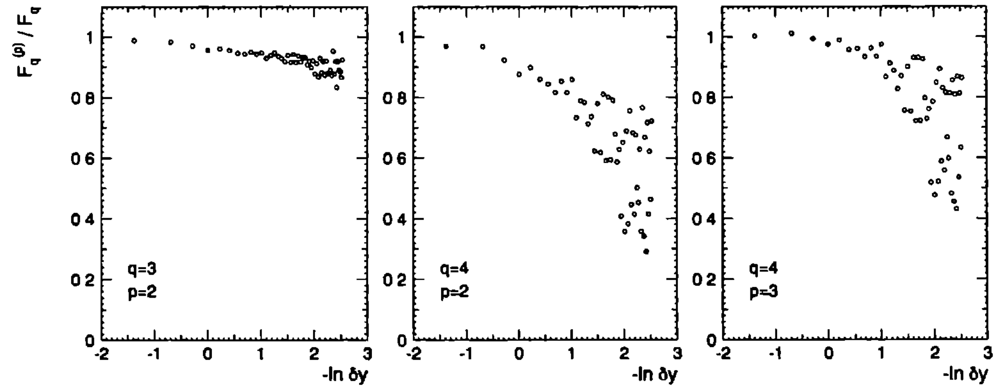

Figure 3.11: *Relative contribution of genuine lower-order correlations to normalized factorial moments.*

It is clear from figs. 3.10 and 3.11 that this difference increases with decreasing bin sizes, implying the growing contribution of higher-order correlations.

3.2.2.3 Test of the LPA

The Linked-Pair Approximation, described in Sect. 3.2.1.3, contains the parameters A_q expected to be constants independent of bin size. They are obtained via formulae (3.72) and tested for constancy in Fig. 3.12 (left two subfigures). Despite the large errors, one can not claim A_q to be independent of δy.

The dotted line in Fig. 3.12 represents the value one would find in case of a NBD. Clearly, this value is not supported by the data. However, the relation (3.80) is derived for a single bin only and obviously will only remain valid after bin averaging if $1/k$ is independent of the position of the rapidity bin. Unfortunately, Fig. 3.13a shows this condition not at all to be fulfilled in the NA22 data. Also $\bar{n}$ varies very strongly over Δy (Fig. 3.13).

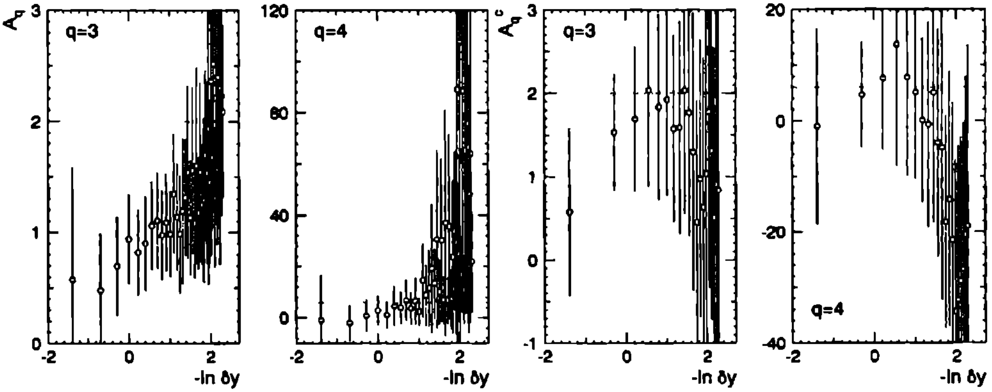

Figure 3.12: *The LPA parameters A_q for the bin averaged K_q (left) and for the central bin (right).*

The right part of Fig. 3.12 shows A^c_q versus $-\ln\delta y$, with A^c_q the value obtained for A_q with (3.71) in case m is the central bin. Now, the variation of $1/k$ and $K^{(m)}_q$ does not bother anymore. Nevertheless, even now A_q is not constant with respect to δy and the NBD-prediction still does not correspond with the data, but the errors are too large for a definite conclusion.

Figure 3.13c shows the difference between the bin-averaged $K_2(\delta y)$ and $1/k$ obtained from NBD-fits applied to the bin-averaged multiplicity distributions. For $M \geq 7$, $1/k$ is almost constant, while K_2 still increases with decreasing bin sizes.

It should be noted now that although the NBD usually fits multiplicity distributions quite well, even in restricted phase space domains, it still is only an approximation. Especially the tail of the distribution is not well reproduced, the probability for high multiplicities is underestimated by the NBD. When the phase space domain is decreased, also the number of degrees of freedom for the NBD-fit decrease and errors on the data points increase. One should, therefore, be careful with strong statements.

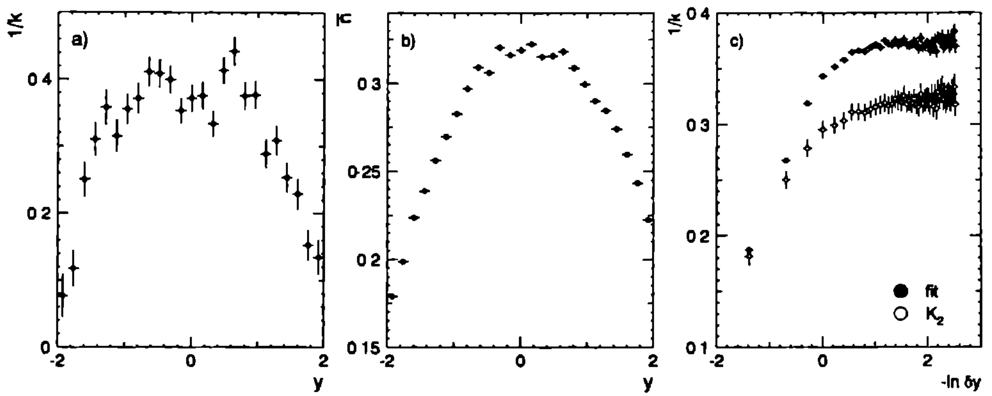

Figure 3.13: *The NBD parameters $1/k$ and $\bar{n}$ resulting from a fit of the multiplicity distributions in rapidity bins of size $\delta y = 0.16$ (subFig. a and b) and the parameter $1/k$ as obtained from the bin averaged $K_2 (= 1/k)$ and from a fit of the bin-averaged multiplicity distributions (subFig. c).*

Despite the above remarks, the NBD is a powerful parametrization and has proven to be very useful for a lot of applications. The breakdown of formula (3.80) cannot be interpreted as a failure of the NBD or as a contradiction with earlier NA22 publications on this subject ([FMTH87, NA22ZP]).

3.3 Factorial correlators

3.3.1 Formalism

3.3.1.1 Correlators of a theoretical density distribution

The single-variate density moments $\langle \rho_m^q \rangle_P$ (as defined in (3.3)) probe the density fluctuations locally in a bin m. However, additional information is contained in the correlations between the fluctuations in non-overlapping bins m and m' within a single event. These correlations can be measured by use of the bivariate moments

$$\left\langle \rho_m^q \rho_{m'}^{q'} \right\rangle_P = \int_0^\infty \cdots \int_0^\infty P(\rho_1, \ldots, \rho_M)\, \rho_m^q \rho_{m'}^{q'}\, \mathrm{d}\rho_1 \ldots \mathrm{d}\rho_M \quad . \tag{3.84}$$

It is clear from formulae (3.5) that the moment generating function $\mathcal{M}$ (defined as (3.4)) can be used to determine all multivariate density moments. In particular, the bivariate moments are obtained by

$$\left\langle \rho_m^q \rho_{m'}^{q'} \right\rangle_P = \left. \frac{\partial^{q+q'} \mathcal{M}(s_1, \ldots, s_m, \ldots, s_{m'}, \ldots, s_M)}{\partial s_m^q \partial s_{m'}^{q'}} \right|_{all\ s_i = 0} \quad . \tag{3.85}$$

In [BPNP88] it is proposed to normalize the bivariate moments as

$$Z^{(mm')}_{qq'} = \frac{\left\langle \rho^q_m \rho^{q'}_{m'} \right\rangle_P}{\langle \rho^q_m \rangle_P \left\langle \rho^{q'}_{m'} \right\rangle_P} \quad . \tag{3.86}$$

Following literature they are called the "correlators", here.

To get an idea of the features the correlators exhibit, one was guided by the predictions of the random-cascade model (3.1.1.4) as given in [BPNP88]. Although there is an inconsistency in this derivation of the correlator properties and its interpretation, it will be summarized below. A remark follows at the end of this subsection.

Recall that for a particular bin m

$$\rho_m(\delta) = W_\nu W_{\nu-1} \dots W_1 \rho(\Delta) \quad , \tag{3.87}$$

from which one obtaines the single-variate moments

$$\langle \rho^q_m(\delta) \rangle = \{W^q\}^\nu \langle \rho^q(\Delta) \rangle \quad . \tag{3.88}$$

Now, consider two paths in the cascade, one leading to bin m and the other to bin m'. Denote the number of steps after which the paths to m and m' separate by ν_0, as indicated in Fig. 3.14 for the case of the α-model ($\lambda = 2$). Define now the distance between m and m' after a total number of ν steps as

$$\mathcal{D} = \delta \lambda^{(\nu - \nu_0)} \quad . \tag{3.89}$$

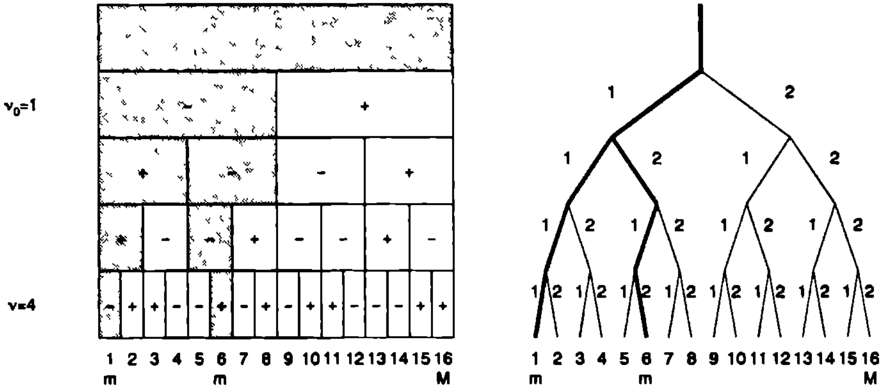

Figure 3.14: *Illustration of the correlators for the α-model. Here, ν_0 is the step after which the paths to m and m' separate.*

The bivariate moments of order qq' involving bins m and m' become

$$\left\langle \rho^q_m \rho^{q'}_{m'} \right\rangle_P = \{W^{q+q'}\}^{\nu_0} \{W^q\}^{\nu-\nu_0} \{W^{q'}\}^{\nu-\nu_0} \left\langle \rho^{q+q'}(\Delta) \right\rangle_P \tag{3.90}$$

and the correlators

$$Z_{qq'}^{(mm')} = \left(\frac{\{W^{q+q'}\}}{\{W^q\}\{W^{q'}\}} \right)^{\nu_0} \frac{\left\langle \rho^{q+q'}(\Delta) \right\rangle_P}{\langle \rho^q(\Delta) \rangle_P \langle \rho^{q'}(\Delta) \rangle_P} \quad . \tag{3.91}$$

This leads to

$$Z_{qq'}^{(mm')} \propto \mathcal{D}^{-\left(\ln\{W^{q+q'}\} - \ln\{W^q\} - \ln\{W^{q'}\} \right) / \ln\lambda} \propto \mathcal{D}^{-\phi_{qq'}} \quad , \tag{3.92}$$

i.e. the correlators exhibit a power-law behavior in $\mathcal{D}$ and are independent of the bin size δ. The power $\phi_{qq'}$ is the intermittency index or intermittency strength. Comparing (3.92) with (3.34) yields

$$\phi_{qq'} = \phi_{q+q'} - \phi_q - \phi_{q'} \quad . \tag{3.93}$$

In the log-normal approximation (3.40), this relation can be written as

$$\phi_{qq'} = qq'\phi_2 = qq'\phi_{11} \quad . \tag{3.94}$$

It was noted that the distance defined as (3.89) is the maximal distance possible between m and m' [FBPRIV]. This corresponds to the situation in which the path leading to m is obtained by taking the leftmost bin at each step after step ν_0 and to m' by taking the rightmost bin, i.e. bins 1 and 8 in Fig. 3.14. Actually $\mathcal{D}/\delta = \lambda^{(\nu-\nu_0)}$ is just the number of bins in which a bin of step ν_0 is divided at the end of the cascade, i.e. $\mathcal{D}$ is just the size of a bin at step ν_0.

However, in the second figure of their paper [BPNP88], Białas and Peschanski indicate a bin distance not corresponding to definition (3.92). To avoid confusion, this distance will here be denoted D. It is given by

$$D = (m' - m)\delta \quad , \tag{3.95}$$

simply the distance between the centers of bins m and m'. This inconsistency has caused the investigations to proceed with the distance as defined by (3.95). Despite this all, D is the distance measure also used in other fields of physics (e.g. quantum optics).

The power laws (3.34) and (3.92) can, after substitution of $\delta = \Delta\lambda^{-\nu}$ and (3.89), be written as

$$\ln Z_q \propto \nu \tag{3.96}$$

and

$$\ln Z_{qq'}^{(mm')} \propto \nu_0 \quad , \tag{3.97}$$

where Z_q has been averaged over all bins. Relations (3.96) and (3.97) are shown in Fig. 3.15a and b, respectively, for data generated with the α-model. In Fig. 3.15b no averaging over (mm') has been performed and the fluctuations of the random generator are visible as the variation of $Z_{qq'}^{(mm')}$ at constant ν_0-values. Obviously, these variations would disappear when averaging over an infinite number of events.

Since hereafter the bin distance will always be defined as (3.95), it is useful to check the behavior of $\ln Z_{qq'}^{(mm')}$ as function of $-\ln D/\delta$. The nice linear behavior on Fig. 3.15b now transforms to the parallel curves on Fig. 3.15c. The correlators of the random-cascade model do not support a power-law behavior in D.

If one determines the correlators experimentally for $M = l^\nu$, one can pretend them to be the result of a random-cascade generation of ν steps. A check of a power-law behavior in $\mathcal{D}$ (3.92) is now possible. It turns out the data do not exhibit this power-law behavior.

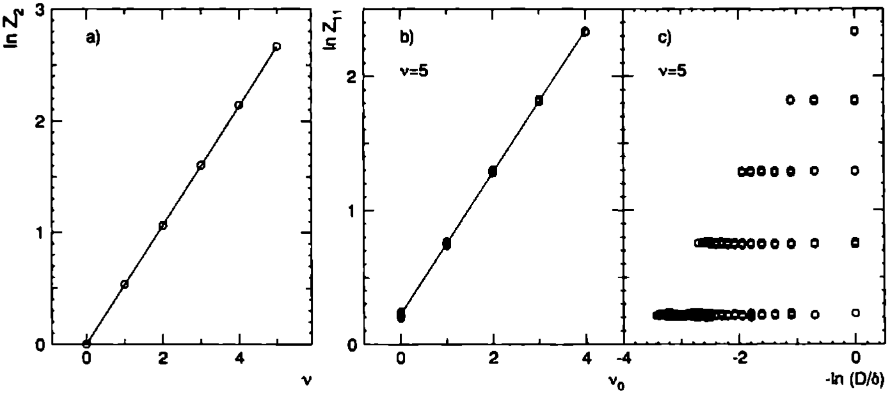

Figure 3.15: *The search for power laws in Monte-Carlo data obtained with the α-model, with parameter values* $a = 0.55$, $\beta_- = 0.25$ *and* $\rho(\Delta) = 1$.

3.3.1.2 Factorial correlators of an experimental multiplicity distribution

To remove the influence of a multi-Poissonian noise on the correlators, one has to apply the same tricks as for the single-variate moments.

Because of (3.14), the bivariate factorial moment is obtained from

$$\left\langle n_m^{[q]} n_{m'}^{[q']} \right\rangle_Q = \left. \frac{\partial^q \mathcal{F}(s_1, \ldots, s_m, \ldots, s_{m'}, \ldots, s_M)}{\partial s_m^q \partial s_{m'}^{q'}} \right|_{all\ s_i=1} \tag{3.98}$$

Combining this with (3.16) gives

$$\left\langle n_m^{[q]} n_{m'}^{[q']} \right\rangle_Q = \left\langle \rho_m^q \rho_{m'}^{q'} \right\rangle_P \delta^{q+q'} \ . \tag{3.99}$$

The factorial correlators are defined as

$$F_{qq'}^{(mm')} = \frac{\left\langle n_m^{[q]} n_{m'}^{[q']} \right\rangle_Q}{\left\langle n_m^{[q]} \right\rangle_Q \left\langle n_{m'}^{[q']} \right\rangle_Q} \ , \tag{3.100}$$

whence, using formulae (3.17) and (3.98),

$$Z_{qq'}^{(mm')} = F_{qq'}^{(mm')} \ . \tag{3.101}$$

In terms of inclusive multiparticle distributions, the bivariate factorial moments for separate bins m and m' can be written as (see Sect. 3.1.1.5)

$$\left\langle n_m^{[q]} n_{m'}^{[q']} \right\rangle_Q = \int_{\Omega_m^q} \mathrm{d}y_1 \ldots \mathrm{d}y_q \int_{\Omega_{m'}^{q'}} \mathrm{d}y_{q+1} \ldots \mathrm{d}y_{q+q'}\, \rho_{q+q'}(y_1, \ldots, y_q; y_{q+1}, \ldots, y_{q+q'}) \ . \tag{3.102}$$

While for overlapping bins ($\Omega_m^q = \Omega_{m'}^{q'}$) the expression on the right-hand side correctly yields the single-variate moment $\left\langle n_m^{[q+q']} \right\rangle$, the left-hand side equals $\left\langle n_m^{[q]+[q']} \right\rangle$.

For reasons of statistics $F_{qq'}^{(mm')}$ is averaged over all bin combinations with the same distance D, with D as indicated in Fig. 3.16. From definition (3.100) it is clear that the factorial correlators for $q \neq q'$ do not a priori need to be symmetric in q and q'. Therefore the quantity is symmetrized. After averaging and symmetrization, the factorial correlators are given by

$$F_{qq'}(D) = \frac{1}{2(M-k)} \sum_{m=1}^{M-k} \left(F_{qq'}^{(m,m+k)} + F_{q'q}^{(m,m+k)} \right) \quad , \tag{3.103}$$

where $M = \Delta/\delta$ and $k = D/\delta$.

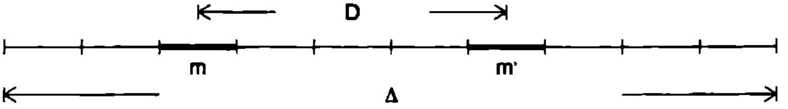

Figure 3.16: *Illustration of the quantities used for the determination of the factorial correlators.*

Inspired by the predictions of the random-cascade model, one examines the power-law behavior

$$F_{qq'}(D) \propto D^{-\phi_{qq'}} \tag{3.104}$$

and the bin-size independence of $F_{qq'}(D)$.

3.3.1.3 Sum rules

Suppose the initial interval Δ is divided into M bins of size $\delta = \Delta/M$ for the calculation of the bivariate factorial moments $\left\langle n_m^{[q]}(\delta) n_{m'}^{[q']}(\delta) \right\rangle$ and into $L = M/2$ bins of size 2δ for the determination of the single-variate factorial moments $\left\langle n_l^{[q]}(2\delta) \right\rangle$. Between the single-variate and the bivariate factorial moments then the following relation holds

$$\left\langle n_l^{[q]}(2\delta) \right\rangle = \left\langle (n_m(\delta) + n_{m+1}(\delta))^{[q]} \right\rangle = \sum_{q'=0}^{q} \binom{q}{q'} \left\langle n_m^{[q]}(\delta) n_{m+1}^{[q-q']}(\delta) \right\rangle \quad , \tag{3.105}$$

$$\text{with} \qquad m = 2l - 1 \quad , \qquad \text{for} \qquad l = 1, 2, \ldots, L \quad .$$

This relation is obtained by application of the binomial theorem generalized to factorial powers [HETH91].

In the particular case of translation invariance, (3.105) can be used to derive a relation between F_{11} and F_2 [RPJS90]. For $q = 2$, (3.105) becomes, after division by $\langle n_m \rangle \langle n_{m+1} \rangle$, (the indication (δ) has been omitted)

$$\frac{\left\langle (n_m + n_{m+1})^{[2]} \right\rangle}{\langle n_m \rangle \langle n_{m+1} \rangle} = \frac{\left\langle n_m^{[2]} \right\rangle}{\langle n_m \rangle \langle n_{m+1} \rangle} + \frac{\left\langle n_{m+1}^{[2]} \right\rangle}{\langle n_m \rangle \langle n_{m+1} \rangle} + \frac{2 \langle n_m n_{m+1} \rangle}{\langle n_m \rangle \langle n_{m+1} \rangle} \quad . \tag{3.106}$$

Since translation invariance has been assumed

$$\langle n_m \rangle \langle n_{m+1} \rangle = \langle n_m \rangle^2 = \langle n_{m+1} \rangle^2 = \frac{1}{4} \left\langle (n_m + n_{m+1})^2 \right\rangle \quad , \tag{3.107}$$

whence, after averaging over m

$$F_{11}(D, \delta = D) = 2F_2(2D) - F_2(D) \quad . \tag{3.108}$$

Here, $F_{11}(D, \delta)$ denotes the factorial correlator calculated for a distance D between the bins and for bin size δ. Guided by the predictions of the random-cascade model, one can state that relationship (3.108) holds for all bin sizes δ for which $F_{11}(D)$ is effectively independent of δ in the range $\delta \leq D \leq D_0$ [RPJS90].

3.3.2 Experimental results

3.3.2.1 The power-law behavior

The ln $F_{qq'}$ are shown as a function of $-\ln Dy$ in Fig. 3.17 for four values of δy (corresponding to $M = \Delta y/\delta y$ =10, 20, 30 and 40). While an estimate of $F_{qq'}$ is possible up to third order in both q and q' for a $\delta y = 0.4$ binning, statistics compels a restriction to first and second order at $\delta y = 0.1$. The smallest possible value for the bin distance Dy is the bin size δy. Since $Dy = k\,\delta y$ with $k = 1, M - 1$, also the number of distances is determined by the bin size. The larger the value of Dy, the less bin combinations can be taken into the average (3.103). Together with the available statistics, this determines the maximal bin distance for which it is meaningful to calculate $F_{qq'}$. For all four bin sizes, this maximum is considered to be $Dy = 2$.

In Fig. 3.17 an increase of $\ln F_{qq'}$ is observed with increasing $-\ln Dy$ (decreasing bin distance). However, this increase is not strictly linear: a clear bending can be seen, i.e. the power law (3.104) is only approximately valid in a restricted region. The values of $\phi_{qq'}$, obtained from the fit

$$\ln F_{qq'} = a_{qq'} + \phi_{qq'} \ln Dy \tag{3.109}$$

in the region $\delta y \leq Dy \leq 1.0$, are collected in Tab. 3.5 for the four different binnings. Since

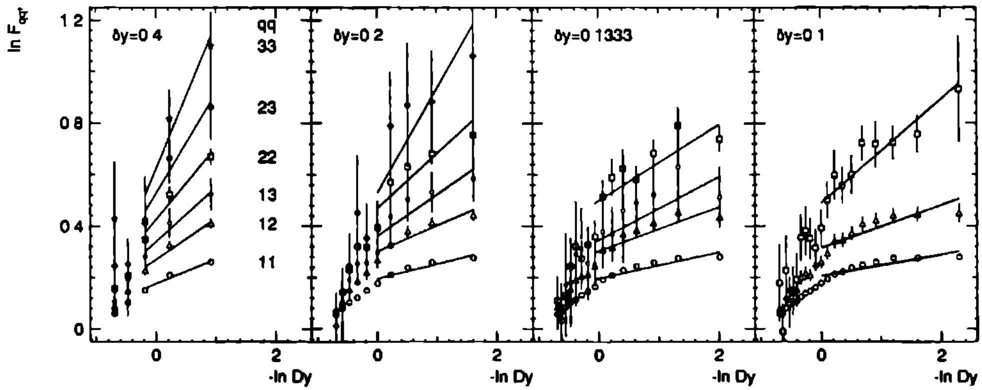

Figure 3.17: *The factorial correlators determined for four different values of δy.*

	ϕ_{11}	ϕ_{12}	ϕ_{22}
data			
$\delta y = 0.4$	0.10 ± 0.01	0.16 ± 0.02	0.28 ± 0.04
$\delta y = 0.2$	0.057 ± 0.006	0.10 ± 0.01	0.21 ± 0.04
$\delta y = 0.1333$	0.051 ± 0.004	0.085 ± 0.009	0.15 ± 0.03
$\delta y = 0.1$	0.042 ± 0.003	0.083 ± 0.009	0.20 ± 0.05
FRITIOF plain			
$\delta y = 0.4$	0.013 ± 0.006	0.027 ± 0.009	0.06 ± 0.02
$\delta y = 0.2$	−0.002 ± 0.003	−0.007 ± 0.006	−0.03 ± 0.02
$\delta y = 0.1333$	−0.000 ± 0.003	−0.003 ± 0.005	−0.02 ± 0.02
$\delta y = 0.1$	−0.004 ± 0.002	−0.014 ± 0.005	−0.03 ± 0.04
FRITIOF + BE			
$\delta y = 0.4$	0.027 ± 0.006	0.055 ± 0.009	0.11 ± 0.02
$\delta y = 0.2$	0.009 ± 0.003	0.017 ± 0.007	0.02 ± 0.02
$\delta y = 0.1333$	0.009 ± 0.003	0.015 ± 0.005	0.03 ± 0.02
$\delta y = 0.1$	0.006 ± 0.002	0.009 ± 0.005	0.03 ± 0.02

	ϕ_{13}	ϕ_{23}	ϕ_{33}
data			
$\delta y = 0.4$	0.21 ± 0.05	0.39 ± 0.07	0.56 ± 0.18
$\delta y = 0.2$	0.16 ± 0.04	0.41 ± 0.08	
$\delta y = 0.1333$	0.12 ± 0.04		
FRITIOF plain			
$\delta y = 0.4$	0.04 ± 0.02	0.09 ± 0.03	0.11 ± 0.08
$\delta y = 0.2$	−0.02 ± 0.02	−0.08 ± 0.03	
$\delta y = 0.1333$	−0.03 ± 0.02		
FRITIOF + BE			
$\delta y = 0.4$	0.09 ± 0.02	0.16 ± 0.03	0.21 ± 0.08
$\delta y = 0.2$	0.02 ± 0.02	0.03 ± 0.04	
$\delta y = 0.1333$	0.02 ± 0.02		

Table 3.5: *Intermittency indices obtained from the factorial correlators.*

the bending of $\ln F_{qq'}$ vs. $\ln Dy$ is more pronounced at smaller bin distances, the intermittency strength $\phi_{qq'}$ decreases for binnings with smaller δy, as then smaller (and more) values of Dy are available.

The predictions of FRITIOF with inclusion of BE-correlations for $\ln F_{qq'}$ vs. $-\ln Dy$ are plotted in Fig. 3.18. At $Dy = 2$ ($-\ln Dy = 0.69$) the factorial correlators are overestimated. The model values increase slower than the experimental data and at $Dy = 1$ ($-\ln Dy = 0$) the predicted values are already smaller than the experimental ones. At $-\ln Dy > 0$ the FRITIOF $F_{qq'}$ saturate strongly instead of just bending as in the data. As can be seen from Tab. 3.17, this translates into intermittency indices much smaller for FRITIOF than for the data.

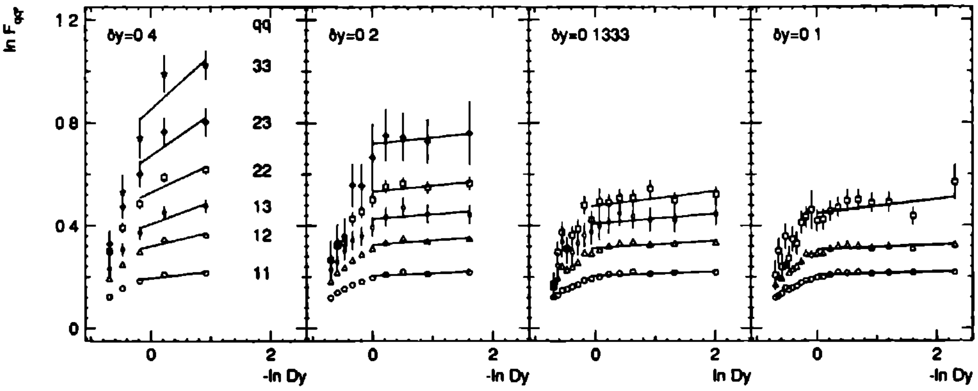

Figure 3.18: *The same as Fig. 3.17 for FRITIOF + BE-correlations.*

For comparison, also the values obtained with FRITIOF without BE-interference are included in Tab. 3.17. In this case, the $\phi_{qq'}$ are consistent with zero, except for the $\delta y = 0.4$ binning (due to the limited Dy-range available). relations (3.93) and (3.94) is tested.

In Fig. 3.19 the intermittency indices $\phi_{qq'}$ are shown for the four different binnings as a function of te product of the orders q and q'. The increase of $\phi_{qq'}$ with $q \cdot q'$ is close to linear. Furthermore, the validity of the first relationship is predicted by the the random-cascade model (rms) and as can be seen on the figure, it leads to an underestimation of $\phi_{qq'}$. If, in addition to the random-cascade model, the log-normal approximation is applied, one obtains formula (3.94). The failure of (3.94), visible on Fig. 3.19, is mainly due to an unjustified application of the log-normal approximation. In [ABZP91] this approximation has been shown to be valid only for the cases that the density fluctuations are weak or that the fluctuations of the cascade variable W have a log-normal distribution. The data, therefore, show that neither of these conditions is fulfilled.

The situation is somewhat different for the FRITIOF model (not shown). For both FRITIOF with and without BE-correlations, (3.93) yields an overestimation[2] of $\phi_{qq'}$. While (3.94) gives a good estimate of $\phi_{qq'}$ for FRITIOF + BE, it leads to an overestimation if

---

[2] Again the $\delta y = 0.4$ binning is an exception for reasons already mentioned.

BE-correlations are not introduced[3].

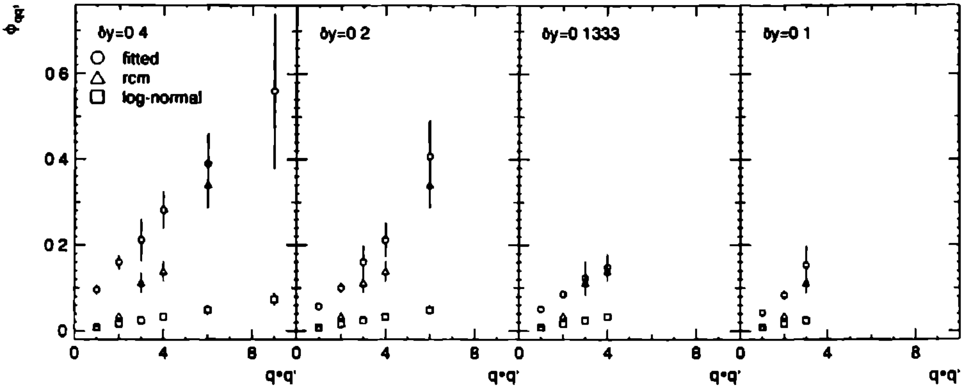

Figure 3.19: *The dependence of $\phi_{qq'}$ on the product $q \cdot q'$ (circles) compared with the behaviors predicted by the random-cascade model (triangles) and the random-cascade model in case of the log-normal approximation (squares).*

3.3.2.2 The bin-size independence

In Fig. 3.20a and b the $\ln F_{qq'}$ at fixed $Dy = 0.4$ and $Dy = 0.8$, respectively, are compared for the four different values of δy. The dashed lines correspond to a horizontal line fit through the points. As expected from the random-cascade model, the $F_{qq'}$ indeed do not depend on δy. For FRITIOF + BE, on the other hand, $\ln F_{qq'}$ tends to decrease with decreasing bin size.

The δy independence, however, is not unique to the random-cascade model. For F_{11} it can be extracted from the integral over the two-particle density, with two integration domains of size δy separated by Dy. Using the exponential short-range order [DWAP90], this gives

$$F_{11} - 1 \propto a^{-2} e^{-D/L} (e^{a} - 1) \left(1 - e^{-a}\right) \quad , \tag{3.110}$$

where L is a correlation length and $a = \delta y / L$. According to (3.110), F_{11} becomes independent of δy for $a < 1$. Since $\exp(-D/L) \to 1$ with $D \to 0$, this form also leads to deviations from the power law (3.104) observed as a bending in Fig. 3.17.

3.3.2.3 The sum rule

For the derivation of (3.108), one had to assume translation invariance of the density and correlations. Although this is not true for the rapidity distribution in the NA22 experiment, the values calculated via the sum rule (3.108)(stars on Fig. 3.21) agree reasonably well with $F_{11}(Dy)$ obtained directly from the data (circles on Fig. 3.21). It seems, the assumption of translation invariance does not weigh heavy in this case. For comparison, the $F_2(Dy)$ are

---

[3] idem

represented on fig 3.21 by the triangles. As could be expected from their definition, $F_2(Dy)$ and $F_{11}(Dy)$ converge for $Dy \to 0$.

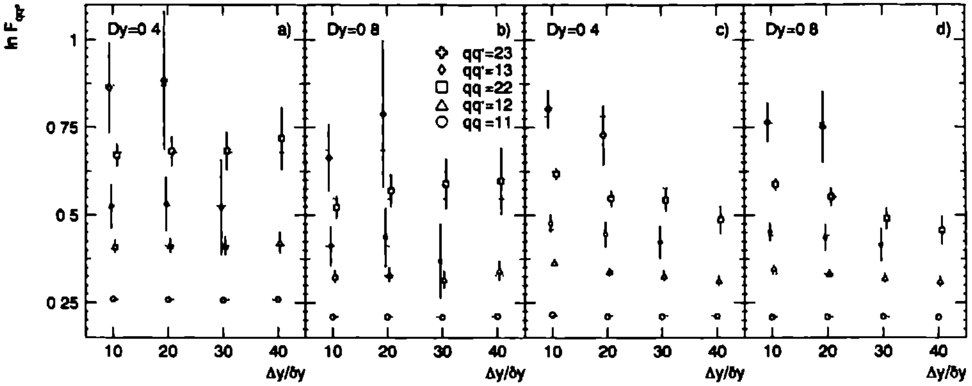

Figure 3.20: *Test of the δy independence at $Dy = 0.4$ and 0.8 for NA22 data (a) and b) respectively) and FRITIOF2.0 + BE predictions (c) and d)). The horizontal lines represent a horizontal fit through the data.*

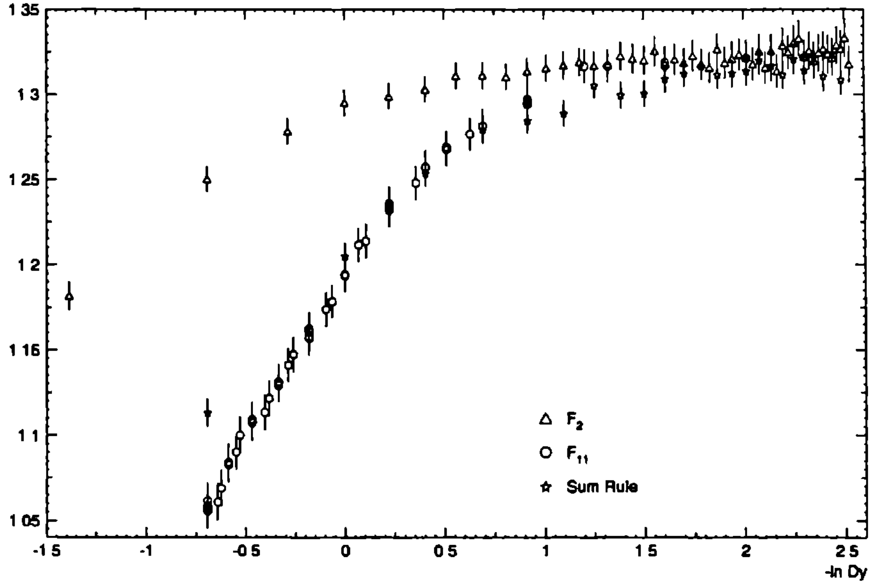

Figure 3.21: *Illustration of the sum rule (3.108)*

3.4 *G*-Moments: a first definition

3.4.1 Formalism

Based on the multifractal property (see Sect. 3.1.1.3)

$$\sum_{m=1}^{N(\delta)} p_m^q(\delta) \propto \delta^{(q-1)D_q} \quad , \tag{3.111}$$

the G-moments [JFED88, IDRE90, RHWA90, RHWA91],

$$G_q(\delta) = {\sum_{m=1}^{M}}' \left(\frac{n_m}{n}\right)^q \qquad \text{with} \qquad n = \sum_{m=1}^{M} n_m \quad , \tag{3.112}$$

are proposed to study the multifractal properties of the multiparticle production process. By definition, $N(\delta)$ corresponds to the number of non-empty bins. Therefore, also the sum of (3.112) runs only over non-empty bins. This restriction, unnecessary when only considering positive integer orders q, is denoted by the prime accompanying the summation sign. The probability p_m to find a particle in a particular bin m and the number of particles n_m in that bin are related by

$$p_m = \lim_{n\to\infty} \frac{n_m}{n} \quad . \tag{3.113}$$

Since the n_m/n are frequencies, the G-moments are known in statistics as frequency moments [KENSTU].

The scaling property of the G-moments is expressed as

$$G_q(\delta) \propto \delta^{\tau(q)} \qquad \text{with} \qquad \tau(q) = (q-1)D_q \quad , \tag{3.114}$$

with D_q as defined in (3.26). Experimentally, this power-law behavior cannot be true in the limit of $\delta \to 0$. Obviously, in that limit the number of particles n_m in a bin is either 0 or 1, forcing $G_q(\delta)$ to behave like

$$\lim_{\delta\to 0} G_q(\delta) \propto n^{1-q} \quad . \tag{3.115}$$

Suppose now $n \to \infty$. Consider the scaling behavior

$$p_m(\delta) \propto \delta^{\alpha} \tag{3.116}$$

within each bin m and group the bins depending on their α-value. The number of bins $N_\alpha(\delta)$ with a specific α is related to the density function $\rho(\alpha)$ by

$$N_\alpha(\delta) = \rho(\alpha)\delta^{-f(\alpha)} \quad , \tag{3.117}$$

with $f(\alpha)$ the fractal spectrum. The number of non-empty bins can then be written as

$$N(\delta) = \int \rho(\alpha)\delta^{-f(\alpha)}\mathrm{d}\alpha \quad . \tag{3.118}$$

The behavior of the G-moments themselves can now be exposed as

$$\begin{aligned} {\sum_{m=1}^{M}}' p_m^q(\delta) &\propto \int N_\alpha(\delta)\,(\delta^\alpha)^q\,\mathrm{d}\alpha \\ &= \int \rho(\delta)\delta^{(q\alpha-f(\alpha))}\mathrm{d}\alpha \end{aligned} \tag{3.119}$$

and this means

$$\delta^{\tau(q)} \propto \int \rho(\delta)\delta^{(q\alpha-f(\alpha))}\mathrm{d}\alpha \quad . \tag{3.120}$$

According to [THAL86, THMJ86, GPAV87] $\tau(q)$ and $f(\alpha)$ are related via the Legendre transform

$$f(\alpha) = q\alpha - \tau(q) \tag{3.121}$$

$$\alpha = \frac{\mathrm{d}\tau(q)}{\mathrm{d}q} \quad . \tag{3.122}$$

In the following some general properties of $f(\alpha)$ are discussed.

- Assume a flat distribution. In the limit $n \to \infty$ this means $p_m = 1/M$, with M the total number of bins. In terms of fractality, this leads to

  $$G_q(\delta) \propto \delta^{q-1} \qquad \Rightarrow \qquad \tau(q) = q-1 \qquad \Rightarrow \qquad \alpha = 1 \quad . \tag{3.123}$$

  The trivial behavior of the fractal spectrum in absence of any fractal structure, therefore, looks like

  $$f(\alpha) = \delta(\alpha - 1) \quad , \tag{3.124}$$

  where δ now stands for the δ-function.

- Substituting $q = 0$ in (3.121) gives

  $$f(\alpha_0) = -\tau(0) = 1 \quad , \tag{3.125}$$

  where the second equality holds if none of the bins is empty.

- Independent of the characteristics of the distribution under consideration,

  $$G_1(\delta) = 1 \qquad \text{and} \qquad \tau(1) = 0 \quad , \tag{3.126}$$

  consequently

  $$f(\alpha_1) = \alpha_1 \quad . \tag{3.127}$$

- The overall behavior of the fractal spectrum can be obtained from the derivatives

  $$\frac{\partial f(\alpha)}{\partial \alpha} = q \quad , \tag{3.128}$$

  $$\frac{\partial^2 f(\alpha)}{\partial \alpha^2} = \left(\frac{\partial^2 \tau(q)}{\partial q^2}\right)^{-1} \tag{3.129}$$

  Eq. (3.128) indicates an extremum in the fractal spectrum at $q = 0$. If $\tau(q)$ is a concave function of q, (3.129) requires this extremum to be a maximum and, therefore, $f(\alpha)$ to be a concave function of α. Assuming this behavior of $f(\alpha)$ and considering again (3.128), it is clear that the positive q-values correspond to the increasing (left-hand side) part of $f(\alpha)$ and the negative q-values to the decreasing (right-hand side) part. This proves $\alpha_{q_1} > \alpha_{q_2}$ when $q_1 < q_2$. If, on the contrary, $\tau(q)$ is a convex function of q, the extremum $f(\alpha_0)$ corresponds to a minimum and above results change into their opposites.

3.4.2 Experimental results

The formalism in the previous section considers only one event and a generalization to many events is needed. Contrary to the assumption of Sect. 3.1.1.3 that the power-law behavior of the moments still holds after event averaging, the autors of [RHWA90, RHWA91] propose to determine $\langle \ln G_q \rangle$ rather than $\langle G_q \rangle$, in order to extract an average value $\langle \tau(q) \rangle$ (as usual, the $\langle \ \rangle$ denote the event average).

The initial rapidity interval $\Delta y = [-2, 2]$ is divided into $M = 2^\mu$ bins of size δy. In Fig. 3.22a $\langle \ln G_q \rangle$ is shown versus $-\ln \delta y$. After an initial sharp increase, $\langle \ln G_q \rangle$ starts bending and staturates. Apparantly, power law (3.114) is not obeyed. The moments are limited by statistics and the saturation effect predicted by (3.115) already sets in at rather large bin sizes.

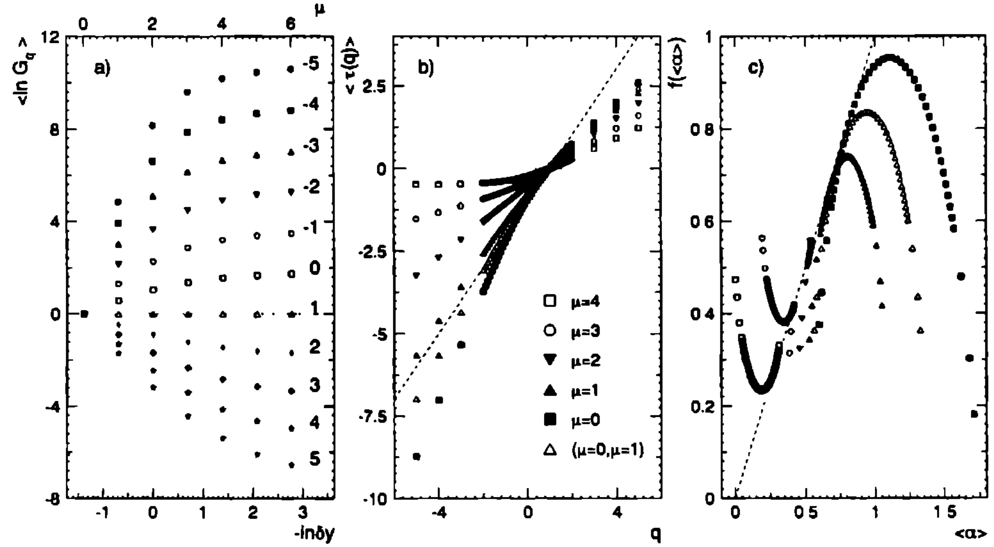

Figure 3.22: *a) The G-moments for orders $q = -5, \ldots, 5$; b) the average slopes $\langle \tau(q) \rangle$ determined at different $M = 2^\mu$ (see text) and obtained from a straight line through the moments at $\mu = 0$ and $\mu = 1$ (open triangles); c) the fractal spectrum for different μ-values, the symbols used in c) follow the same conventions as in b).*

In order to obtain the (δy-dependent) function $\tau(q)$, a third-order polynomial fit is applied to $\langle \ln G_q \rangle$ as a function of $-\ln \delta y$. The polynomial is forced to become zero for $\delta y = \Delta y$, where trivially $G_q = 1$ for all orders. Differentiating the third-order polynomial with respect to q then delivers $\langle \tau(q) \rangle$ in an analytical manner. This result is presented in Fig. 3.22b for $\mu = 1, \ldots, 4$. On the same plot $\langle \tau(q) \rangle$ acquired from the slope defined by the first two data points ($\langle \ln G_q \rangle$ at $\mu = 0$ and $\mu = 1$), is represented by the open triangles. For comparison to the behavior in case of absence of fractality, the dashed line $\tau(q) = q - 1$ is added to the figure.

Subsequently, (3.122) is approximated by taking very small differences in q ($\Delta q = 0.1$)

and is substituted into (3.121). The fractal spectrum obtained is shown in Fig. 3.22c. The dashed line corresponds to $f(\alpha_1) = \alpha_1$.

Comparing Fig. 3.22b and c one observes the behavior explained above: $\langle\tau(q)\rangle$ for $\mu = 0, 1$ as well as $\tau(q)$ obtained from the first two data points are concave functions of q and, consequently, $f(\langle\alpha\rangle)$ is a concave function of $\langle\alpha\rangle$; for $\mu = 3, 4$, however, $\langle\tau(q)\rangle$ is convex and so is $f(\langle\alpha\rangle)$; the almost linear increase of $\tau(q < 1)$ for $\mu = 2$ results in a quite strange behavior of $f(\langle\alpha\rangle)$.

3.5 G-Moments: an improvement

3.5.1 Formalism

From Sect. 3.4.2 it is clear that the G-moments are dominated by statistical fluctuations: due to the low average multiplicity the moments saturate at rather large bin sizes. To filter out bins containing a large number of particles, the G-moments are modified to [RHWA92]

$$G_q = \sum_{m=1}^{M} \left(\frac{n_m}{n}\right)^q \Theta(n_m, q) \tag{3.130}$$

with

$$\begin{aligned}\Theta(n_m, q) \;=\; & \{([q] + 1 - q)\delta(n_m - [q]) + (1 - \delta(n_m - [q]))\,\theta(n_m - q)\}\;\theta(q - 1) \\ & + (1 - \delta(q - 1))\,\theta(1 - q)\theta(n_m - 1)\quad .\end{aligned} \tag{3.131}$$

Here, $\theta(x)$ is the well-known step function which becomes zero as soon as its argument is negative and equals one for zero and positive x. The largest integer $\leq q$ is denoted $[q]$. The Θ-function is zero for empty bins, regardless of the value of q. For positive orders, Θ equals zero if $n_m < [q]$ and one if $n_m > [q]$. When q is increased past a positive integer value $[q]$, the contribution from a bin with $n_m = [q]$ diminishes linearly with $q - [q]$. For $q < 0$ definitions (3.112) and (3.130) coincide.

In order to extract the dynamical component, the authors of [RHWA92] now investigate $\langle G_q\rangle$ instead of the earlier proposed $\langle \ln G_q\rangle$ (Sect. 3.4.2). Now the power law

$$\langle G_q\rangle_{\mathrm{obs}} \propto \delta^{\tau_q^{\mathrm{obs}}} \tag{3.132}$$

has to be verified. The sub- and superscript "obs" indicates that these are quantities one observes directly from the data. Besides dynamics, $\langle G_q\rangle_{\mathrm{obs}}$ contains a statistical contribution and an influence of the shape of the single particle rapidity distribution. The statistical component $\langle G_q\rangle_{\mathrm{stat}}$ can be obtained by distributing the n particles of an event randomly according to the experimental rapidity spectrum in the initial interval and averaging over all events. This component now has contributions of trivial dynamics, statistical fluctuations and the shape of the rapidity distribution. Since the trivial dynamics are represented by a power-law behavior δ^{q-1} (see (3.123)), the dynamical component $\langle G_q\rangle_{\mathrm{dyn}}$ is given by

$$\langle G_q\rangle_{\mathrm{dyn}} = \frac{\langle G_q\rangle_{\mathrm{obs}}}{\langle G_q\rangle_{\mathrm{stat}}}\,\delta^{q-1} \quad . \tag{3.133}$$

In terms of the powers τ_q this becomes

$$\tau_q^{\rm dyn} = \tau_q^{\rm obs} - \tau_q^{\rm stat} + q - 1 \quad , \qquad (3.134)$$

i.e. any deviation of $\tau_q^{\rm obs}$ from $\tau_q^{\rm stat}$ results in a deviation of $\tau_q^{\rm dyn}$ from $q - 1$, this implies a dynamical contribution to $\tau_q^{\rm obs}$.

3.5.2 Experimental results

For negative orders G_q probes the holes in the rapidity distribution, for positive orders the peaks Since, in the NA22 experiment, the average multiplicity in $-2 < y < 2$ is only about 7, the holes are very dominating even for small M. It is, therefore, not very interesting to investigate negative q-values and, in the following, only results on positive orders will be shown.

In Fig. 3.23a $\ln \langle G_q \rangle_{obs}$ is shown for orders $q = 0, 0.2, \ldots, 5$. As expected, the saturation behavior has diminished with respect to Fig. 3.22a. However, the effect of the Θ-function on the non-integer orders is not exactly what one would like it to be: the moments tend to "group" towards $\left\langle G_{[q]} \right\rangle$. This results in a kind of oscillating behavior of $\tau(q)$ The values of $\tau(q)$ shown in Fig. 3.23b are obtained with the use of a third-order polynomial fit, a method analoguous to the one described in Sect. 3.4.2. A linear fit to $\ln \langle G_q \rangle$ versus $-\ln \delta y$ for $0.0625 \leq \delta y \leq 1$. (i.e. $2 \leq \mu \leq 6$) produces the slopes $\tau(q)$ presented in Fig. 3.23c.

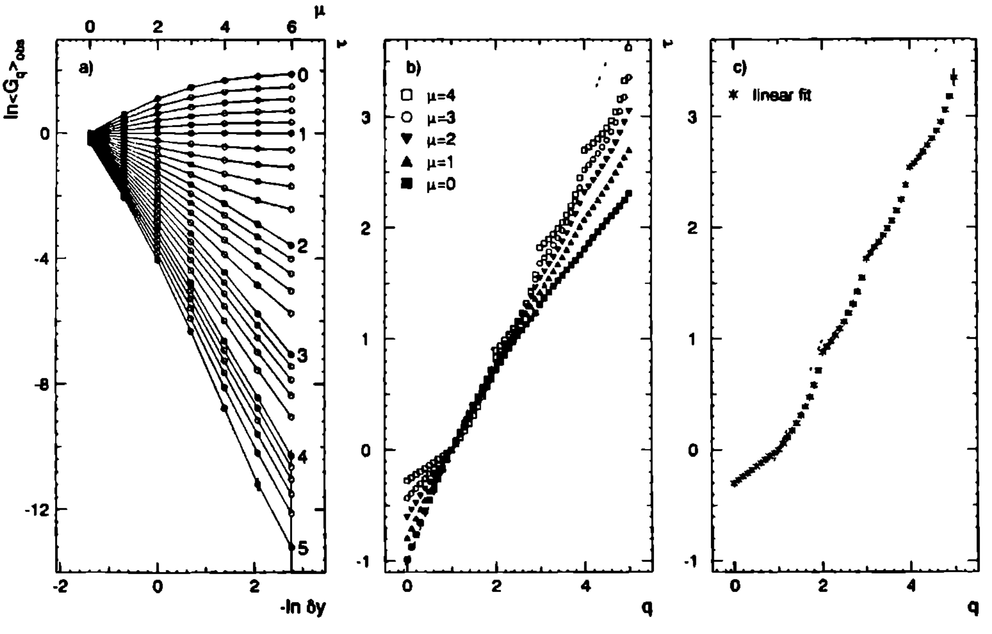

Figure 3.23: *a) The modified G-moments for $0 \leq q \leq 5$ (with steps of 0.2); b) the slopes $\tau(q)$ as obtained from a third-order polynomial and c) as obtained from a linear fit for $2 \leq \mu \leq 6$.*

It is clear, that this strange behavior was not the aim of the proposed modification. Further analyses will, therefore, be restricted to integer values of q.

In Fig. 3.24a and b, an effort is made to extract the dynamical component of $\langle G_q \rangle_{\text{obs}}$. The corresponding values of $\tau(q)$ are summarized in Fig. 3.24c. It is clear that $\langle G_q \rangle_{\text{obs}}$ and $\langle G_q \rangle_{\text{stat}}$ take values that differ very little, although the differences increase with increasing order. One should therefore not be surprised that the behavior of $\langle G_q \rangle_{\text{dyn}}$ is very close to δ^{q-1} (the dashed line in Fig. 3.24c), pointing out that there is almost no dynamical contribution in $\langle G_q \rangle_{\text{obs}}$. Despite the extension of definition (3.112) to (3.130), the dominance of statistical fluctuations is still a problem.

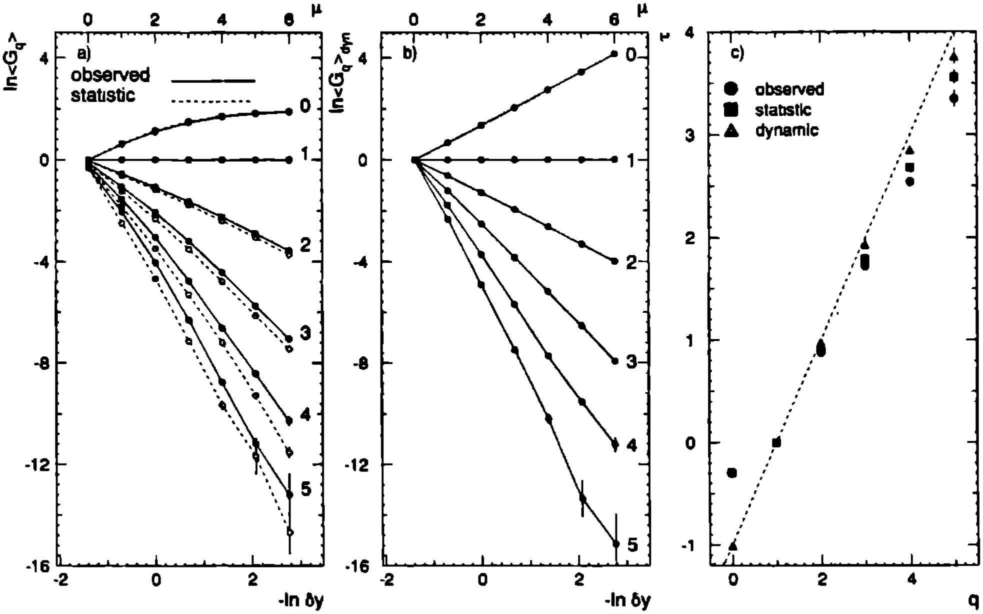

Figure 3.24: *a) The modified G-moments for* $q = 1, \ldots, 5$ *as observed from the data and its statistical component; b) the dynamical part of the modified G-moments; c) the slopes* $\tau(q)$ *obtained from a linear fit for* $2 \leq \mu \leq 6$.

In [DWDK93] the authors prove that if the n particles of an event, n according to some multiplicity distribution $P(n)$, are distributed independently over the bins with probability $1/M$; many of the multifractal properties seen in the data are reproduced and explained. If the data are dominated by statistical fluctuations, this trivial binomial multifractal behavior will be seen. Spreading the n particles randomly in the initial interval in order to obtain $\langle G_q \rangle_{\text{stat}}$ only destroys short-range correlations,. but the Bernoulli-nature of the particle repartition and consequently the noise-induced multifractal behavior remain. These considerations hold for both (3.112) and (3.130).

3.6 Conclusions

- The power-law behavior predicted by the random-cascade model for the normalized factorial moments $F_q(\delta y)$ as a function of decreasing bin size δy, only holds approximately and in a restricted region ($0.1 \leq \delta y \leq 1$). The intermittency indices ϕ_q increase with increasing order q.

  The indices do not increase by a factor 2 when restricting the sample to positively charged or negatively charged particles, as expected from Bose-Einstein type correlations [MGYU92]. Conform to the model, this indicates other sources besides Bose-Einstein correlations to be co-responsible for the increase of the moments.

  The intermittency effect in rapidity seems the strongest for the low-p_T sample ($p_T <$ 0.15 GeV/c) and the weakest for the high-p_T sample ($p_T >$ 0.30 GeV/c).

  The FRITIOF2.0 model (with and without incorporation of the BE-correlations) underestimates the normalized factorial moments and the intermittency indices. The model is not able to predict the influence of the restriction to like-charged samples correctly, nor does it yield the correct p_T-dependence.

- The investigation of the normalized factorial cumulant moments $K_q(\delta y)$ gives clear evidence for the existence of genuine multiparticle correlations. The data do not contradict the scaling hypothesis for $K_q(\delta y)$.

  The linked-pair approximation is not applicable in NA22: The model parameters A_q are not independent of the bin size, neither for the bin-averaged case, nor for bins centered around $y = 0$.

  The A_q do not obtain the value predicted by the NBD, neither is K_2 equal to $1/k$ obtained from a NBD fit applied to the bin-averaged multiplicity distribution.

  The large errors on the K_q are a serious drawback. In sec. 5 the star integrals will be introduced. These are a good tool to measure the genuine higher-order correlations without suffering from large errors. FRITIOF underestimates the values of K_q and the slopes ψ_q.

- The random-cascade model predicts the factorial correlators $F_{qq'}$ to exhibit a power-law dependence on the bin distance $\mathcal{D}y$ and to be independent of the bin size δy. However, the distance $\mathcal{D}y$ used to derive this features does not correspond to the distance Dy used in experiments to investigate the $F_{qq'}$.

  In a restricted region ($\delta y \leq Dy \leq 1.0$), $F_{qq'}$ depends approximately power-law like on the bin distance Dy. Furthermore, $F_{qq'}$ turns out to be independent of the bin size δy.

  The intermittency indices $\phi_{qq'}$ increase approximately linearly with increasing $q \cdot q'$. However, the increase is much stronger than expected from the random-cascade model combined with the log-normal approximation.

  In case of translational invariance, a relation can be derived between F_2 and F_{11}. Although the NA22 rapidity spectrum does not fulfil this condition, this relationship is rather well obeyed.

  As for the other investigated quantities, FRITIOF underestimates the correlations and the slopes.

- Despite all efforts, the G-moments are dominated by statistical noise at the NA22 energy, and are, therefore, not well suited to reveal the fractal properties of the multiparticle production process.

Bibliography

[ABZP91] J.M. Alberty and A. Bialas, Z. Phys. **C50** (1991) 315.

[ACWS90] A. Capella et al., Festschrift Léon Van Hove, A. Giovannini and W. Kittel (eds.), p. 413, Singapore, World Sientific 1990.

[ALEP92] D. Buskelic et al. (ALEPH), Phys. Lett. **B292** (1992) 210.

[BPNP86] A. Bialas and R. Peschanski, Nucl. Phys. **B273** (1986) 703.

[BPNP88] A. Bialas and R. Peschanski, Nucl. Phys. **B308** (1988) 857.

[DWAP90] E.A. De Wolf, Acta Phys. Pol. **B21** (1990) 611.

[DWDK93] E.A. De Wolf, I.M. Dremin, W. Kittel, Scaling Laws for Density Correlations and Fluctuations in Multiparticle Dynamics; HEN-362 (1993), IIHE-93.01, FIAN/TD-09/93.

[EDWP92] E.A. De Wolf, Proc. XXII Int. Symp. on Multiparticle Dynamics, Santiago de Compostela, Spain, July 1992, edt. C. Pajares, (World Scientific, Singapore 1993) p.263.

[FBPRIV] F. Botterweck, private communication.

[FBTH92] F. Botterweck, Ph.D. Thesis, Univ. of Nijmegen (1992).

[FMTH87] F. Meijers, Ph.D. Thesis, Univ. of Nijmegen (1987).

[FRIT87] B. Nilsson-Almqvist and E. Stenlund, Comput. Phys. Commun. **43** (1987) 387; B. Andersson, G. Gustafson and B. Nilsson-Almqvist, Nucl. Phys. **B281** (1987) 289; B. Andersson, G. Gustafson and B. Nilsson-Almqvist, A high energy string dynamical model for hadronic interactions, LUND preprint, LU-TP 87-6 (1987).

[GPAV87] G. Paladin and A. Vulpiani, Phys. Rep. **156** (1987) 156.

[HETH91] H. Eggers, Ph.D. thesis, Univ. of Arizona, 1991.

[HEPR91] H. Eggers et al., Phys. Rev. **D44** (1991) 1975.

[IDRE90] I.M. Dremin, Sov. Phys. Uspekhi **160** (1990) 647.

[JACE83] T.H. Burnett, Phys. Rev. Lett. **50** (1983) 2062.

[JFED88] J. Feder, Fractals, Plenum Press, N.Y. and London, 1988.

[KENSTU] M. G. Kendall and A. Stuart, The Advanced Theory of Statistics, Vol. 1-3, Charles Griffin & Company Limited, London, 1967.

[KHSM63] K. Huang: Statistical Mechanics, John Wiley and Sons, 1963.

[LBPL89] P. Lipa and B. Buschbeck, Phys. Lett. **B223** (1989) 465.

[MAND82] B. Mandelbrot, The Fractal Geometry of Nature, Freeman, N.Y.,1982.

[MGYU92] M. Gyulassy: Festschrift L. Van Hove, A. Giovannini and W. Kittel (eds.), P.479, Singapore: World Sientific 1992.

[MUEL71] A.H. Mueller, Phys. Rev. **D4** (1971) 150.

[NA2287] M. Adamus et al. (NA22), Phys. Lett. **B185** (1987) 200.

[NA2292] M. R. Atayan et al. (NA22), Z. Phys. **C54** (1992) 247.

[NA22PL] M. Adamus et al. (NA22), Phys. Lett. **B177** (1986) 239; **B205** (1988) 401.

[NA22ZP] M. Adamus et al. (NA22), Z. Phys. **C37** (1988) 215.

[NBDR88] C. Fuglesang, Prc. XIX Int. Symp. on Multiparticle Dynamics, Arles, 1988, p. 257; D. Schiff, j. Tran Thanh Van (eds.), Signapore, World Scientific.

[PVPR87] G. Paladin and A. Vulpani, Phys. Rep. **156** (1987) 147.

[PLTH90] P. Lipa, Intermittency in Antiproton-Proton Collisions, Ph.D. thesis Univ. of Vienna, HEPHY-PUB 542/90, 1990.

[RENY70] A. Rényi, Probability Theory, North-Holland, 1970.

[RHWA90] R.C. Hwa, Phys. Rev. **D41** (1990) 1456.

[RHWA91] C.B. Chiu and R.C. Hwa, Phys. Rev. **D43** (1991) 100.

[RHWA92] R.C. Hwa and J. Pan, Phys. Rev. **D45** (1992) 1476.

[RPJS90] R. Peschanski and J. Seixas, Scaling relations between fluctuations and correlations in multiparticle production, CERN-TH-5903/90, DF/IST-3.90.

[RPSF90] R. Peschanski, Why and How to Normalize the Factorial Moments of Intermittency, Contribution to the Santa Fe workshop on Intermittency in High Energy Collisions, 1990, editors F. Cooper, R. C. Hwa, I. Sarcevic, World Scientific.

[PBPL91] P. Bozek and M. Ploszajcak, Phys. Lett. **B271** (1991) 243.

[PCPL91] P. Carruthers et al., Int. J. Mod. Phys. **A6** (1991) 3031.

[PCPR89] P. Carruthers et al., Phys. Lett. **B254** (1991) 258.

[THAL86] T.C. Halsey et al., Phys. Rev. **A33** (1986) 1141.

[THMJ86] T.C. Halsey and M.H. Jensen, Physica **23D** (1986) 112.

[TSJO82] T. Sjöstrand, Comp. Phys. Comm. **27** (1982) 243.

[TSMB87] T. Sjöstrand and M. Bengtsson, Comp. Phys. Comm. **43** (1987) 367.

[UA5C84] G.J. Alner et al. (UA5), Proc. 4th Topical Workshop on $p\bar{p}$ Collider Physics Bern 1984, CERN 84-09 (1984) 286.

[UA5P84] G.J. Alner et al. (UA5), Phys. Lett. **B138** (1984) 304.

[UA5P85] G.J. Alner et al. (UA5), Phys. Lett. **B160** (1985) 193; ibid. 199.

[UA5P87] G.J. Alner et al. (UA5), Phys. Rep. **154** (1987) 247.

[VKSPPC] N. G. van Kampen, Stochastic processes in physics and chemistry, North-Holland Physics Publishing, 1st edition, 1981.

[WMDICT] W. J. Metzger, Statistical Methods in Data Analysis, Nijmegen preprint HEN-343, 1991.

[WWPL92] W.D. Walker et al., Phys. Lett. **B255** (1991) 155.

4

Multidimensional analysis

4.1 Motivation

Already in [BPNP86, BPNP88] the authors mentioned that intermittency could be explained in terms of cascading. However, the first attempt to interprete multiparticle production in terms of scale invariant branching processes was given by [POLY71]. Based on this paper, the authors of [WOJW88] suggest a jet model with a scale invariant cascade structure. They introduce the term pencil jet: a group of strongly collimated particles, clustered in both rapidity y and azimuthal angle φ. This clustering would cause the intermittency strength to increase if the normalized factorial moments are calculated in two-dimensional $y - \varphi$ grids instead of in one-dimensional binnings in y. In particular for $q = 2$, the model predicts an increase by a factor six. This prediction is tested for NA22 data in [NA2290, EDBE89, FBTH92]. The intermittency indices indeed increase when going to two-dimensional analysis; however, the predicted factor six is not reached. Moreover, the particular events with a dense cluster in y, have their particles widely spread in φ [EDBE89].

The facts that the one-dimensional factorial moments only exhibit approximate power-law dependence on the bin size and that the two-dimensional intermittency indices increase w.r.t. the one-dimensional indices, inspired W. Ochs [WOCH90] to investigate the three-dimensional α-model and its lower-dimensional projections. It turns out that the power law generated by the three-dimensional α-model is distorted when considering the lower-dimensional projections.

Bialas and Seixas [ABJS90] use two- and three-dimensional density distributions with a singularity in the squared four-momentum difference Q^2 to generate the intermittency effect. Studied in lower dimensions saturation of the moments is observed. This is called the projection effect. It reflects the loss of information when the three-dimensional multiparticle production process is projected onto lower-dimensional phase spaces. It reminds of the shadow of a tree which does not reveal much of the structure of the branches. A one-dimensional analysis is even worse: the shadow is projected on a line...

A plausible choice of variables to perform the three-dimensional analysis is the set of rapidity y, azimuthal angle φ and transverse momentum p_T. However, the exponential shape of the inclusive p_T-distribution causes troubles: In certain bins, the average multiplicity will be very small, causing unstable calculations due to limited computational precision. Besides, one could wonder how meaningful remains the bin averaging in an exponentially changing environment.

A solution for this problem is proposed simultaneously by Ochs [WOCH91] and Białas and Gazdzicki [ABMG90]. The authors propose a method to transform the non-flat inclusive distribution into a completely flat distribution. For any one-dimensional phase-space variable y, this is simply accomplished by introducing the normalized cumulative variable

$$X(y) = \frac{\int_{y_{min}}^{y} \rho(y')\,\mathrm{d}y'}{\int_{y_{min}}^{y_{max}} \rho(y')\,\mathrm{d}y'} \quad . \tag{4.1}$$

The distribution $\rho(y)$ in the initial interval $\Delta y = [y_{min}, y_{max}]$ is now transformed into a flat distribution $\rho\left(X(y)\right)$ in the interval $\Delta X = [0,1]$.

For multidimensional phase space, the method proposed by Ochs and the one proposed by Białas and Gazdzicki diverge. Ochs suggests to flatten the three one-dimensional projections of the three-dimensional density distribution, i.e. transforming the three variables y, φ and p_T according to (4.1) independently. Białas and Gazdzicki prefer to flatten the three-dimensional density distribution itself. The method proposed only involves simple mathematics, but is very nasty to implement. An algorithm exists for the case no event weights are taken into account [PODO90], but it is not clear how this algorithm should be generalized for the use of event weights.

Clearly, both prescriptions ([WOCH91] and [ABMG90]) yield the same results if the three-dimensional density function factorizes

$$\rho(y,\varphi,p_T) = \rho(y)\rho(\varphi)\rho(p_T) \quad . \tag{4.2}$$

Unfortunately, experimental investigation proves the variables to be correlated [FBTH92]. As a consequence, the three-dimensional distribution obtained via the Ochs method is not completely flat. This residual non-flatness can be corrected for by using *vertical* factorial moments.

In [FBTH92] the Ochs method and the Białas and Gazdzicki method are compared for unweighted events. Both methods lead to approximately the same values of the factorial moments. There is, therefore, no need to use the complex method of Białas and Gazdzicki and to discard the event weights.

In this chapter the variables y, φ and $\ln(p_T^2)$ are transformed according to (4.1). The initial interval used in all cases is given by

$$\begin{array}{rcccl} -2 & \leq & y & \leq & 2 \\ 0 & \leq & \varphi & \leq & 2\pi \\ -18 & \leq & \ln(p_T^2) & \leq & 6 \quad . \end{array} \tag{4.3}$$

Since no untransformed variable will be used in the following, the transformed variables will be referred to by their parent symbol without the risk of confusion.

The multidimensional factorial moments are described in sec. 4.2, the multidimensional factorial cumulants moments in sec. 4.3 and the multidimensional factorial correlators in sec. 4.4.

4.2 Factorial moments

4.2.1 Formalism

Consider an initial d-dimensional interval $\Delta = \Delta x_1 \ldots \Delta x_d$ ($= [0,1]$), with x_i one of the (transformed) variables y, φ and p_T. Dividing each one-dimensional interval Δx_i into M bins of size $\delta x_i = \delta_l$ ($= M^{-1}$) yields M^d d-dimensional boxes of size $\delta = \delta x_1 \ldots \delta x_d = \delta_l^d$ ($= M^{-d}$). The one-dimensional factorial moments of (3.18) can now be generalized to d dimensions via

$$F_q(\delta) = \frac{1}{M^d} \sum_{m=1}^{M^d} \frac{\left\langle n_m^{[q]} \right\rangle}{\langle n_m \rangle^q} \quad . \tag{4.4}$$

The intermittency index ϕ_q is defined by

$$F_q(\delta) \propto \delta^{-\phi_q} \quad , \tag{4.5}$$

or in terms of the linear size δ_l of the d-dimensional box

$$F_q(\delta_l^d) \propto \delta_l^{-d\phi_q} \propto \delta_l^{-\Phi_q} \quad . \tag{4.6}$$

The parameter Φ_q is needed for the generalization of the link between intermittency and fractality described in sec. 3.1.1.3, however, most often ϕ_q is used in intermittency analyses. Call $N(\delta_l)$ the number of d-dimensional pieces of size δ_l^d needed to cover the fractal object and p_m the probability to be in piece $N_m(\delta_l)$. The average q-th order moments in case of a monofractal is given by

$$[p_m^q(\delta_l)] = \delta_l^{qD_F} \tag{4.7}$$

and in case of a multifractal by

$$\sum_{m=1}^{N(\delta_l)} p_m^q(\delta_l) = \left[p_m^{q-1}(\delta_l)\right] = \delta_l^{(q-1)D_q} \quad . \tag{4.8}$$

An example of a multidimensional fractal is the monofractal two-dimensional Cantor set (Fig. 4.1) with fractal dimension $D_F = \ln 8 / \ln 9$.

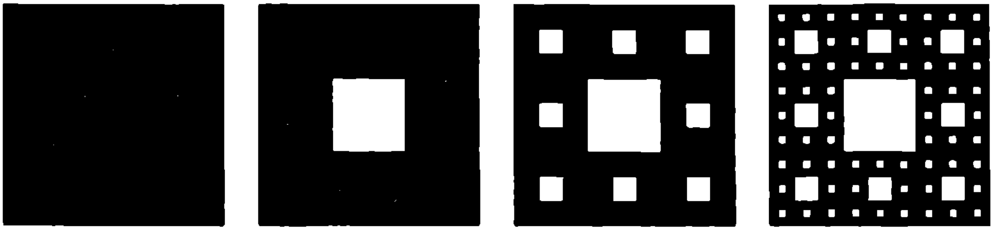

Figure 4.1: *The two-dimensional Cantor set.*

For a d-dimensional intermittency analysis, $\delta_l \propto M^{-1}$, $N(\delta_l) = M^d$ and $p_m(\delta_l)$ is the probability to find a particle in bin m. Supposing relation (4.8) holds after bin averaging and assuming a completely flat inclusive distribution, one finds

$$\begin{aligned} C_q(\delta_l) &:= \left\langle \frac{1}{M^d} \sum_{m=1}^{M^d} (M^d p_m(\delta_l))^q \right\rangle \\ &= M^{d(q-1)} \left\langle \sum_{m=1}^{M^d} (p_m(\delta_l))^q \right\rangle \\ &\propto M^{\Phi_q} \\ &\propto M^{d(q-1)} M^{(1-q)D_q} \quad , \end{aligned} \tag{4.9}$$

whence

$$D_q = d - \frac{\Phi_q}{q-1} = d - d_q \quad . \tag{4.10}$$

The anomalous dimension d_q measures the deviation from the topological dimension d.

If intermittency is present in the three-dimensional multiparticle production process, power-law (4.5) is not expected to be exact for the lower-dimensional projections. However, Ochs and Wosiek [WOJW88, WOCH91] claim the projections "remember" their intermittent origin. This results in a modified power law

$$F_q(\delta) \propto (g(\delta))^{\alpha_q} \quad , \tag{4.11}$$

being equivalent to

$$\ln F_q(\delta) = a_q + \frac{\alpha_q}{\alpha_2} \ln F_2(\delta) \quad . \tag{4.12}$$

The order dependence of α_q/α_2 can reveal some properties of the underlying dynamics. If intermittency is due to a second-order phase transition at a critical temperature, this would correspond to a monofractal structure yielding [HSAT89]

$$\frac{\alpha_q}{\alpha_2} = q - 1 \quad . \tag{4.13}$$

The observation of such a monofractal behavior may indicate the formation of a quark-gluon plasma.

With the random cascade model, a multifractal structure is generated. In this case, the behavior of α_q/α_2 can be predicted by approximating the density distribution either by the log-normal distribution or the Lévy stable law. If one assumes the log-normal approximation to be valid one finds [BPNP88]

$$\frac{\alpha_q}{\alpha_2} = \frac{q}{2}(q-1) \quad . \tag{4.14}$$

However, the log-normal approximation is shown often not to be applicable [JAAB91]. Therefore, Brax and Peschanski use the Lévy stable law, yielding a more accurate result [PBRP91]

$$\frac{\alpha_q}{\alpha_2} = \frac{q^\mu - q}{2^\mu - 2} \quad . \tag{4.15}$$

The authors claim the Lévy index μ characterizes the processes causing the intermittency pattern. If $0 < \mu < 1$ a thermal phase transition interspersed in the cascade process has occurred.

For the regions $\mu \leq 0$ and $\mu > 2$, the Lévy stable law is not applicable. However, for $\mu = 0$ (4.13) coincides (4.15). If $\mu = 2$, the distribution is Gaussian and (4.15) reduces to (4.14).

Another approach to the characteristics of the ratio α_q/α_2 is presented by Hwa and Nazirov in [RHTN92, JPRH92, JPRH93]. The authors investigate the properties of intermittency in the framework of the Ginzburg-Landau description of phase transitions and come up with the order dependence

$$\frac{\alpha_q}{\alpha_2} = (q-1)^{\nu} \quad . \tag{4.16}$$

The scaling exponent ν is an universal number independent of the details of the system. In the Ginzburg-Landau theory $\nu = 1.304$ holds for a phase transition. If ν is found to differ significantly from this value, the Ginzburg-Landau description is inapplicable and a second-order phase transition is excluded.

4.2.2 Experimental results

The multidimensional factorial moments are studied already in [FBTH92]. In this, section the main results are recapitulated and new FRITIOF2.0 results are added as well as fit results obtained with (4.16).

If the factorial moments strictly follow the power law (4.5), this would be visible on a $\ln F_q$ vs. $\ln M$ plot as a straight line of slope $\Phi_q = d\phi_q$. However, as can be seen on Fig. 4.2, there is no linear dependence of $\ln F_q$, whatever the number of dimensions or which variable(s) used.

While the factorial moments in y and in p_T show a downward curvature before saturating, the factorial moments in φ first decrease, curve upward and saturate. It is believed that this behavior is caused by local momentum conservation and resonances, producing particles far apart from each other in azimuth. The influence of φ is still visible in the two-dimensional factorial moments in φ-p_T and to less extent in the moments in y-φ. They both exhibit an upward curvature while the F_q in y-p_T slightly curve downwards. The saturation visible for the one-dimensional factorial moments vanishes when performing the analysis in two or three dimensions. The increase of the moments with the linear size of the d-dimensional boxes (equal to $1/M$) is clearly the strongest for the three-dimensional case. The upward curvature of the three-dimensional factorial moments means that the increase is faster than a power law.

Because of the absence of linearity in Fig. 4.2, fits are not presented on the figure. However, the intermittency indices ϕ_q are summarized in Tab. 4.1, purely to quantify the increase and to compare the behavior in different phase spaces. The fits are performed in the region M = 4-40 for the one-dimensional factorial moments, M = 5-18 for the two-dimensional case and $M = 1, 10$ for the three dimensional analysis. The upper limits are reduced if the $F_q(M)$ become zero. The two-dimensional ϕ_4 and ϕ_5 are not given because of too large errors on the fit parameters. For second order, the intermittency index increases if the analysis is extended to more dimensions. Nevertheless, ϕ_q obtained for y increases much faster with increasing order than the three-dimensional ϕ_q and for $q = 4, 5$ $\phi_q(y)$ is larger than

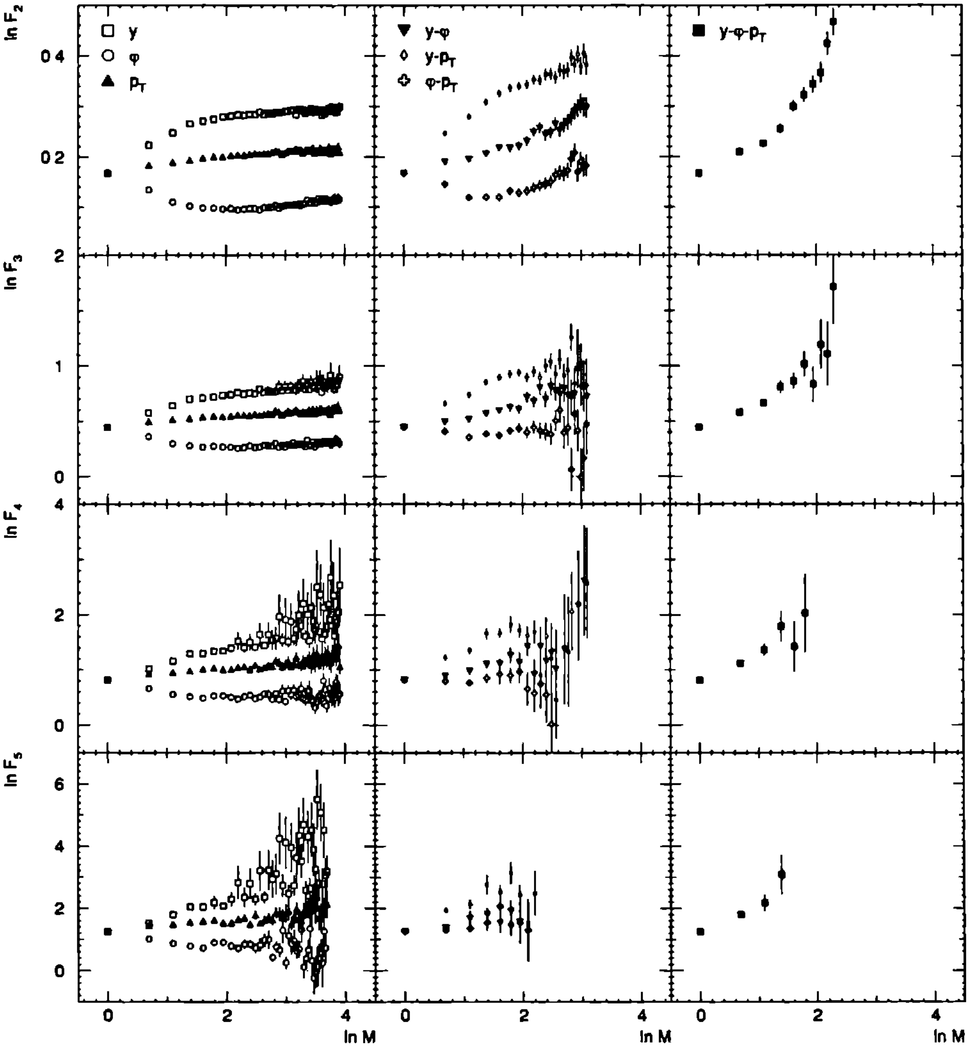

Figure 4.2: *Comparison of F_q for different variables and dimensions, as indicated in the uppermost subfigures.*

	ϕ_2	ϕ_3	ϕ_4	ϕ_5
y	0.009 ± 0.002	0.051 ± 0.007	0.19 ± 0.03	0.55 ± 0.07
φ	0.007 ± 0.002	0.014 ± 0.005	0.00 ± 0.02	-0.08 ± 0.04
p_T	0.008 ± 0.002	0.029 ± 0.005	0.08 ± 0.02	0.15 ± 0.04
y-φ	0.025 ± 0.004	0.09 ± 0.02	–	–
y-p_T	0.022 ± 0.003	0.05 ± 0.02	–	–
φ-p_T	0.025 ± 0.004	0.03 ± 0.02	–	–
y-φ-p_T	0.031 ± 0.002	0.077 ± 0.006	0.16 ± 0.02	0.28 ± 0.04

Table 4.1: *The intermittency indices ϕ_q for different combinations of the variables y, φ and p_T.*

$\phi_q(y\text{-}\varphi\text{-}p_T)$. However, one should notice that the parameter $\Phi_q = d\phi_q$ and, consequently, the anomalous dimension d_q are, for all orders, the largest for the three-dimensional phase space. I.e. the deviation from the topological dimension d is the largest for three-dimensions.

FRITIOF2.0 without BE-correlations (and with slightly different parameter setting), has been used to correct for possible biases in F_2 and F_3 due to Dalitz decay and γ-conversions [FBTH92]. The corrected values of F_2 and F_3 are smaller than the uncorrected ones, though the upward curvature of $\ln F_q$ vs. $\ln M$ remains. The ratio α_q/α_2 remains approximately the same. The uncertainties in FRITIOF2.0 were considered to be too large to repeat the procedure for orders $q \geq 4$. In Sect. 5.2.2.3 the problem of biases will be reconsidered.

The multidimensional factorial moments as predicted by FRITIOF2.0 without and with BE-correlations are compiled in figs. 4.3 and 4.4, respectively. Comparing Fig. 4.3 and Fig. 4.2 yields following remarks (the y-axes are shifted w.r.t. each other, but have the same scale in both figs.).

- The increase of the factorial moments in y is strongly underestimated. They are predicted to take values very close to the factorial moments in p_T. The moments in p_T themselves correspond rather well to the experimental values.
- The initial decrease of the F_q in φ observed in the experimental data can also be seen in the FRITIOF predictions.
- The FRITIOF predictions for the two-dimensional F_q in φ-p_T and y-φ almost coincide and decrease. The higher the order, the smaller this decrease and for $q = 4, 5$ $F_q(\varphi\text{-}p_T)$ even tends to increase at large M (small box sizes).
- The three-dimensional FRITIOF calculations result in a fast decreasing F_2 and a slower decreasing F_3. The F_4 and F_5, on the other hand, increase with decreasing phase space domains.

There seems to be a mechanism present in FRITIOF causing the moments to rise, most evident for higher-dimensional analysis and higher orders.

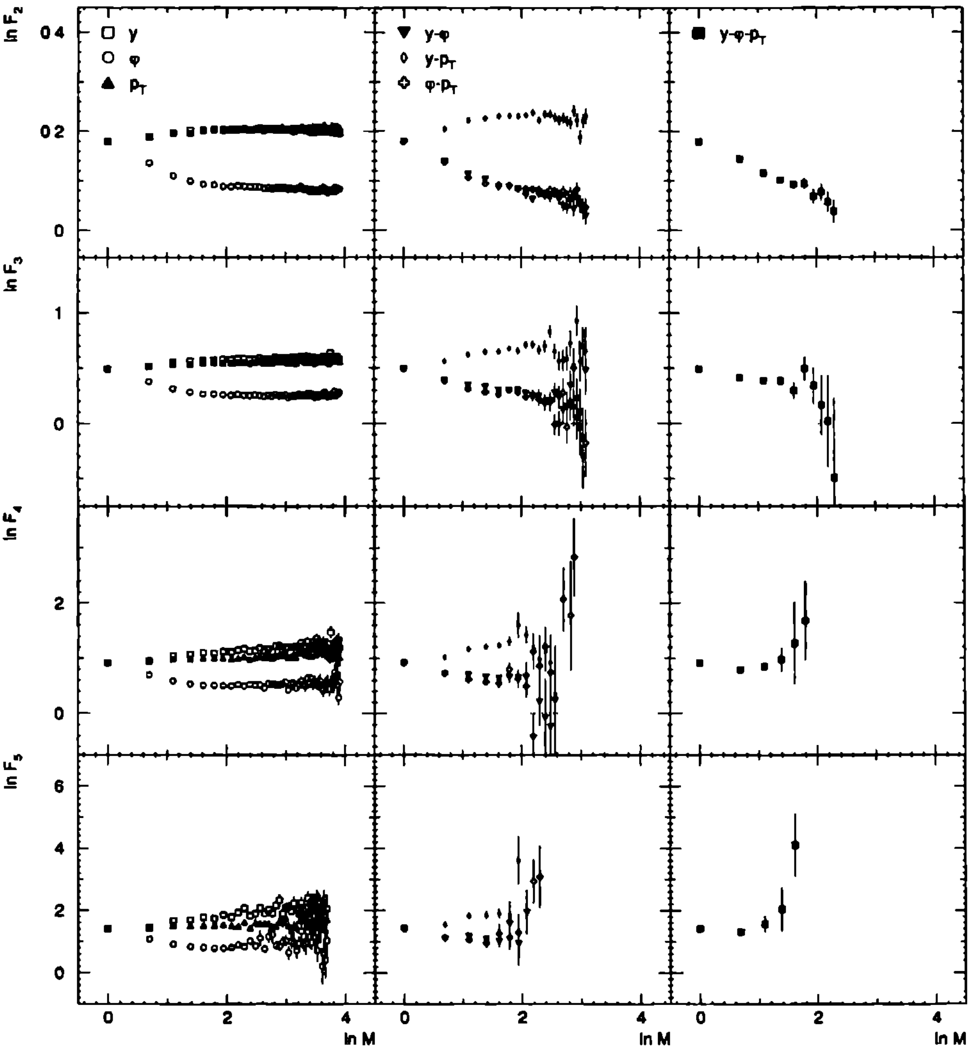

Figure 4.3: *Same as Fig. 4.2 for FRITIOF2.0 plain.*

When BE-correlations are introduced (Fig. 4.3), an increase of the moments is already visible for the one-dimensional $F_q(\varphi)$ and $F_q(p_T)$. While the second-order two- and three-dimensional factorial moments are still underestimated, the increase for the higher orders is overestimated by such a large amount that they could not be plotted on the same scale as the experimental factorial moments.

The overestimation of higher orders can be expected since the algorithm used to incorporate BE-correlations in FRITIOF only considers pairwise interactions [SJOCPC].

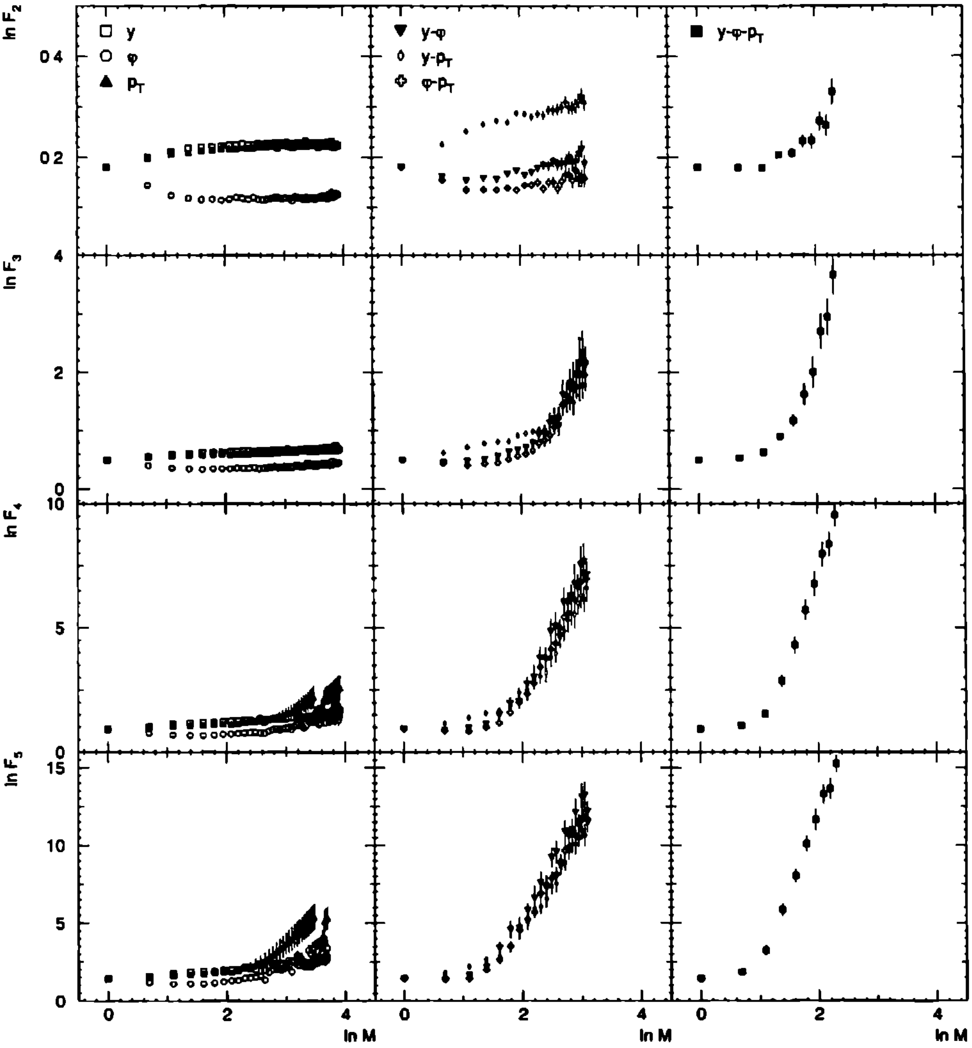

Figure 4.4: *Same as Fig. 4.2 for FRITIOF2.0 + Bose-Einstein correlations.*

An easy way of testing the modified power-law hypothesis (4.11) of Ochs and Wosiek consists in plotting $\ln F_q$ as a function of $\ln F_2$, the so-called Ochs-Wosiek plot. If all available data points are plotted, one is left with a rather messy picture. In [WOCH91], the author only shows $F_q(\delta)$ for δ-regions in which $F_2(\delta)$ varies significantly. Therefore, in Fig. 4.5 the moments are only given for $M = 1, \ldots, 10$. Except for φ-p_T, the data follow straight lines.

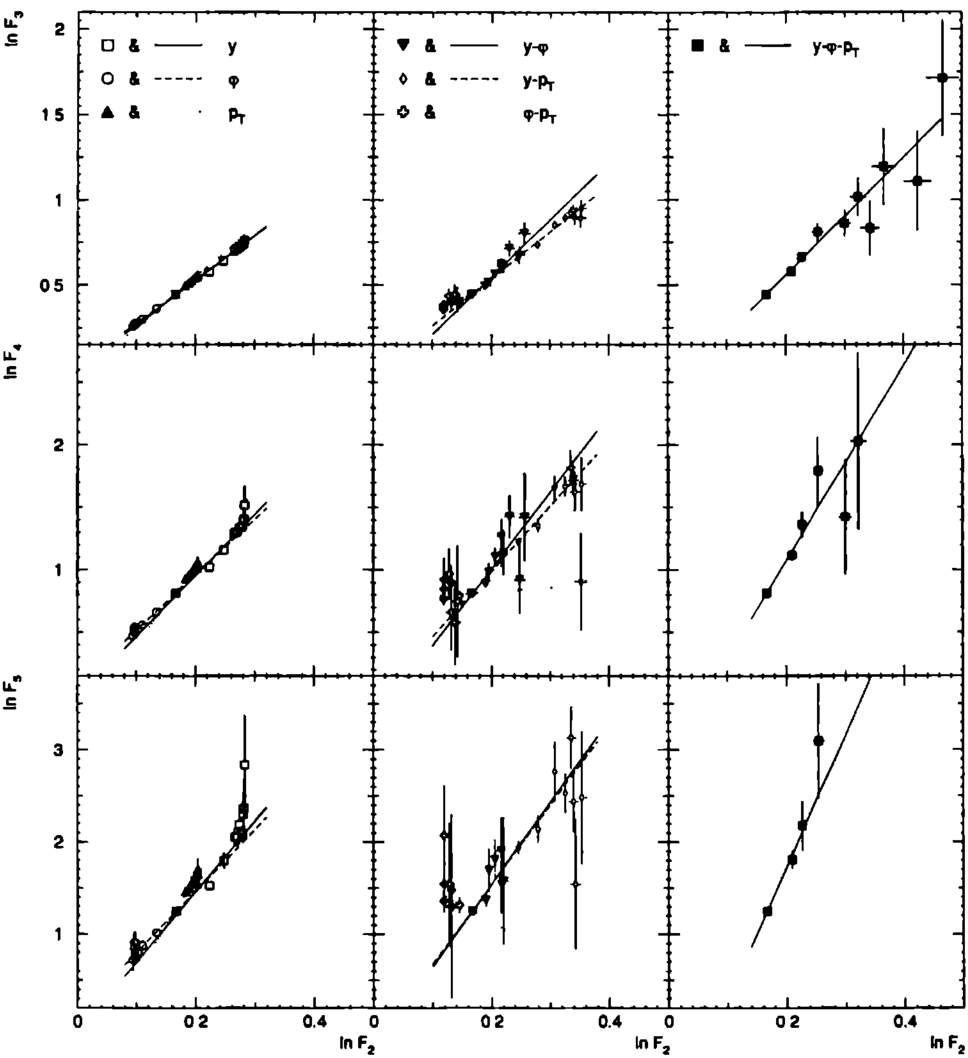

Figure 4.5: *The multidimensional factorial moments on a so-called Ochs-Wosiek plot.*

In order to extract the ratio α_q/α_2, a fit according to (4.12) has been applied to the data. The results are summarized in Tab. 4.2. On Fig. 4.5, they are represented by different line types as indicated on the figures. To make the difference in slopes (α_q/α_2) clearly visible, these straight lines are drawn over a larger region than the interval in which the fit was performed. Although the differences in α_q/α_2 are not that large (except for φ-p_T), one should not fit all variable combinations at the same time, as is suggested in [WOCH91].

	y	φ	p_T	y-φ	y-p_T	φ-p_T	y-φ-p_T
α_3/α_2	2.63 ± 0.09	2.6 ± 0.1	3.0 ± 0.3	3.4 ± 0.2	2.75 ± 0.07	1.6 ± 0.3	3.4 ± 0.2
α_4/α_2	4.9 ± 0.2	4.5 ± 0.2	6.2 ± 0.4	6.1 ± 0.6	5.2 ± 0.2	0.3 ± 0.5	7.8 ± 0.5
α_5/α_2	7.7 ± 0.3	6.7 ± 0.4	10.4 ± 0.7	8.9 ± 1.3	8.6 ± 0.3	-4 ± 1	14 ± 1
μ	1.54 ± 0.05	1.30 ± 0.08	2.07 ± 0.09	2.0 ± 0.1	1.75 ± 0.05	–	2.53 ± 0.08
χ^2/NDF	0.25/2	0.12/2	0.054/2	3.1/2	0.85/2	–	0.05/2
ν	1.45 ± 0.02	1.36 ± 0.03	1.67 ± 0.04	1.66 ± 0.05	1.51 ± 0.02	–	1.87 ± 0.04
χ^2/NDF	1.8/2	0.018/2	0.67/2	1.4/2	4.1/2	–	2.1/2

Table 4.2: *The ratios α_q/α_2 of from. (4.12) and the fit results obtained from (4.15) and (4.16).*

The difference between the different phase spaces becomes more striking when applying the fits proposed by Brax and Peschanski (4.15) [PBRP91] and by Hwa and Nazirov (4.16) [RHTN92]. The results of both fits can be found in Tab. 4.2. The χ^2 are displayed to allow a comparison of the fit quality obtained with the two different prescriptions. The aberrant behavior of φ-p_T leads to very large χ^2. Therefore, these fit results are not included in Tab. 4.2. For the one-dimensional p_T phase space and for the three-dimensional phase space (4.15) yields to values of $\mu > 2$, i.e. values not allowed in the Lévy stable law context. Non of the μ-values obtained are in accordance with a second-order phase transition. Fitting (4.16) also leads to an exclusion of a second-order phase transition to be responsible for the intermittency effect: all values of ν are larger than 1.304. Considering the χ^2-values, the Brax and Peschanski fit is slightly preferable over the Hwa and Nazirov fit, though both fits achieve acceptable χ^2-values.

Since the one-dimensional normalized factorial moments suffer from the projection effect, it is possible that also the BE-effect is distorted by this projection. Therefore, the F_q ($q = 2, 3$) of the all-charged sample are compared with those of the positively- and negatively-charged samples (Fig. 4.6). For $q = 2$ the moment for $(+-)$ combinations is added. Conform (3.43), $F_2(+-)$ (for d-dimensions) is given by

$$F_2^{(+-)}(\delta) = \frac{1}{M^d} \sum_{m=1}^{M^d} \frac{\int_{\Omega_m^q} \rho_2(\vec{x}^{(-)}, \vec{x}^{(+)}) d\vec{x}^{(-)} d\vec{x}^{(+)}}{\int_{\Omega_m} \rho_1(\vec{x}^{(-)}) d\vec{x}^{(-)} \int_{\Omega_m} \rho_1(\vec{x}^{(+)}) d\vec{x}^{(+)}} \tag{4.17}$$

$$= \frac{1}{M^d} \sum_{m=1}^{M^d} \frac{\left\langle n_m^{(-)} n_m^{(+)} \right\rangle}{\left\langle n_m^{(-)} \right\rangle \left\langle n_m^{(+)} \right\rangle} \; . \tag{4.18}$$

Unfortunately, the large errors on Fig. 4.6 make it very difficult to draw conclusions about the importance of BE-correlations in the intermittency effect. New tools are needed to extract this information. They exist under the form of density integrals to be discussed in (Sect. 5).

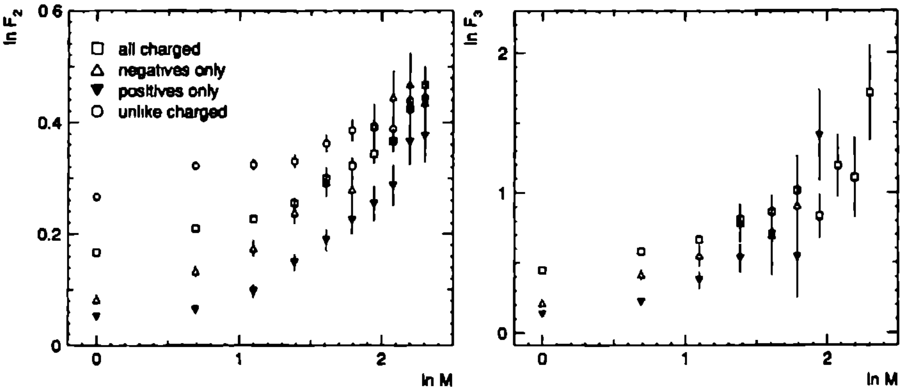

Figure 4.6: *Comparison of F_2 and F_3 for different charge combinations.*

4.3 Factorial cumulant moments

4.3.1 Formalism

For the determination of the multidimensional normalized factorial cumulant moments, the initial d-dimensional interval Δ is divided into d-dimensional boxes in the same way as for the calculation of the multidimensional normalized factorial moments. The generalization of (3.52) to higher dimensions is given by

$$K_q(\delta) = \frac{1}{M^d} \sum_{m=1}^{M^d} \frac{k_q^{(m)}}{\langle n_m \rangle^q} \quad , \tag{4.19}$$

where $k_q^{(m)}$ can be determined from the unnormalized factorial moments $\left\langle n_m^{[q]} \right\rangle$ by the use of (3.48).

Already for the one-dimensional analysis, the idea existed that one should investigate the scaling properties of the $K_q(\delta)$ rather than those of the $F_q(\delta)$ [HETH91, PCPL91]. Since neither of the multidimensional $F_q(\delta)$ exhibit a power law in δ, it is interesting to search for a power-law behavior of the multidimensional $K_q(\delta)$

$$K_q(\delta) = a_q \delta^{-\psi_q} = a_q \delta_l^{-\Psi_q} \quad . \tag{4.20}$$

To allow for a possible deviation from a simple power law, Fiałkowski [KFIA91, KFIA92a] suggested to add a constant c for $q = 2$, i.e. to fit

$$K_2(\delta) = a\delta^{-b} + c \quad , \tag{4.21}$$

where c takes into account possible non-singular long-range correlations. In [KFIA92b] the author stresses the importance of including bin-size correlations when fitting (4.21).

4.3.2 Experimental results

The $\ln K_q$ are plotted as a function of $\ln M$ in Fig. 4.7, for the analysis in the various variables and dimensions. As in the case of the one-dimensional analysis, the $K_q(\delta)$ are only considered for bin sizes where $F_{q+1}(\delta)$ is non-zero and the relative error on F_q is smaller than 50%.

In one-dimensional rapidity space, the data (open squares in Fig. 4.7a and d) show the presence of genuine higher-order multiparticle correlations in rapidity. K_4 still has the same trend of an increase with decreasing bin size, but is not shown here because of large errors. K_5 is consistent with zero (not shown). The same analysis applied to the variable φ (open circles in Fig. 4.7a) does not show evidence for correlations of order higher than two. In p_T (triangles in Fig. 4.7a) an increase is observed for K_2 and K_3, but the results are not shown for K_3 due to too large errors. Also here, K_4 and K_5 are consistent with zero.

For the three possible two-dimensional combinations of y, φ and p_T (Fig. 4.7b) an increase is observed for $q = 2$ and $q = 3$, K_3 is not shown because of the large errors. The higher orders are consistent with zero.

In three dimensions (Fig. 4.7c and e), the existence of $K_q > 0$ up to order three suggests the presence of three-dimensional genuine higher order multiparticle correlations. K_4 still

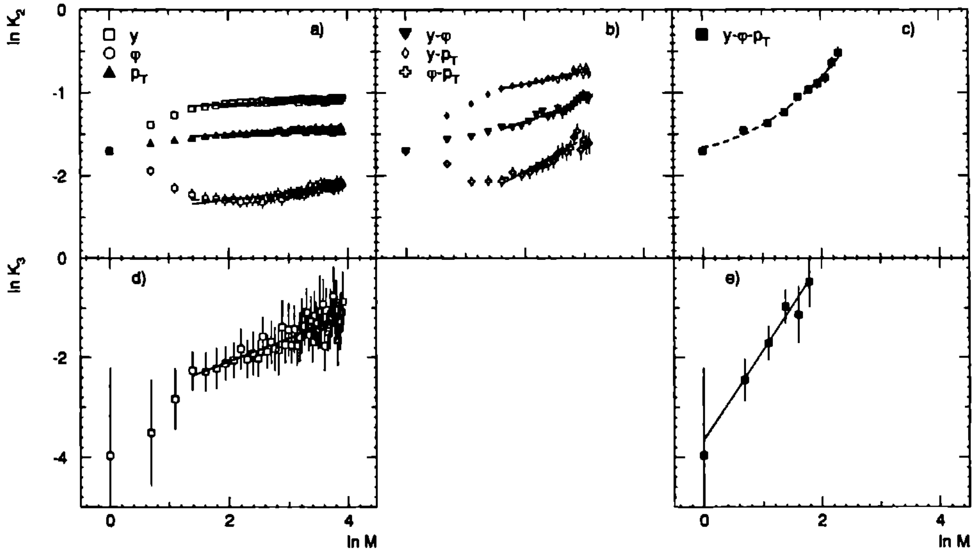

Figure 4.7: *Comparison of K_2 and K_3 for different variables and dimensions, as indicated in the uppermost subfigures. Full lines correspond to a fit by (4.20), dashed lines to a fit by (4.21).*

has the same trend of an increase with decreasing bin size, but is dropped from the figure since the errors are very large. For $q \geq 5$, K_q is equal to zero within errors.

Fits according to (4.20) have been applied to the data and are represented in Fig. 4.7 by full lines. The fit parameters are collected in Tab. 4.3, together with χ^2/NDF and the range of the fit in the number of linear divisions M. Except for K_2 in the three dimensions, the fit quality is good. The three dimensional K_2, however, shows a clear upward bending and, compared to the behavior of the three-dimensional F_2, there is very little improvement in the direction of linearity.

order		y	φ	p_T
2	a_2	0.299 ± 0.002	0.086 ± 0.001	0.205 ± 0.002
	ψ_2	0.036 ± 0.002	0.081 ± 0.004	0.042 ± 0.002
	χ^2/NDF	8.1/35	10/35	4.4/35
	range M	$4-40$	$4-40$	$4-40$
3	a_3	0.049 ± 0.003		0.036 ± 0.003
	ψ_3	0.47 ± 0.02		0.30 ± 0.03
	χ^2/NDF	5.9/35		3.7/35
	range M	$4-40$		$4-40$
4	a_4	0.014 ± 0.003		
	ψ_4	1.46 ± 0.07		
	χ^2/NDF	8.9/28		
	range M	$4-33$		

order		y-φ	y-p_T	φ-p_T	y-φ-p_T
2	a_2	0.162 ± 0.002	0.305 ± 0.003	0.065 ± 0.001	0.162 ± 0.003
	ψ_2	0.118 ± 0.002	0.073 ± 0.002	0.195 ± 0.005	0.161 ± 0.004
	χ^2/NDF	5.4/12	2.6/12	6.1/12	23/8
	range M	$5-18$	$5-18$	$5-18$	$1-10$
3	a_3	0.009 ± 0.002	0.18 ± 0.02	0.04 ± 0.01	0.026 ± 0.005
	ψ_3	0.74 ± 0.04	0.15 ± 0.03	0.24 ± 0.08	0.60 ± 0.05
	χ^2/NDF	2.7/7	2.6/7	0.7/5	0.8/4
	range M	$5-13$	$5-13$	$5-11$	$1-6$
4	a_4				0.006 ± 0.005
	ψ_4				1.3 ± 0.2
	χ^2/NDF				0.26/2
	range M				$1-4$

Table 4.3: *Fit results according to (4.20).*

The dashed lines in Fig. 4.7 represent fits according to (4.21), without taking into account the bin-size correlations. The fit parameters are given in Tab. 4.4. For the three-dimensional factorial cumulant moment, the addition of the constant in (4.21) improves the fit quality. The value $c = 0.16 \pm 0.02$ found here is compatible with an old model [ACAK78] and a more recent estimate [ACFK89]. The value b turns out to be rather independent of the process considered, suggesting universality in the bin-size dependence of the second-order factorial cumulant moment. Collective correlations seem to be the basis of the power-law term in (4.21) [KFIA91, KFIA92a, KFIA92b]. Since for $q > 2$ the $\ln K_q$ show good linear behavior on $\ln M$, an analogous fit (4.21) to higher orders gives values of c compatible with zero.

	a	b	c	χ^2/NDF	range
y	1.58 ± 0.02	0.07 ± 0.01	-1.30 ± 0.02	8.1/34	4 – 40
φ	$(0.2 \pm 1.1) \times 10^{-4}$	1.8 ± 1.3	0.101 ± 0.004	4.3/34	4 – 40
p_T	0.70 ± 0.02	0.013 ± 0.003	-0.49 ± 0.02	4.4/34	4 – 40
y-φ	0.02 ± 0.08	0.3 ± 0.5	0.2 ± 0.1	5.1/11	5 – 18
y-p_T	0.04 ± 0.24	0.2 ± 0.6	0.3 ± 0.3	2.4/11	5 – 18
φ-p_T	$(0.1 \pm 0.6) \times 10^{-3}$	1.1 ± 0.7	0.13 ± 0.02	1.8/11	5 – 18
y-φ-p_T	0.03 ± 0.01	0.39 ± 0.06	0.16 ± 0.02	5.9/7	1 – 10
+ cov. mat.	0.05 ± 0.01	0.30 ± 0.04	0.13 ± 0.01	25/7	1 – 10
y-φ-p_T	0.012 ± 0.008	0.50 ± 0.09	0.20 ± 0.02	3.1/7	2 – 10
+ cov. mat.	0.011 ± 0.004	0.51 ± 0.06	0.20 ± 0.01	6.2/7	2 – 10

Table 4.4: *Fit results according to (4.21).*

To get a feeling of the influence of bin-size correlations on the fit results, the Fiałkowski fit (4.21) has been repeated for the three-dimensional factorial cumulants with use of the proper covariance matrix (Tab. 4.4). This reduces the constant term to $c = 0.13 \pm 0.01$.

In Fig. 4.8a, $\ln(K_2 - c)$ is shown as a function of $\ln M$. Here, c is obtained from the Fiałkowski fit in the range $M = 1-10$, with including the bin-size correlations. If relationship (4.21) holds, the data are on a straight line. The fit itself is represented on Fig. 4.8a by the dashed line. The full line corresponds to the fit result one obtains when neglecting the bin-size correlations. While the dashed line is straight, the full line is curved due to the difference in the constant term c. Both fits give a visually satisfying result. On the contrary, for the one-dimensional rapidity F_q the use of the covariance matrix in the fit procedure yielded fits appearing optically wrong: the curves run below most of the data points [FBTH92].

A closer look at Fig. 4.8a learns that the data points are not exactly on a straight line. Furthermore, it seems as if for the data point at $M = 1$ other mechanisms are involved, it is lower than one expects from an extrapolation of the other nine points. Therefore, in Fig. 4.8b, the $M = 1$ point has been dropped and fits with and without use of the covariance matrix are performed. As already can be expected from the resulting parameters (Tab. 4.4), the fits become undistinguishable. The influence of the bin-size correlations has been reduced by dropping the first data point in the fit procedure. The constant term c is now increased to $c = 0.20 \pm 0.02$.

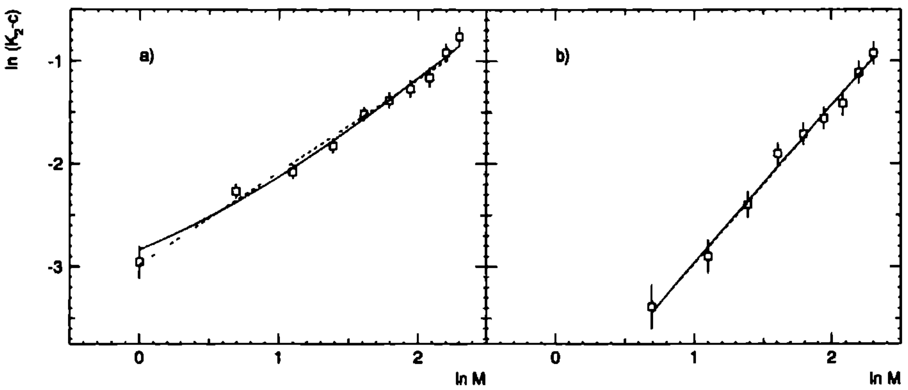

Figure 4.8: *Illustration of fitting (4.21) with (dashed lines) and without (full lines) taking into account the bin-size correlations. The c in the label on the y-axis refers to the value of c obtained when the covariance matrix is used in the fit procedure. The fits are applied in the range $M = 1 - 10$ and $M = 2 - 10$ for a) and b), respectively.*

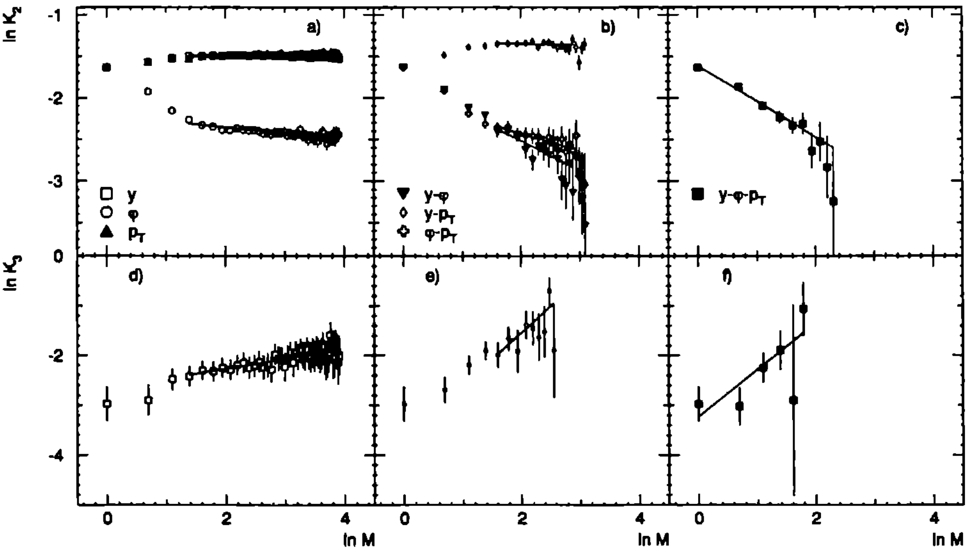

Figure 4.9: *Multidimensional factorial cumulants predicted by FRITIOF2.0 plain. The full lines represent a fit according to (4.20).*

As can be seen from Fig. 4.9 and Tab. 4.5, FRITIOF2.0 plain predicts all second-order cumulant moments, except for p_T, to decrease with decreasing bin size in the region where the fit (4.20) (full lines on Fig. 4.9) has been applied. This behavior is the opposite of what is observed experimentally. Except for $\varphi - p_T$, genuine third-order correlations are predicted to exist and to increase with decreasing bin size for all multidimensional phase spaces (for clarity of the picture, only $K_3(y)$, $K_3(y - p_T)$ and $K_3(y - \varphi - p_T)$ are shown on Fig. 4.9). The $K_3(\varphi - p_T)$ are equal to zero within errors. However, the error on $\psi_3(y - \varphi)$ is so large that the slope could be considered compatible with zero. Experimentally, K_3 is found to be zero only for the one-dimensional azimuthal-angle phase space and none of the fitted slopes turns out to be compatible with zero. Fourth-order factorial cumulant moments in y exist and increase with decreasing δ (not shown). For the other dimensions K_4 is predicted to be zero. Experimentally, however, also the three-dimensional fourth-order factorial cumulant moments turn out to be non-zero and increasing with decreasing bin size. Multiparticle correlations of order $q \geq 5$ are predicted to be compatible with zero for

order		y	φ	p_T	
2	a_2	0.227 ± 0.001	0.110 ± 0.001	0.217 ± 0.001	
	ψ_2	-0.004 ± 0.002	-0.072 ± 0.003	0.019 ± 0.001	
	χ^2/NDF	4.1/35	6.5/35	6.5/35	
	range M	$4 - 40$	$4 - 40$	$4 - 40$	
3	a_3	0.069 ± 0.003	0.0050 ± 0.0008	0.040 ± 0.003	
	ψ_3	0.20 ± 0.01	0.60 ± 0.05	0.21 ± 0.02	
	χ^2/NDF	3.1/35	3.7/35	7.4/35	
	range M	$4 - 40$	$4 - 40$	$4 - 40$	
4	a_4	0.014 ± 0.002			
	ψ_4	1.01 ± 0.05			
	χ^2/NDF	8.9/35			
	range M	$4 - 40$			

order		y-φ	y-p_T	φ-p_T	y-φ-p_T
2	a_2	0.164 ± 0.005	0.266 ± 0.003	0.134 ± 0.037	0.200 ± 0.004
	ψ_2	-0.177 ± 0.007	-0.006 ± 0.002	-0.105 ± 0.007	-0.143 ± 0.007
	χ^2/NDF	8.3/12	5.5/12	1.9/12	5.4/8
	range M	$5 - 18$	$5 - 18$	$5 - 18$	$1 - 10$
3	a_3	0.07 ± 0.01	0.025 ± 0.003		0.04 ± 0.007
	ψ_3	0.05 ± 0.06	0.54 ± 0.03		0.32 ± 0.05
	χ^2/NDF	0.30/6	4.7/7		3.1/4
	range M	$5 - 13$	$5 - 13$		$1 - 6$

Table 4.5: *Fit results according to (4.20) obtained for FRITIOF2.0 plain.*

whatever multidimensional phase space, consistent with experimental observations.

As could be expected from Fig. 4.4, the inclusion of Bose-Einstein correlations in FRITIOF2.0 yields an overestimation of the two- and three-dimensional genuine multiparticle correlations of order $q > 2$ (Fig. 4.10). The genuine higher-order correlations in the one-dimensional p_T and φ phase spaces are overestimated as well.

Fig. 4.10 and Tab. 4.6 show that one-dimensional genuine higher-order correlations are now predicted to exist and increase with decreasing bin size, up to order $q = 5$. Unfortunately, the relative error on $F_5(p_T)$ becomes larger than 50% for $M \geq 15$. Consequently, the determination of $K_5(p_T)$ for sufficiently small bin sizes needed for a meaningful fit, is not possible. Further investigation reveals that only a few events contribute to the strong increase of the fifth-order normalized factorial moments in p_T, decreasing from 286 events out of 110000 at $M = 15$ to 23 events at $M = 40$.

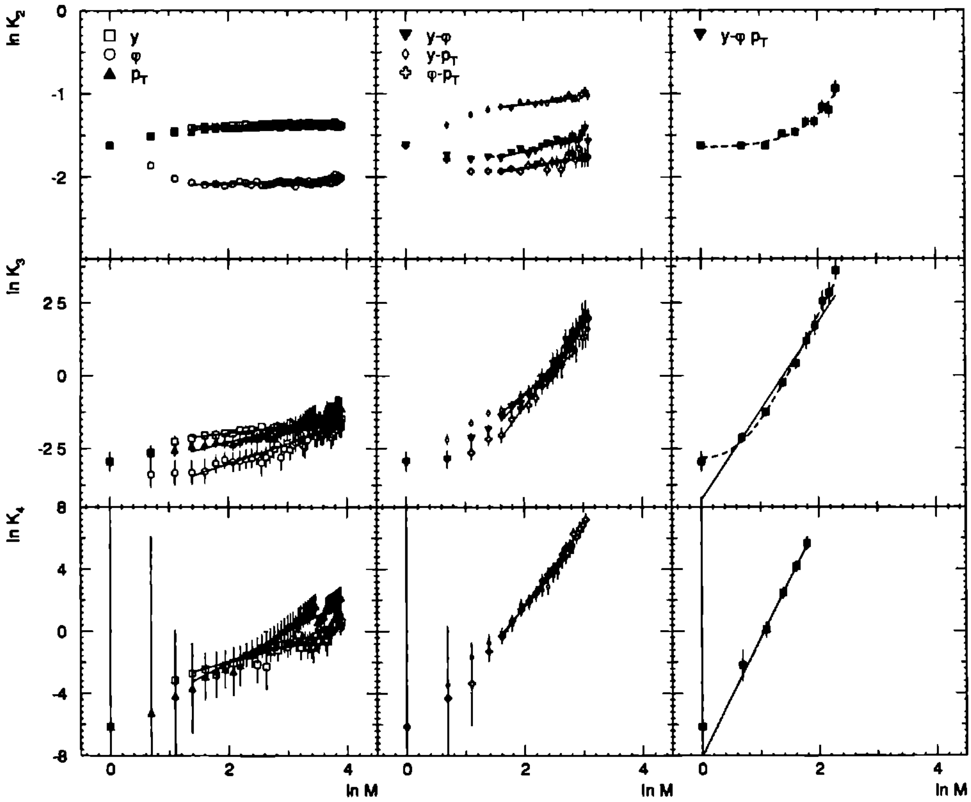

Figure 4.10: *Multidimensional factorial cumulants predicted by FRITIOF2.0 + BE. The full lines and dashed lines represent fits according to (4.20) and (4.21), respectively.*

order		y	φ	p_T
2	a_2	0.242 ± 0.001	0.121 ± 0.001	0.230 ± 0.001
	ψ_2	0.016 ± 0.001	0.125 ± 0.003	0.026 ± 0.002
	χ^2/NDF	6.5/35	5.6/35	5.3/35
	range M	4 – 40	4 – 40	4 – 40
3	a_3	0.089 ± 0.003	0.0123 ± 0.0008	0.036 ± 0.002
	ψ_3	0.22 ± 0.01	0.69 ± 0.02	0.52 ± 0.02
	χ^2/NDF	6.2/35	8.1/35	8.7/35
	range M	4 – 40	4 – 40	4 – 40
4	a_4	0.017 ± 0.002	0.0017 ± 0.0002	0.0230 ± 0.0003
	ψ_4	1.06 ± 0.04	1.86 ± 0.03	2.03 ± 0.04
	χ^2/NDF	4.6/37	7.2/35	10/35
	range M	4 – 40	4 – 40	4 – 40
5	a_4	0.06 ± 0.02	0.0008 ± 0.0002	
	ψ_4	1.17 ± 0.09	1.27 ± 0.07	
	χ^2/NDF	3.2/32	3.9/24	
	range M	4 – 40	4 – 29	

order		y-φ	y-p_T	φ-p_T	y-φ-p_T
2	a_2	0.129 ± 0.002	0.268 ± 0.002	0.117 ± 0.002	0.180 ± 0.002
	ψ_2	0.089 ± 0.003	0.047 ± 0.002	0.064 ± 0.004	0.062 ± 0.004
	χ^2/NDF	3.9/12	5.7/12	4.9/12	48/8
	range M	5 – 18	5 – 18	5 – 18	1 – 10
3	a_3	0.0066 ± 0.0004	0.019 ± 0.001	0.0015 ± 0.0001	0.014 ± 0.001
	ψ_3	1.08 ± 0.02	0.83 ± 0.01	1.36 ± 0.02	0.32 ± 0.05
	χ^2/NDF	5.7/12	4.1/12	4.5/12	31/8
	range M	5 – 18	5 – 18	5 – 18	1 – 10
4	a_3		$(6.6 \pm 0.8) \times 10^{-4}$	$(1.7 \pm 0.2) \times 10^{-4}$	$(3.1 \pm 0.6) \times 10^{-4}$
	ψ_3		2.22 ± 0.03	2.57 ± 0.02	2.54 ± 0.05
	χ^2/NDF		3.2/11	1.9/12	0.52/4
	range M		5 – 17	5 – 18	1 – 6

Table 4.6: *Fit results according to (4.20) obtained for FRITIOF2.0 + BE.*

When more than one dimension is involved, the factorial cumulants can be determined up to $q = 4$. An increase with decreasing δ is observed for all cases. Nevertheless, for the $y - \varphi$ analysis, too few points are available in the fit region and no fit has been performed.

The three-dimensional K_2 and K_3 are both predicted to curve upward, while for the NA22 data only K_2 exhibits this behavior. For FRITIOF2.0 + BE a fit according to (4.21) has been applied (dashed lines on Fig. 4.10) to both K_2 and K_3. The fit results are given in

Tab. 4.7. It is clear that both K_2 and K_3 benefit from the constant c added. The predicted value of c (second order) is slightly larger than experimentally observed.

	a	b	c	χ^2/NDF	range
y-φ-p_T $(q=2)$	0.001 ± 0.001	0.7 ± 0.1	0.192 ± 0.005	6.9/7	$1-10$
y-φ-p_T $(q=3)$	0.003 ± 0.001	1.3 ± 0.1	0.06 ± 0.02	2.2/7	$1-10$

Table 4.7: *Fit results according to (4.21) obtained for FRITIOF2.0 + BE.*

4.4 Factorial correlators

4.4.1 Formalism

While the generalization of the one-dimensional normalized factorial moments and factorial cumulant moments to the multidimensional analysis is rather straightforward, it is not that obvious to define multidimensional factorial correlators. The big issue is the definition of the distance between two d-dimensional boxes. Consider the two-dimensional case in Fig. 4.11a. Is, for example, the distance between bin 1, 1 and bin 1, 2 the same as the distance between 1, 1 and 2, 2? And in what "units" should one express this distance? Once this problem of distance definition is solved, the factorial correlators can be averaged over constant bin- (or box-) distances and symmetrized w.r.t. the order qq', as in the one-dimensional case.

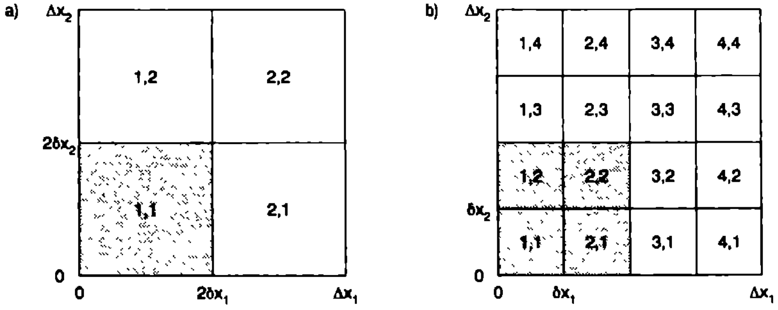

Figure 4.11: *Illustration of a two dimensional binning in $\Delta = \Delta x_1 \Delta x_2$. The linear size δ_l of the bins in a) is twice δ_l of the bins in b).*

A suggestion for a good definition of distance measure is obtained by extending the relation between the one-dimensional normalized factorial moments and factorial correlators (sec. 3.3.1.3),

$$F_{11}(D) = 2F_2(2D) - F_2(D) \quad , \tag{4.22}$$

to two dimensions.

Consider the initial interval $\Delta = \Delta x_1 \Delta x_2$ and divide it into L^2 bins of size $4\delta = 2\delta x_1 2\delta x_2$, as shown in Fig. 4.11a. In Fig. 4.11b, the initial interval is divided into $M^2 = (2L)^2$ bins of size $\delta = \delta x_1 \delta x_2$. For the occasion, the numbering of the bins occurs in a different way than for the factorial moments and cumulant moments: Each bin is given a number l_1, l_2 with $l_1 = 1, \ldots, L$ and $l_2 = 1, \ldots, L$ in Fig. 4.11a and analogously in Fig. 4.11b.

The relation between the two-dimensional normalized factorial moments and factorial correlators can now be derived as follows. From Fig. 4.11 it is clear that

$$\begin{aligned}
\left\langle n^{[2]}_{l_1,l_2} \right\rangle &= \left\langle (n_{m_1,m_2} + n_{m_1+1,m_2} + n_{m_1,m_2+1} + n_{m_1+1,m_2+1})^{[2]} \right\rangle \\
&= \left\langle n^{[2]}_{m_1,m_2} \right\rangle + \left\langle n^{[2]}_{m_1+1,m_2} \right\rangle + \left\langle n^{[2]}_{m_1,m_2+1} \right\rangle + \left\langle n^{[2]}_{m_1+1,m_2+1} \right\rangle + 2\left\langle n_{m_1,m_2} n_{m_1+1,m_2} \right\rangle \\
&\quad +2\left\langle n_{m_1,m_2} n_{m_1,m_2+1} \right\rangle + 2\left\langle n_{m_1,m_2} n_{m_1+1,m_2+1} \right\rangle + 2\left\langle n_{m_1+1,m_2} n_{m_1,m_2+1} \right\rangle \\
&\quad +2\left\langle n_{m_1+1,m_2} n_{m_1+1,m_2+1} \right\rangle + 2\left\langle n_{m_1,m_2+1} n_{m_1+1,m_2+1} \right\rangle \qquad (4.23)
\end{aligned}$$

$$\text{with} \qquad m_1 = 2l_1 - 1 \qquad \text{and} \qquad m_2 = 2l_2 - 1 \quad ,$$

where the second step is obtained by applying the generalized multinomial theorem. Dividing (4.23) by $\langle n_{m_1,m_2} n_{m_1,m_2+1} \rangle$, assuming translation invariance of the density distribution and averaging over the bins, yields

$$16F_2(2\delta x_1 2\delta x_2) = 4F_2(\delta x_1 \delta x_2) + 12F_{11}(D = \delta x_1 \delta x_2, \delta = \delta x_1 \delta x_2) \quad . \qquad (4.24)$$

If, as for the one-dimensional case, the F_{11} is bin-size independent, (4.24) becomes, after substitution of $\delta x_1 = \delta x_2 = D_l$,

$$F_{11}\left(D_l^2\right) = \frac{4}{3}F_2\left((2D_l)^2\right) - \frac{1}{3}F_2\left(D_l^2\right) \quad . \qquad (4.25)$$

From this derivation, one understands the distance between two bins is expressed as an area and is the same between bins 1, 1 and 1, 2 as between bins 1, 1 and 2, 2. Generally, if the factorial correlators are calculated for two-dimensional bins of linear size δ_l, the bin distance $D = D_l^2$ between m_1, m_2 and m_3, m_4 is defined via the linear bin distance D_l by

$$D_l = \max(|m_1 - m_3|, |m_2 - m_4|)\,\delta_l \quad . \qquad (4.26)$$

The extension from two to three dimensions is now straightforward. If factorial correlators are determined for three-dimensional bins of linear size δ_l, the bin distance $D = D_l^3$ between m_1, m_2, m_3 and m_4, m_5, m_6 is given by

$$D_l = \max(|m_1 - m_4|, |m_2 - m_5|, |m_3 - m_6|)\,\delta_l \quad . \qquad (4.27)$$

The three dimensional analogue of (4.25) is found to be

$$F_{11}\left(D_l^3\right) = \frac{8}{7}F_2\left((2D_l)^3\right) - \frac{1}{7}F_2\left(D_l^3\right) \quad . \qquad (4.28)$$

In general, the sum rule for d-dimensional factorial moments and factorial cumulants can be expressed as

$$F_{11}\left(D_l^d\right) = \frac{2^d}{2^d - 1}F_2\left((2D_l)^d\right) - \frac{1}{2^d - 1}F_2\left(D_l^d\right) \quad , \qquad (4.29)$$

with D_l representing the linear bin *distance* on the left-hand side and the linear bin *size* on the right-hand side.

Before turning to the experimental results, a remark should be made about the variable φ. Before applying transformation (4.1) φ is a cyclic variable: Angles outside the interval $[0, 2\pi]$ can be brought inside the interval since $\varphi = \varphi \pm 2k\pi$. An angle between two objects, however, will always be contained in the interval $[0, \pi]$. If the angle $D\varphi = |\varphi_1 - \varphi_2|$ between two particles is found to be larger than π, it should, therefore, be replaced by $2\pi - D\varphi$. Since the density distribution in φ is almost flat, transformation (4.1) approximately acts as the linear transformation $X(\varphi) = \varphi/2\pi$. The distance $DX(\varphi)$ between two particles will now be smaller than or equal to 0.5, larger values have to be replaced by $1 - DX(\varphi)$.

In the following only transformed variables are used and are referred to by the name of the variable itself.

4.4.2 Experimental results

In Fig. 4.12, the $\ln F_{qq'}$ are plotted vs. $-\ln D_l$ (decreasing bin distance) for various dimensions and orders, according to the symbols in the uppermost subfigures. Factorial correlators obtained for different bin sizes are put together to form one curve. Usually, correlators determined for different bin sizes but for the same bin distance yield values the same within errors, proving the bin-size independence also holds approximately for higher dimensions. To maintain a reasonable number of bin pairs in the averaging over constant bin distance, the correlators are only determined for $D_l \leq 0.5$ ($-\ln D_l = 0.693$).

Fig. 4.12 shows that there are no strict power laws. Therefore, no fits have been performed. Although the three one-dimensional $\ln F_{11}$ behave very differently, they have parallel curves for $-\ln D_l \geq 2.5$. In this region the one-dimensional F_{11} are nearly independent of D_l. The curves of the two-dimensional $\ln F_{11}$ become parallel for $-\ln D_l \geq 2.3$, where they increase with decreasing bin-distance (increasing $-\ln D_l$). In three dimensions, $\ln F_{11}$ increases with increasing $-\ln D_l$ for $-\ln D_l \geq 1.4$, this increase is stronger than the one mentioned above for the two-dimensional case.

For higher orders, the same tendency can be seen. However, due to too low statistics, the correlators cannot be determined for small bin sizes, consequently, the number of points at small bin distances reduces. Even for large bin sizes, the higher-order factorial correlators exhibit large errors.

In Fig. 4.13, the factorial correlators of order $qq' = 11$ (circles) are compared with values obtained from the factorial moments via the sum rule (4.29) (triangles). As can be seen the agreement is good (especially for $-\ln D_l \geq 1.39$), but not exact. Reasons for differences between F_{11} and (4.29) are:

1. the bin-size independence of the correlators is only approximately true,
2. the cyclic character of φ is not taken into account for the determination of the factorial moments (it is not clear how one should incorporate this),
3. the two-dimensional and three-dimensional inclusive distributions are only approximately flat.

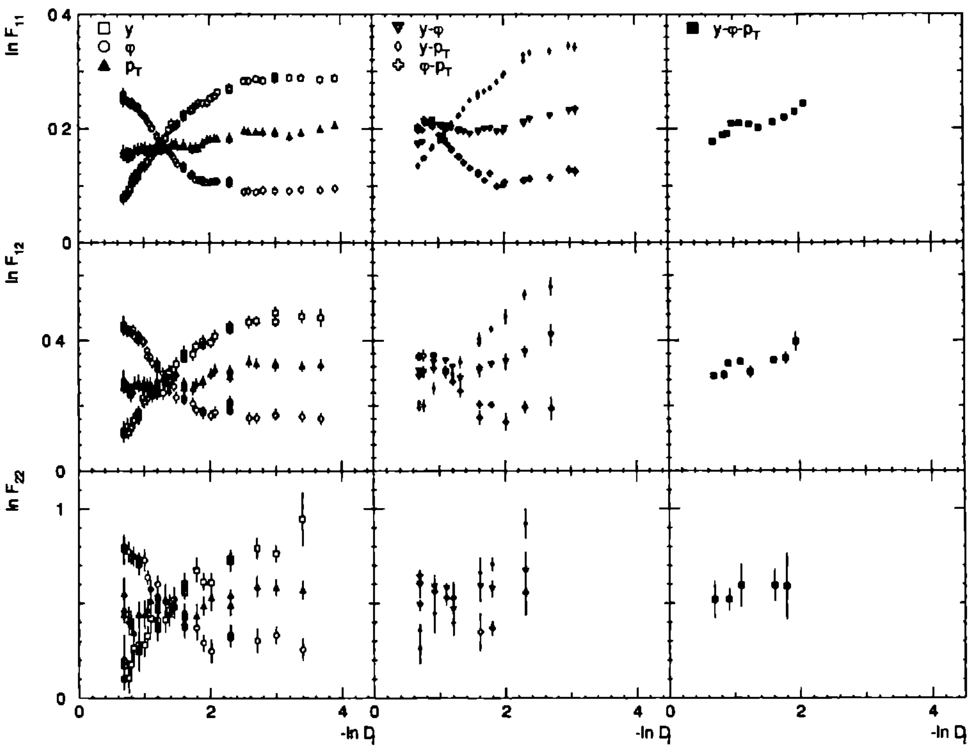

Figure 4.12: *Compilation of the multidimensional factorial correlators for orders* $qq' = 11, 12, 22$.

4.5 Conclusions

- The rise of the factorial moments with decreasing linear bin size is stronger when evaluated in three than in lower dimensions. They do not obey a strict power law for whatever combination of phase-space variables. The behavior of the factorial moments is not reproduced by FRITIOF2.0, neither without nor with inclusion of BE-correlations. Some mechanism in the model causes the higher-dimensional higher-order moments to rise. Taking into account the BE-correlations stresses the effect of the mechanism.

  Except for $\varphi - p_T$, the modified power-law hypothesis of Ochs and Wosiek is followed by the NA22 data in the region where $F_2(\delta)$ depends significantly on δ. For the one-dimensional p_T- and the three-dimensional phase space, the order dependence of the slopes α_q/α_2 on the Ochs-Wosiek plot yields values of μ larger than allowed in the Lévy stable law context. For all cases, the order dependence of α_q/α_2 excludes a second-order phase transition as a possible source of intermittency, both in the framework of the Lévy stable law and the Ginzburg-Landau description of phase transitions.

- Except for the one-dimensional φ phase space, the factorial cumulant moments show

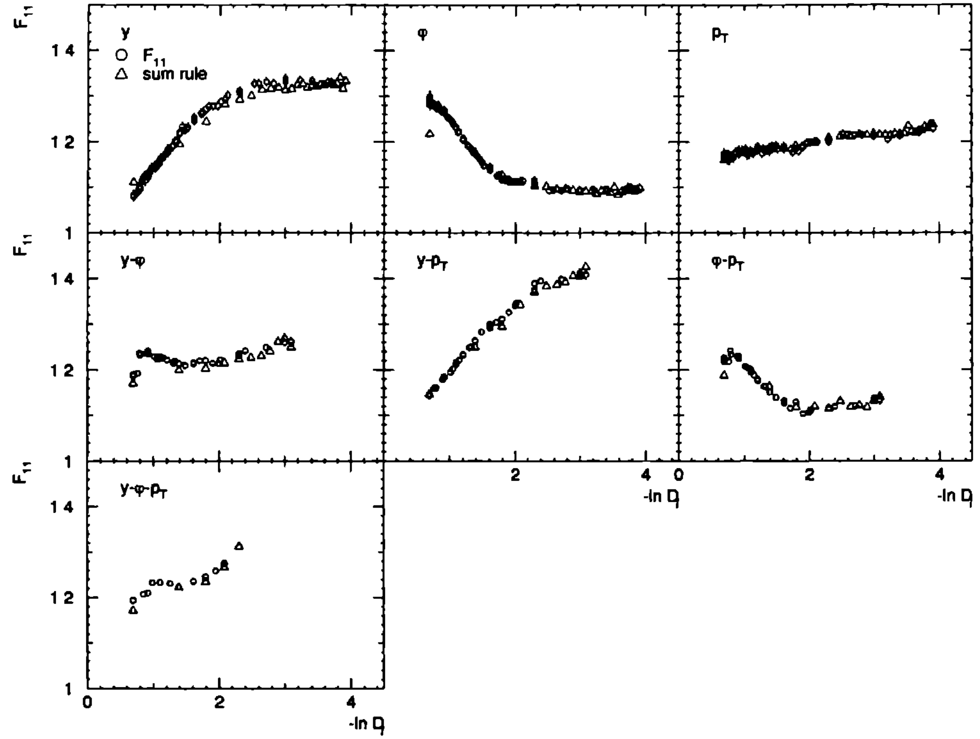

Figure 4.13: *Test of the generalized sum rule (4.29) for multidimensional factorial correlators.*

evidence for non-zero genuine multiparticle correlations. They increase according to a power law for orders $q > 2$. The three-dimensional second-order factorial cumulant moments show a clear upward bending. Adding a constant c to the power law, to take into account possible non-singular long-range correlations, improves the fit quality considerably. The constant c turns out to take the value $c = 0.16 \pm 0.02$, compatible with earlier independent estimates. If $K_2(\delta = 1)$ is excluded from the fit, the fit results are the same whether or not the bin-size correlations are taken into account. The constant c then increases to $c = 0.20 \pm 0.02$.

The FRITIOF model fails to reproduce the experimentally observed factorial cumulant moments, regardless the order or the variables used.

- The factorial correlators depend strongly on the phase-space variables used for the analysis. This makes comparison very difficult, though the increase of the correlators with decreasing bin distance seems strongest in three dimensions.

  As was the case in one dimension (Sect. 3.3), the sum rule between F_{11} and F_2 holds reasonably well for multidimensional factorial correlators.

Bibliography

[ABJS90] A. Białas and M. Gazdzicki, Phys. Lett. **B252** (1990) 483.

[ABMG90] A. Białas and J. Seixas, Phys. Lett. **B250** (1990) 161.

[ACAK78] A. Capella, A. Krzywicky, Phys. Rev. **D18** (1978) 4120.

[ACFK89] A. Capella, K. Fiałkowski, A. Krzywicky, Phys. Lett. **B230** (1989) 149.

[BPNP86] A. Białas and R. Peschanski, Nucl. Phys. **B273** (1986) 703.

[BPNP88] A. Białas and R. Peschanski, Nucl. Phys. **B308** (1988) 857.

[EDBE89] E. den Bekker, Diploma Thesis, Univ. of Nijmegen (1989).

[FBTH92] F. Botterweck, Ph.D. Thesis, Univ. of Nijmegen (1992).

[HETH91] H. Eggers, Ph.D. Thesis, Univ. of Arizona, (1991).

[HSAT89] H. Satz, Nucl. Phys. **B326** (1989) 613.

[JAAB91] J. Alberty and A. Białas, Z. Phys. **C50** (1991) 315.

[JPRH92] J. Pan and R. Hwa, Phys. Rev. **D46** (1992) 4890.

[JPRH93] J. Pan and R. Hwa, Phys. Rev. **D48** (1993) 168.

[KFIA91] K. Fiałkowski, Acta Phys. Pol. **B22** (1991) 397.

[KFIA92a] K. Fiałkowski, Proc. Ringberg Workshop on Multiparticle Production, R. Hwa et al. (eds.), p. 238. Singapore, World Scientific 1992.

[KFIA92b] K. Fiałkowski, Acta Phys. Pol. **B23** (1992) 1255.

[NA2290] I.V. Ajinenko et al. (NA22), Phys. Lett. **B235** (1990) 373.

[PBRP91] P. Brax and R. Peschanski, Phys. Lett. **B253** (1991) 225.

[PCPL91] P. Carruthers et al., Int. J. Mod. Phys. **A6** (1991) 3031.

[PODO90] O. Podobrin, private communication.

[POLY71] A.M. Polyakov, Sov. Phys. **JETP32** (1971) 296, **JETP33** (1971) 850.

[RHTN92] R. Hwa and M. Nazirov, Phys. Rev. Lett. **69** (1992) 741.

[SJOCPC] T. Sjóstrand, Computer Physics Commun. **39** (1986) 347;
T. Sjóstrand and M. Bengtsson, Computer Physics Commun. **43** (1987) 367.
H.U. Bengtsson and T. Sjóstrand; Computer Physics Commun. **46** (1987) 43.

[WOCH90] W. Ochs, Phys. Lett. **B247** (1990) 101.

[WOCH91] W. Ochs, Z. Phys. **C50** (1991) 339.

[WOJW88] W. Ochs and J. Wosiek, Phys. Lett. **B214** (1988) 617.

5

Density integrals

5.1 Introduction

For higher orders ($q > 3$), the normalized factorial moments have large errors and exhibit large fluctuations when evaluated as a function of δ. The first deficiency finds its origin in the lack of statistics, the second in the splitting-up of density spikes due to the particular manner of binning. Needed is a tool that exploits the available statistics in an optimal way and does not split the initial interval.

Based on ideas of Dremin [IDRE88, IDRE89], such a tool is proposed by Carruthers et al. [PLHE92, PLHE93a]. The authors call it the "correlation integral". However, since it corresponds to an integral over an inclusive q-particle density, the correct name is "density integral" and this term shall be used, here.

To clarify the method, consider the one-dimensional second-order factorial moment expressed in terms of integrals over the inclusive density distribution

$$F_2(\delta y) = \frac{1}{M}\sum_{m=1}^{M}\frac{\int_{\Omega_m^2}\rho_2(y_1,y_2)\mathrm{d}y_1\mathrm{d}y_2}{\int_{\Omega_m}\rho_1(y_1)\mathrm{d}y_1\int_{\Omega_m}\rho_1(y_2)\mathrm{d}y_2} \tag{5.1}$$

Here, Ω_m represents a one-dimensional integration domain of size δy and Ω_m^2 a square with edge length δy. The total integration domain of the numerator $\Omega_B = \sum_{m=1}^{M}\Omega_m^2$ is shown in Fig. 5.1a. A point in the m-th box corresponds to a pair (y_1, y_2) of size $|y_1 - y_2| \leq \delta y$ and both particles in the same bin m. Points with $|y_1 - y_2| \leq \delta y$ for which y_1 and y_2 happen *not* to lie in the same but in adjacent bins (e.g. $*$ in Fig. 5.1a) are left out.

The statistics can be approximately doubled when replacing the integration domain of Fig. 5.1a by the strip domain Ω_S shown in Fig. 5.1b. After normalization to the uncorrelated background, the one-dimensional second-order density integral is now defined as

$$\begin{aligned} F_2^D(\delta y) &= \frac{\int_{\Omega_S}\rho_2(y_1,y_2)\mathrm{d}y_1\mathrm{d}y_2}{\int_{\Omega_S}\rho_1(y_1)\rho_1(y_2)\mathrm{d}y_1\mathrm{d}y_2} \\ &= \frac{\int_{\Delta y}\int_{\Delta y}\rho_2(y_1,y_2)\,\theta(\delta y - |y_1 - y_2|)\,\mathrm{d}y_1\mathrm{d}y_2}{\int_{\Delta y}\int_{\Delta y}\rho_1(y_1)\rho_1(y_2)\,\theta(\delta y - |y_1 - y_2|)\,\mathrm{d}y_1\mathrm{d}y_2}\ , \end{aligned} \tag{5.2}$$

where Δy stands for the initial interval and θ is the usual Heaviside unit step function.

For the extension to more dimensions and higher orders, one first needs to define two things: the distance between two particles and, given that distance, a proper multiparticle topology. The three most commonly used topologies are listed below.

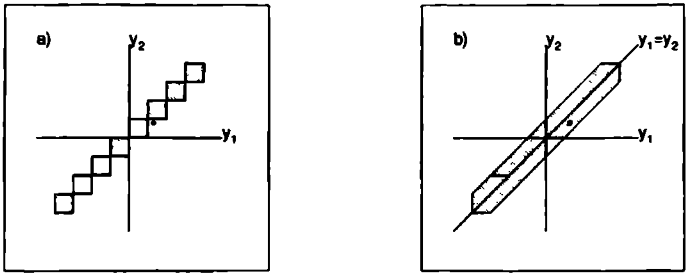

Figure 5.1: *Integration domain for a) the second-order factorial moment and b) the second-order density ingral. (Both in a one-dimensional phase space.)*

1. The snake topology [PCAR91]: A q-tuple according to the snake topology is shown Fig. 5.2a. The size of such an ordered q-tuple is defined as the maximum distance of the successive pairs.
2. The GHP-topology [GHP283]: All pair-wise distances have to be measured (Fig. 5.2b). The largest distance determines the size of the q-tuple.
3. The star topology [PLHE93b]: Now, a q-tuple consists of a central particle surrounded by $q-1$ other particles as pictured in Fig. 5.2c. The size of the q-tuple is given by the distance between the central particle and the most distant among the surrounding ones.

The application of the first topology is rather time consuming and will, therefore, not be used here. An elaboration of the second and third topology, together with experimental results, will be given in sec. 5.2 and sec. 5.3, respectively.

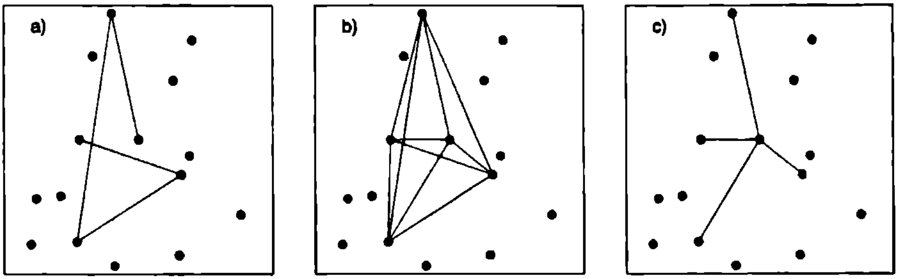

Figure 5.2: *Illustration of a q-tuple considered in three different topologies: a) snake topology, b) GHP-topology, c) star topology*

In its most general form, the density integral can be written as

$$F_q^D(\delta) = \frac{\int\cdots\int \rho_q(p_1,\ldots,p_q)\,\theta(\delta - \text{size } q\text{-tuple})\prod_{j=1}^{q}\frac{d^3p_j}{(2\pi)^3 2E_j}}{\int\cdots\int \rho_1(p_1)\ldots\rho_1(p_q)\,\theta(\delta - \text{size } q\text{-tuple})\prod_{j=1}^{q}\frac{d^3p_j}{(2\pi)^3 2E_j}} \tag{5.3}$$

$$=: \frac{\xi_q(\delta)}{\xi_q^{(n)}(\delta)} \ , \tag{5.4}$$

with p_i the four-momentum of particle i. This is the normalized average number of q-tuples smaller than δ. One can also determine the average number of q-tuples of size included in the interval $[\delta-\epsilon,\delta]$ via the so-called differential density integral

$$DF_q^D(\delta) = \frac{\xi_q(\delta)-\xi_q(\delta-\epsilon)}{\xi_q^{(n)}(\delta)-\xi_q^{(n)}(\delta-\epsilon)} \ . \tag{5.5}$$

Analogously to the factorial cumulant moments (3.53), cumulants are defined in the density integral framework as integrals over the correlation functions $C_q(p_1,\ldots,p_q)$

$$K_q^D(\delta) = \frac{\int\cdots\int C_q(p_1,\ldots,p_q)\,\theta(\delta - \text{size } q\text{-tuple})\prod_{j=1}^{q}\frac{d^3p_j}{(2\pi)^3 2E_j}}{\int\cdots\int \rho_1(p_1)\ldots\rho_1(p_q)\,\theta(\delta - \text{size } q\text{-tuple})\prod_{j=1}^{q}\frac{d^3p_j}{(2\pi)^3 2E_j}} \tag{5.6}$$

$$=: \frac{\zeta_q(\delta)}{\xi_q^{(n)}(\delta)} \ . \tag{5.7}$$

The correlation functions $C_q(p_1,\ldots,p_q)$ are related to the density functions $\rho_q(p_1,\ldots,p_q)$ via formulae (3.47). The differential cumulants are given by

$$DK_q^D(\delta) = \frac{\zeta_q(\delta)-\zeta_q(\delta-\epsilon)}{\xi_q^{(n)}(\delta)-\xi_q^{(n)}(\delta-\epsilon)} \ . \tag{5.8}$$

To indicate what topology is used to determine the density integral, the superscript D will, in the following, be replaced by GHP and $*$ for the GHP-topology and star topology, respectively.

5.2 The GHP-integral

5.2.1 Formalism

In the GHP-topology, the size of a q-tuple is smaller than δ if

$$\prod_{\substack{i=1\\ i\neq j}}^{q}\prod_{j=1}^{q}\theta(\delta - d_{ij}) = 1 \ , \tag{5.9}$$

with d_{ij} the distance between particles i and j of the q-tuple. For the experimental computation of the numerator of $F_q^{GHP}(\delta)$ one needs to count, for each event, the number of

q-tuples of size smaller than δ and then to average over the events. This can mathematically be expressed as

$$\xi_q(\delta) = \left\langle q! \sum_{i_1 < \quad < i_q} \prod_{\substack{\text{all pairs} \\ k_1, k_2}} \theta\left(\delta - d_{i_{k_1}, i_{k_2}}\right) \right\rangle \quad , \tag{5.10}$$

where the sum runs over $i_1 = 1$ to n, with n being the multiplicity of the event.

The denominator of $F_q^D(\delta)$ is obtained from "mixed" events by using a track pool. The multiplicity $n_{\mathcal{P}}$ of a mixed event is taken to be a Poissonian random variable, thereby ensuring that no extra correlations are introduced from the multiplicity distribution. Also for the mixed events the average number of q-tuples of size smaller than δ is determined. Because the tracks of a mixed event are not correlated, $\rho_q(p_1, \ldots, p_q)$ factorizes to $\rho_1(p_1) \ldots \rho_1(p_q)$ and $\xi_q^{(n)}(\delta)$ is obtained after multiplication by

$$\frac{\langle n \rangle^q}{\langle n_{\mathcal{P}} \rangle_{\mathcal{P}}^q} \tag{5.11}$$

to correct for the difference in average multiplicity $\langle n_{\mathcal{P}} \rangle_{\mathcal{P}}$ of the Poissonian and average multiplicity $\langle n \rangle$ of the experimental distribution.

To understand the meaning of this procedure, consider the evaluation of the density integral in full phase space, for all charged particles. Then, $\delta = \delta_{max}$ and the θ-functions in (5.3) are irrelevant. Straight from definition (5.3) one obtains

$$F_q^{GHP}(\delta_{max}) = \frac{\left\langle n^{[q]} \right\rangle}{\langle n \rangle^q} \tag{5.12}$$

and via the above described procedure

$$F_q^{GHP}(\delta_{max}) = \frac{\left\langle n^{[q]} \right\rangle}{\left\langle n_{\mathcal{P}}^{[q]} \right\rangle_{\mathcal{P}}} \frac{\langle n_{\mathcal{P}} \rangle_{\mathcal{P}}^q}{\langle n \rangle^q} \quad . \tag{5.13}$$

Since for a Poisson distribution

$$\left\langle n_{\mathcal{P}}^{[q]} \right\rangle_{\mathcal{P}} = \langle n_{\mathcal{P}} \rangle_{\mathcal{P}}^q \quad , \tag{5.14}$$

(5.12) and (5.13) are the same. Note that this is also the value one obtaines for the usual normalized factorial moment determined for the initial interval (i.e. for $M = 1$ in (4.4)).

In the determination of the unnormalized cumulants, quantities like

$$\rho_{q_1}(p_1, \ldots, p_{q_1})\, \rho_{q-q_1}(p_{q_1+1}, \ldots, p_q) \tag{5.15}$$

and

$$\rho_{q_1}(p_1, \ldots, p_{q_1})\, \rho_{q_2}(p_{q_2}, \ldots, p_{q_1+q_2})\, \rho_{q-q_1-q_2}(p_{q_1+q_2+1}, \ldots, p_q) \tag{5.16}$$

etc. are involved. As mentioned above, $\rho_1(p_1) \ldots \rho_1(p_q)$ can be obtained by taking tracks from q different events. Analogously, taking q_1 tracks from one event and $q - q_1$ tracks from another event yields (5.15) since then the first q_1 tracks are not correlated with the other $q - q_1$. This procedure can be extended to whatever combination of density functions. It is, however, not easy to implement for higher orders. For second and third order, NA22 results are presented in [NA2294], where the size of a q-tuple is defined as the invariant mass M_{inv}, defined as the square root of

$$M_{inv}^2 = \left(\sum_{k=1}^{q} p_k\right)^2 \tag{5.17}$$

However, in the star topology, the determination of $\zeta_q(\delta)$ is accomplished in a much easier way. The cumulants will, therefore, only be considered in sec. 5.3.

5.2.2 Experimental results

5.2.2.1 The moving box

To be able to compare the results of the GHP-integral with the conventional normalized factorial moments, it is convenient to use the variables y, φ and p_T (as usual, transformed according to (4.1)) and to define the distance between two particles i and j as

$$d_{i,j} = \max\left(|y_i - y_j|\,, |\varphi_i - \varphi_j|\,, |(p_T)_i - (p_T)_j|\right)^3 \tag{5.18}$$

I.e. the size of the q-tuple is defined by the smallest box volume that encloses the q-tuple. The determination of ξ_q can now be compared with moving around a box in the full phase space under consideration and counting the number of q-tuples fitting into the box.

In Fig. 5.3, conventional F_2 and F_3 are compared to the density-integral versions F_2^{GHP} and F_3^{GHP}. For the conventional normalized factorial moments the box volume equals M^{-3}. Although (5.12),(5.13),(5.14) lead to $F_q(\text{box vol} = 1) = F_q^{GHP}(\text{box vol} = 1)$, the two values differ on Fig. 5.3. The first reason is that (5.14) only holds for an exact Poisson distribution. Deviations from an exact Poissonian are caused by the finite number of events used and by an upper limit on the multiplicity set for computational reasons. The second reason lies in the fact that (5.12) is only true for an infinite number of events, otherwise (5.12) is a biased estimator of (5.3). The availability of only a finite number of events has been neglected in the determination of the factorial moments. In Sect. 5.3.1 this issue will be treated in more detail.

As anticipated, in Fig. 5.3 one indeed observes that statistical errors are strongly reduced in the F_q^{GHP}. This, in principle, allows the analysis to be carried down to much smaller box volumes. It, furthermore, now allows a comparison of different charge combinations.

The solid lines for $q = 2$ correspond to the Fiałkowski fit

$$F_2(\text{box vol}) = a\,(\text{box vol})^{-b} + c + 1 \quad . \tag{5.19}$$

Results are given in Tab. 5.1 for the range $0.125 \leq$ box volume ≤ 0.001, as indicated in the figure. This fit range is chosen on the basis of Fig. 5.3a: The fits start with the second point, since the first point is not compatible with the form (5.19), in particular for the unlike-charged sample. The end point of the fit range coincides with the smallest box volume yielding meaningful normalized factorial moments. The same fit region is used for Fig. 5.3c. However, one should realise that for the same box volume F_q and F_q^{GHP} are determined in a different total integration domain. Whenever, in the process of fitting, the constant c is

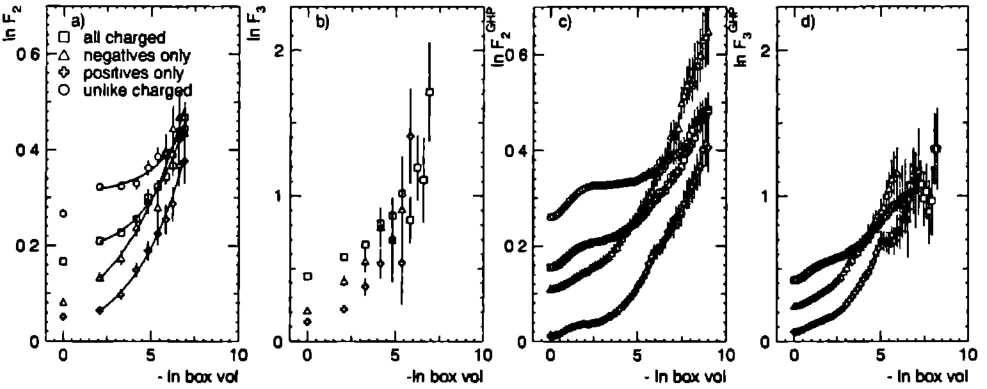

Figure 5.3: *Comparison of a), b) conventional factorial moments F_2 and F_3 in three dimensions to c), d) F_2^{GHP} and F_3^{GHP} obtained from the density integral method in GHP-topology. Solid lines in a) and c) correspond to fits according to (5.19).*

found to be compatible with zero, it is fixed to zero in order to obtain more precise values for the other parameters. Results are given for fits neglecting correlations (and consequently the χ^2/NDF values are very low). Remember, however, that for F_2 in the all-charged case the parameters remain the same within errors if bin-size correlations are taken into account.

		all charged	unlike charged	negatives only	positives only
F_2	a	0.012 ± 0.007	0.003 ± 0.005	0.028 ± 0.001	0.072 ± 0.003
	b	0.50 ± 0.09	0.6 ± 0.2	0.0405 ± 0.008	0.314 ± 0.008
	c	0.20 ± 0.02	0.36 ± 0.02	0	0
	χ^2/NDF	3.1/6	2.5/6	1.1/7	4.1/7
F_2^{GHP}	a	0.009 ± 0.005	0.0006 ± 0.0009	0.0115 ± 0.0003	0.04 ± 0.02
	b	0.45 ± 0.07	0.7 ± 0.2	0.469 ± 0.004	0.37 ± 0.06
	c	0.20 ± 0.01	0.380 ± 0.006	0	0.08 ± 0.03
	χ^2/NDF	2.3/30	1.4/30	8.1/31	1.7/30

Table 5.1: *Results of fits to the data presented in Fig. 5.3a and c, according to (5.19).*

The parameter values given in Tab. 5.1 show a striking difference for unlike- and like-charged pairs. While (+−) pairs are dominated by long-range correlations (large c), these are smaller or absent in the case of (−−) and (++). Correspondingly, the parameter a is compatible with zero for (+−), but relatively large for (−−) and (++). Consequently, b is determined well only for the latter.

As in the case of the conventional F_q, the modified power-law assumption,

$$\ln F_q^{GHP}(\text{box vol}) = a_q + \frac{\alpha_q}{\alpha_2} \ln F_2(\text{box vol}) \quad , \tag{5.20}$$

can be fitted to the data. The fits are represented by full lines on the Ochs-Wosiek plot, Fig. 5.4. As can be seen on the figure, (5.20) only holds approximately. The ratios α_q/α_2 serve as input for the determination of the Lévy index μ, by means of (4.15), and the Ginzburg-Landau parameter ν, via (4.16). Results are collected in Tab. 5.2. Again, μ is found to be larger than 2, but the fit quality of (4.15) is very bad. While χ^2 is lower for (4.15) than for (4.16) in the case of conventional F_q , the situation is reversed for the F_q^{GHP}. The values obtained for μ and ν again exclude a second-order phase transition.

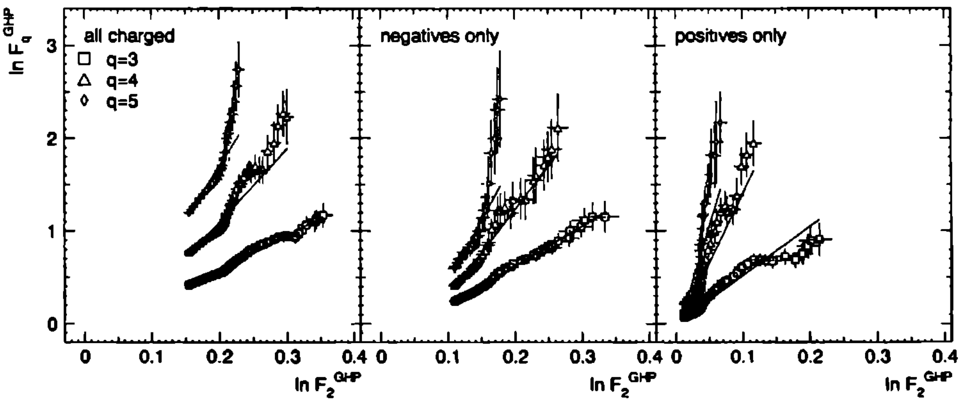

Figure 5.4: *The density integrals* F_q^{GHP}(box vol) *in the Ochs-Wosiek representation. The full lines represent fits according to (5.20).*

	all charged	negatives only	positives only
α_3/α_2	3.81 ± 0.09	4.3 ± 0.2	5.3 ± 0.2
α_4/α_2	8.0 ± 0.3	9.4 ± 0.5	15.0 ± 0.5
α_5/α_2	11.8 ± 0.3	13 ± 1	24 ± 1
μ	2.51 ± 0.04	2.82 ± 0.06	3.55 ± 0.03
χ^2/ NDF	29/2	23/2	42/2
ν	1.87 ± 0.02	2.01 ± 0.03	2.40 ± 0.02
χ^2/ NDF	9.7/2	9.1/2	14/2

Table 5.2: *The slopes* α_q/α_2 *obtained by fitting (5.20) to the data of Fig. 5.4 and results of fits according to (4.15) and (4.16).*

5.2.2.2 The GHP-integral in Q^2

In this section, the pair-wise distance is defined directly from the four-vectors p_i as

$$d_{i,j} = Q^2_{i,j} = (p_i - p_j)^2 \quad . \tag{5.21}$$

Therefore, a q-tuple is smaller than Q^2 if

$$\prod_{i<j} \theta\left(Q^2 - Q^2_{i,j}\right) = 1 \quad . \tag{5.22}$$

Note that the $Q^2_{i,j}$ of a pion pair is linked with the invariant mass of the pair via

$$M^2_{inv} = (p_i + p_j)^2 = Q^2_{i,j} + 4m^2_\pi \quad . \tag{5.23}$$

In Fig. 5.5, the NA22 data are plotted as a function of $-\ln Q^2$. On this figure, the following observations can be made.

i) The errors and fluctuations are largely reduced, as compared to the multidimensional factorial moments.

ii) The distance measure Q^2 essentially shows a similarly steep rise as the three-dimensional analysis.

iii) Contrary to the results in y (Sect. 3.1.2.2), the positives-only and negatives-only samples behave similarly here, but are now much steeper than the all-charged sample.

iv) F_2^{GHP} is flatter for unlike-charged pairs than for the all-charged, positives-only and negatives-only samples.

The first two observations demonstrate the strength of the method and the proper variable. The last two observations directly demonstrate the large influence of like-charged particle combinations on the rise of the factorial moments.

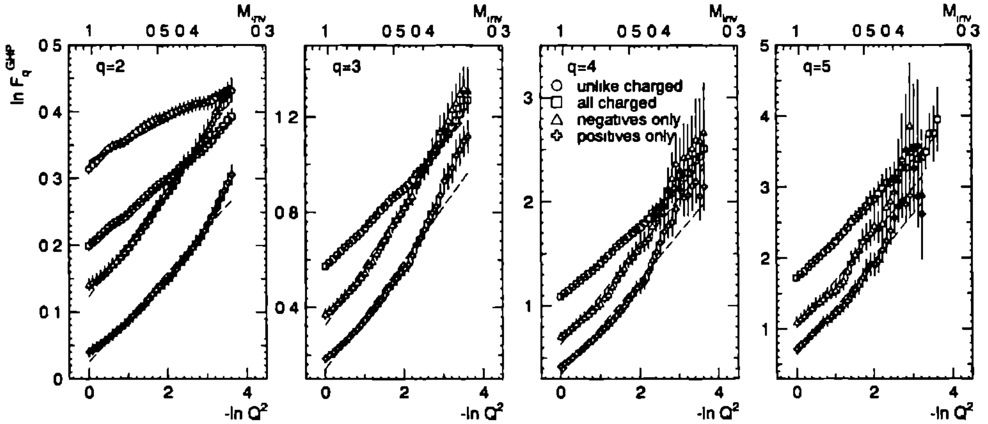

Figure 5.5: *The* $\ln F_q^{GHP}$ *as function of* $-\ln Q^2$. *Note that* $-\ln Q^2 = 0.65$ *corresponds to the peak of the* ρ *meson and* 1.77 *is the value corresponding to the* K^0 *mass.*

The solid lines correspond to fits according to a power law in Q^2, i.e.

$$F_q^{GHP}\left(Q^2\right) = a_q \left(Q^2\right)^{-\phi_q} \quad ; \tag{5.24}$$

the dashed ones (for $q = 2$ only) to fits according to the Fiałkowski proposition

$$F_2^{GHP}\left(Q^2\right) = a \left(Q^2\right)^{-b} + c + 1 \quad . \tag{5.25}$$

The fit parameters are given in Tab. 5.3. Again, the parameter c is fixed to zero if it is found to be compatible with zero. It can be seen that the negatives-only sample now is a factor 1.2 (ϕ_5) to 1.6 (ϕ_2) steeper than the all-charged sample. A factor 2 has been predicted [MGYU92] on the basis of Bose-Einstein correlations, but has not been observed in the analysis in y, φ and p_T so far.

order		all charged	negatives only	positives only	unlike charged
2	range	0.02674	0.02674	0.02674	0.02674
	a_2	1.219 ± 0.003	1.131 ± 0.002	1.026 ± 0.002	1.386 ± 0.002
	ϕ_2	0.051 ± 0.001	0.081 ± 0.001	0.067 ± 0.001	0.032 ± 0.001
	$\chi^2/$NDF	2.4/35	17/35	36/35	15/35
2	range	0.02674	0.02674	0.02674	0.02674
	a	0.228 ± 0.003	0.153 ± 0.001	0.11 ± 0.03	0.389 ± 0.002
	b	0.207 ± 0.006	0.362 ± 0.004	0.37 ± 0.05	0.099 ± 0.002
	c	0	0	-0.7 ± 0.3	0
	$\chi^2/$NDF	3.8/35	4.6/35	1.5/34	20/35
3	range	0.02674	0.02674	0.02674	
	a_3	1.751 ± 0.007	1.38 ± 0.01	1.15 ± 0.05	
	ϕ_3	0.177 ± 0.002	0.253 ± 0.004	0.227 ± 0.003	
	$\chi^2/$NDF	13/35	31/35	65/35	
4	range	0.02674	0.02674	0.02674	
	a_4	2.90 ± 0.02	1.88 ± 0.02	1.41 ± 0.01	
	ϕ_4	0.358 ± 0.006	0.47 ± 0.01	0.45 ± 0.01	
	$\chi^2/$NDF	7.8/35	25/35	52/35	
5	range	0.02674	0.03950	0.03950	
	a_5	5.45 ± 0.08	2.78 ± 0.07	1.89 ± 0.04	
	ϕ_5	0.56 ± 0.01	0.66 ± 0.02	0.66 ± 0.02	
	$\chi^2/$NDF	3.1/35	13/31	23/31	

Table 5.3: *Results of fits to the data presented in Fig. 5.5, according to (5.24) and (5.25). The fit range in* $(\mathrm{GeV/c})^2$*: the largest value = 1 and the smallest as given in the table.*

In Fig. 5.6, $\ln F_2^{GHP}$ and $\ln F_3^{GHP}$ are plotted as a function of $-\ln Q^2$ for event samples in which each particle of the q-tuple has transverse momentum p_T in the region indicated on the figure. The results of the fits according to formulae (5.24) and (5.25) are summarized in Tab. 5.4.

A comparison of figs. 5.5 and 5.6 and tabs. 5.3 and 5.4 reveals several interesting features:

i) The difference in $-\ln Q^2$ dependence of $F_2^{GHP}(+-)$ and $F_2^S(--)$ seen in Fig. 5.5 is essentially due to the particles with $p_T > 0.15$ GeV/c, where $F_2^{GHP}(+-)$ even decreases.

ii) The slope $\phi_2(--)$ is *larger* for $p_T > 0.15$ GeV/c than for $p_T < 0.15$ GeV/c. This effect is much less pronounced with a p_T-cut of 0.3 GeV/c.

iii) $\phi_2(--)$ is smaller for $p_T < 0.15$ GeV/c than for the uncut data sample.

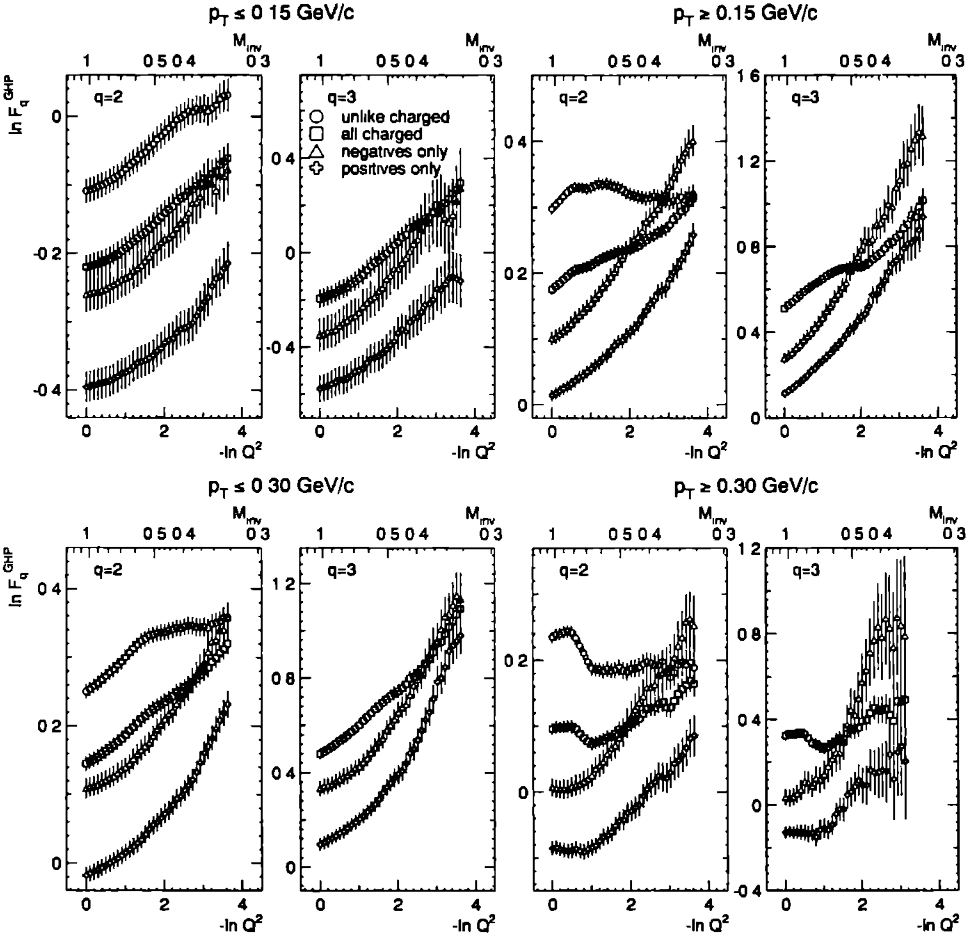

Figure 5.6: *The second- and third-order GHP-integral for different* p_T*-regions.*

$p_T \leq 0.15$ GeV/c					
order		all charged	negatives only	positives only	unlike charged
2	range	0.02674	0.02674	0.02674	0.02674
	a_2	0.792 ± 0.002	0.756 ± 0.004	0.660 ± 0.003	0.891 ± 0.002
	ϕ_2	0.046 ± 0.002	0.053 ± 0.002	0.046 ± 0.002	0.043 ± 0.002
	χ^2/NDF	22/35	3.6/35	8.9/35	3.8/35
2	range	0.02674	0.02674	0.02674	0.02674
	a	0.15 ± 0.15	0.072 ± 0.064	0.020 ± 0.015	0.012 ± 0.002
	b	0.18 ± 0.13	0.33 ± 0.12	0.56 ± 0.19	0.70 ± 0.03
	c	-0.36 ± 0.16	-0.31 ± 0.07	-0.35 ± 0.02	-0.094 ± 0.006
	χ^2/NDF	1.1/34	1.3/34	0.48/34	3.6/34
3	range	0.02674	0.02674	0.02674	
	a_3	0.800 ± 0.006	0.67 ± 0.01	0.538 ± 0.006	
	ϕ_3	0.136 ± 0.004	0.17 ± 0.01	0.138 ± 0.006	
	χ^2/NDF	2.9/35	3.3/35	3.8/35	

$p_T \geq 0.15$ GeV/c					
order		all charged	negatives only	positives only	unlike charged
2	range	0.02674	0.02674	0.02674	0.02674
	a_2	1.196 ± 0.002	1.085 ± 0.002	0.999 ± 0.002	1.381 ± 0.002
	ϕ_2	0.032 ± 0.001	0.081 ± 0.001	0.061 ± 0.001	-0.001 ± 0.001
	χ^2/NDF	11.6/35	18/35	30/35	41/35
2	range	0.02674	0.02674	0.02674	0.02674
	a	0.200 ± 0.002	0.19 ± 0.06	0.09 ± 0.02	0.76 ± 0.03
	b	0.154 ± 0.004	0.31 ± 0.06	0.39 ± 0.06	-0.0016 ± 0.0028
	c	0	-0.09 ± 0.06	-0.07 ± 0.03	-0.38 ± 0.03
	χ^2/NDF	9.0/35	1.7/34	1.1/34	41/34
3	range	0.02674	0.02674	0.02674	
	a_3	1.691 ± 0.007	1.26 ± 0.01	1.085 ± 0.006	
	ϕ_3	0.107 ± 0.003	0.269 ± 0.006	0.202 ± 0.004	
	χ^2/NDF	27/35	21/35	22/35	

Table 5.4: *Same as Tab. 5.3 but for different p_T-regions.*

From the last two observations (for negatives) one would conclude that in Q^2 the intermittency effect is weaker at low p_T than at higher p_T. However, in a one-dimensional (rapidity) analysis of the all-charged sample in this experiment, it was concluded that, on the contrary, intermittency is strongest when small-p_T particles are selected (Sect. 3.1.2.3). This is still visible when comparing ϕ_2 and ϕ_3 for the all-charged sample for $p_T < 0.15$ GeV/c and $p_T > 0.15$ GeV/c in Tab. 5.4.

		$p_T \leq 0.30$ GeV/c			
order		all charged	negatives only	positives only	unlike charged
2	range	0.02674	0.02674	0.02674	0.02674
	a_2	1.151 ± 0.002	1.086 ± 0.003	0.960 ± 0.002	1.303 ± 0.003
	ϕ_2	0.047 ± 0.001	0.067 ± 0.001	0.062 ± 0.001	0.031 ± 0.001
	χ^2/ NDF	2.0/35	23/35	41/35	33/35
2	range	0.02674	0.02674	0.02674	0.02674
	a	0.69 ± 0.03	0.105 ± 0.002	0.05 ± 0.01	15.06 ± 0.04
	b	0.075 ± 0.004	0.389 ± 0.006	0.54 ± 0.08	0.0028 ± 0.0002
	c	-0.53 ± 0.03	0	-0.06 ± 0.02	-14.76 ± 0.04
	χ^2/ NDF	1.8/34	2.0/35	0.79/34	31/34
3	range	0.02674	0.02674	0.02674	
	a_3	1.573 ± 0.007	1.295 ± 0.009	1.024 ± 0.006	
	ϕ_3	0.155 ± 0.003	0.206 ± 0.005	0.209 ± 0.004	
	χ^2/ NDF	17/35	40/35	82/35	

		$p_T \geq 0.30$ GeV/c			
order		all charged	negatives only	positives only	unlike charged
2	range	0.02674	0.02674	0.02674	0.02674
	a_2	1.081 ± 0.002	0.976 ± 0.003	0.895 ± 0.002	1.261 ± 0.003
	ϕ_2	0.016 ± 0.001	0.069 ± 0.002	0.043 ± 0.002	-0.019 ± 0.001
	χ^2/ NDF	67/35	24/35	36/35	60/35
2	range	0.02674	0.02674	0.02674	0.02674
	a	0.021 ± 0.001	0.07 ± 0.03	0.03 ± 0.01	0.0886 ± 0.009
	b	1.1 ± 0.2	0.5 ± 0.1	0.6 ± 0.1	-1.1 ± 0.2
	c	0.089 ± 0.004	-0.08 ± 0.03	-0.12 ± 0.01	0.198 ± 0.007
	χ^2/ NDF	30/34	15/34	9.8/34	32/34
3	range	0.02674	0.02918	0.02918	
	a_3	1.347 ± 0.008	0.97 ± 0.01	0.848 ± 0.008	
	ϕ_3	0.032 ± 0.005	0.25 ± 0.01	0.102 ± 0.009	
	χ^2/ NDF	43//35	23/34	24/34	

Table 5.4: *continued*

The reason for this apparent contradiction lies in the fact that factorial moments such as F_2 have very different $-\ln Q^2$ and p_T-dependence for like-charged ($\pm\pm$) and unlike-charged ($+-$) pairs. This hampers easy interpretation of the all-charged sample. It is, therefore, dangerous to base conclusions about dynamical properties on all-charged data only, without proper analysis of the different charge combinations.

A further warning is needed concerning the interpretation of correlation-integral results for data samples in restricted p_T intervals. In [EDWP92] it is shown that the stronger rise of $F_2(\delta y)$ with decreasing δy, and the slower rise of $F_2^{GHP}(Q^2)$ with decreasing Q^2 for small-p_T particles, as observed in our data, is to a large extent a consequence of a kinematical cut on the two-particle invariant-mass distribution. This result is obtained under the assumption that the two-particle correlation function is a rapidly decreasing function of the invariant mass (or Q^2) in restricted p_T-intervals, without an explicit dependence on the other kinematical variables of the pair. Integration of such a correlation function over the appropriate variables in a p_T-restricted phase space leads to the observed results.

For the uncut sample, the modified power law

$$\ln F_q^{GHP}\left(Q^2\right) = a_q + \frac{\alpha_q}{\alpha_2} \ln F_2\left(Q^2\right) \quad , \tag{5.26}$$

the Lévy index μ and the Ginzburg-Landau parameter ν have been examined. The Ochs-Wosiek plot is given in Fig. 5.7, the fit results are given in Tab. 5.5. Although the values of μ are smaller than those obtained for F_q^{GHP}(box vol). They are still larger than 2, thus confirming that the density fluctuations are not of the Lévy type. Also the paramter ν has decreased w.r.t. the values obtained for F_q^{GHP}(box vol). They are, however, still incompatible with a second-order phase transition.

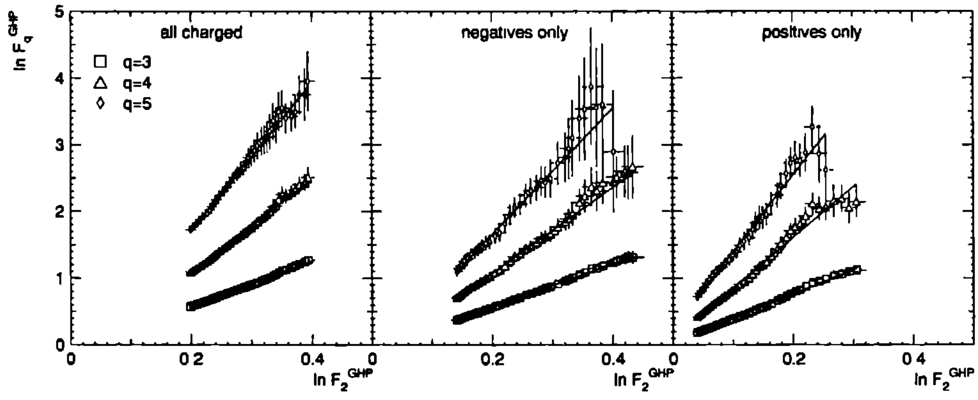

Figure 5.7: *Ochs-Wosiek plots for $F_q^{GHP}(Q^2)$ for the samples "all charged", "negatives only" and "positives only".*

5.2.2.3 Influence of possible biases

At very small Q^2, the increase of $F_2^{GHP}(+-)$ with decreasing Q^2 is at least partially due to Dalitz misidentification and undetected γ-conversions. To estimate this effect, a procedure borrowed from [NA35PC] is followed. First, the differential form of the density integral DF_2^{GHP} is determined with distance measure $M_{inv} - 2m_\pi$ near threshold, where this variable is very sensitive to biases like $e^\pm$ misidentification and double counting of tracks.

	all charged	negatives only	positives only
range	0.02674	0.02674	0.02674
α_3/α_2	3.48 ± 0.08	3.28 ± 0.09	3.65 ± 0.09
range	0.02674	0.02674	0.02674
α_4/α_2	7.1 ± 0.2	6.4 ± 0.2	7.6 ± 0.2
range	0.02674	0.03950	0.03950
α_5/α_2	11.2 ± 0.4	9.4 ± 0.5	11.4 ± 0.5
μ	2.30 ± 0.04	2.10 ± 0.05	2.30 ± 0.04
$\chi^2/$NDF	13/2	11/2	26/2
ν	1.77 ± 0.02	1.68 ± 0.02	1.82 ± 0.02
$\chi^2/$NDF	2.1/2	3.1/2	7.5/2

Table 5.5: *The slopes in the Ochs-Wosiek plot Fig. 5.7 and the derived parameters μ and ν.*

In Fig. 5.8, $DF_2^{GHP}(M_{inv} - 2m_\pi)$ is shown for the different charge combinations. In all cases, the data indeed exhibit a sharp peak near zero, pointing to a possible bias of double counting (Fig. 5.8b and c) and Dalitz decay or γ-conversion (Fig. 5.8d). Events contributing to the first bin in figs. 5.8b and 5.8c have been investigated visually on the scanning table for double counting of single tracks. The corresponding tracks could be positively identified as double tracks by charge conservation, double minimum ionization and/or visible separation at the end of the sensitive volume of the bubble chamber. Furthermore, it has been verified that for like-charged pairs the small-mass peaking can be qualitatively reproduced by the FRITIOF2.0 Monte Carlo when including Bose-Einstein correlations. The peak for like-charged pairs is, therefore, considered to be real. The peak at small mass for unlike-charged pairs can be reproduced by FRITIOF2.0 only when γ-conversion is introduced as a bias (see sec. 5.2.2.4).

To see the influence of the peaks on $F_q^{GHP}(Q^2)$, every pair contributing to $(M_{inv} - 2m_\pi) <$ 0.002 GeV, is given a weight such that $DF_2^{GHP}(M_{inv} - 2m_\pi)$ becomes flat, more precisely $DF_2^{GHP}(M_{inv} - 2m_\pi) = 2$ in the presented case (of course this cut can be applied separately and with different cut values for the various charge combinations). The influence of the peaks on $F_2^{GHP}(Q^2)$ is shown in Fig. 5.9. Removing the $(+-)$-peak gives the most dramatic effect. The influence on the fit parameters of (5.24) and (5.25) can be judged from Tab. 5.6. The intermittency indices ϕ_2 and b decrease, but do not become compatible with zero. Also the constant c of (5.25), which is supposed to take into account possible non-singular long-range correlations, decreases. $F_3^{GHP}(Q^2)$ (not shown) only changes within errors. For higher-order moments the statistics does not allow to consider Q^2 values small enough to show a difference.

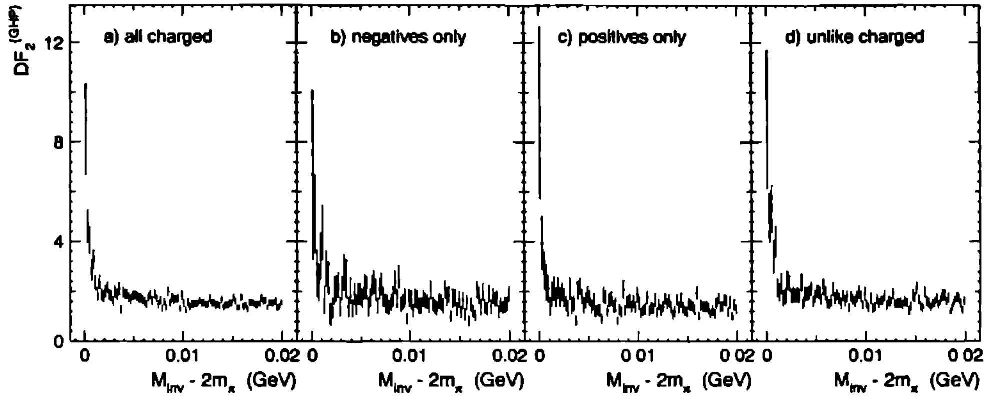

Figure 5.8: *The second-order differential density function in $M_{inv} - 2m_\pi$ for a)* cc *pairs, b) $--$ pairs, c) $++$ pairs and d) $+-$ pairs. This plot serves as a test for possible biases, such as: Dalitz misidentification, undetected γ-conversions and track double counting.*

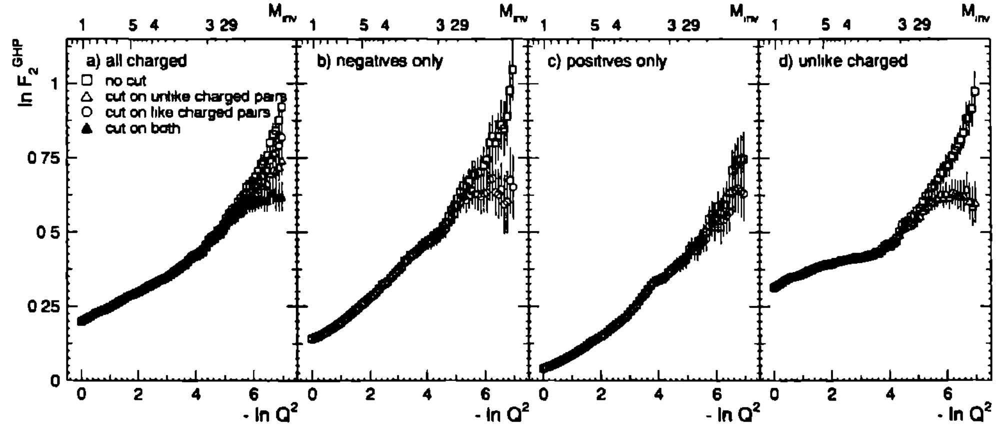

Figure 5.9: *Influence of the suppression of small $M_{inv} - 2m_\pi$ values on a) $F_2^{GHP}(cc)$, b) $F_2^{GHP}(--)$, c) $F_2^{GHP}(++)$ and d) $F_2^{GHP}(+-)$, where Q^2 is used as distance measure.*

		no cut	cut on unlike charged pairs	cut on like charged pairs	cut on both
all charged	a_2	1.191 ± 0.003	1.99 ± 0.003	1.195 ± 0.002	1.203 ± 0.002
	ϕ_2	0.069 ± 0.001	0.064 ± 0.001	0.0657 ± 0.0005	0.0609 ± 0.0005
	$\chi^2/$NDF	418/68	186/68	267/68	108/67
	a	0.09 ± 0.01	0.15 ± 0.02	0.12 ± 0.01	0.225 ± 0.001
	b	0.36 ± 0.02	0.27 ± 0.02	0.31 ± 0.02	0.213 ± 0.002
	c	0.15 ± 0.01	0.08 ± 0.02	0.11 ± 0.02	0
	$\chi^2/$NDF	32/67	15/67	19/67	21/68
negatives only	a_2	1.118 ± 0.002		1.126 ± 0.002	
	ϕ_2	0.090 ± 0.001		0.084 ± 0.001	
	$\chi^2/$NDF	97/68		32/68	
	a	0.25 ± 0.03		0.52 ± 0.09	
	b	0.26 ± 0.02		0.15 ± 0.02	
	c	-0.11 ± 0.03		-0.38 ± 0.09	
	$\chi^2/$NDF	12/67		19/67	
positives only	a_2	1.012 ± 0.003		1.014 ± 0.002	
	ϕ_2	0.078 ± 0.001		0.076 ± 0.001	
	$\chi^2/$NDF	156/68		107/68	
	a	0.17 ± 0.02		0.21 ± 0.02	
	b	0.28 ± 0.02		0.24 ± 0.02	
	c	-0.13 ± 0.02		-0.18 ± 0.03	
	$\chi^2/$NDF	16/67		18/67	
unlike charged	a_2	1.359 ± 0.002	1.371 ± 0.002		
	ϕ_2	0.0464 ± 0.0006	0.0394 ± 0.0006		
	$\chi^2/$NDF	336/68	138/68		
	a	0.032 ± 0.004	0.10 ± 0.02		
	b	0.51 ± 0.02	0.27 ± 0.03		
	c	0.373 ± 0.007	0.29 ± 0.02		
	$\chi^2/$NDF	86/67	76/67		

Table 5.6: *Results of fits to the data presented in Fig. 5.9 according to (5.24) and (5.25), respectively. Range in* Q^2*:* $1 - 0.9419 \times 10^{-3}$ $(\mathrm{GeV/c})^2$.

The same analysis has been repeated for F_2^{GHP}(box vol) and the ordinary three-dimensional factorial moments. They both lead to the same conclusions. Because of smaller errors, only

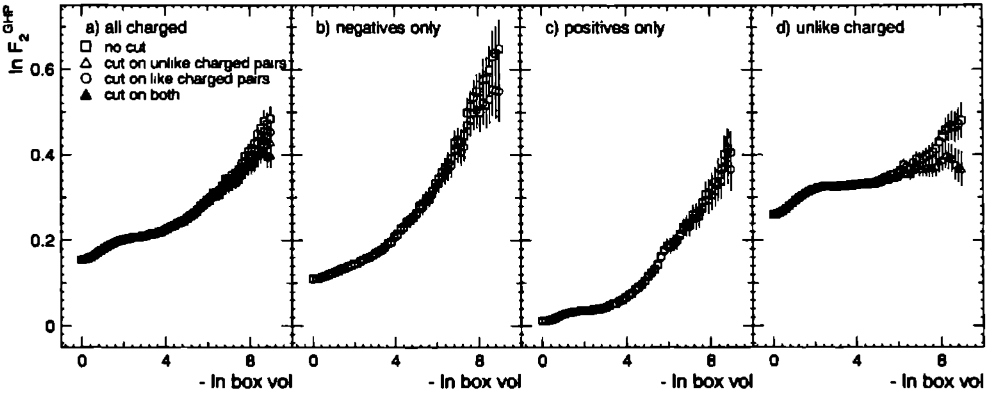

Figure 5.10: *Same as Fig. 5.9 but with* box vol *as distance measure.*

		no cut	cut on unlike charged pairs	cut on like charged pairs	cut on both
all charged	a	0.016 ± 0.004	0.025 ± 0.007	0.020 ± 0.006	0.035 ± 0.01
	b	0.37 ± 0.03	0.31 ± 0.03	0.34 ± 0.03	0.27 ± 0.03
	c	0.18 ± 0.01	0.17 ± 0.01	0.18 ± 0.01	0.16 ± 0.02
	$\chi^2/$NDF	5.1/43	7.3/43	6.2/43	9.2/43
unlike charge	a	0.002 ± 0.001	0.008 ± 0.008		
	b	0.53 ± 0.07	0.3 ± 0.1		
	c	0.374 ± 0.006	0.36 ± 0.02		
	$\chi^2/$NDF	3.5/43	6.1/43		
negatives only	a	0.04 ± 0.01		0.06 ± 0.02	
	b	0.34 ± 0.03		0.28 ± 0.03	
	c	0.06 ± 0.02		0.03 ± 0.03	
	$\chi^2/$NDF	4.0/43		5.9/43	
positives only	a	0.031 ± 0.007		0.04 ± 0.01	
	b	0.33 ± 0.03		0.30 ± 0.03	
	c	-0.04 ± 0.01		-0.05 ± 0.02	
	$\chi^2/$NDF	16/43		18/43	

Table 5.7: *Results of fits to the data presented in Fig. 5.9 according to (5.24) and (5.25), respectively. Range in Q^2:* $1 - 0.9419 \times 10^{-3}$ (GeV/c)^2.

F_q^{GHP}(box vol) will be discussed here. As in the case of Q^2, only the second order is sensitive to the peaks in Fig. 5.8 (see Fig. 5.10). The $F_2^{GHP}(++)$ and $F_2^{GHP}(--)$ change within errors. However, $F_2^{GHP}(+-)$ becomes almost completely flat and the fit parameter b decreases considerably (Tab. 5.7). The effect of the different cuts on the all-charged sample, however, gives results very close to each other.

One should be aware, that in the analysis done in this section, one assumes the peaks in $DF_2^{GHP}(M_{inv} - 2m_\pi)$ near zero to be completely caused by experimental biases (already disproved for the case of like-charged pairs). The results, therefore, reflect the worst possible case. In addition, note that in figs. 5.5, 5.6 and 5.7 the data are only given for $-\ln Q^2 < 3.64$ ($Q^2 > 0.0264$ GeV^2), which is far away from the region where possible biases have influence on the data.

5.2.2.4 Monte-Carlo models

Besides the model versions FRITIOF2.0 plain and FRITIOF2.0 + BE-correlations used throughout this thesis, this section will make use of FRITIOF2.0 + BE + an additional "bias", to take into account Dalitz decay and undetected γ-conversions.

Dalitz decay is treated according to the procedure used in the Monte Carlo. Contamination from undetected γ-conversion has been studied in [FBTH92] and is introduced into the model using the rate (0.25% of all γ's), the γ effective-mass distribution and the electron-energy ratio as estimated from the γ's detected in this experiment.

The Monte Carlo results are given[1] in Fig. 5.11 for second order and in Fig. 5.12 for higher orders.

The plain version is not able to describe the data for any charge combination of any

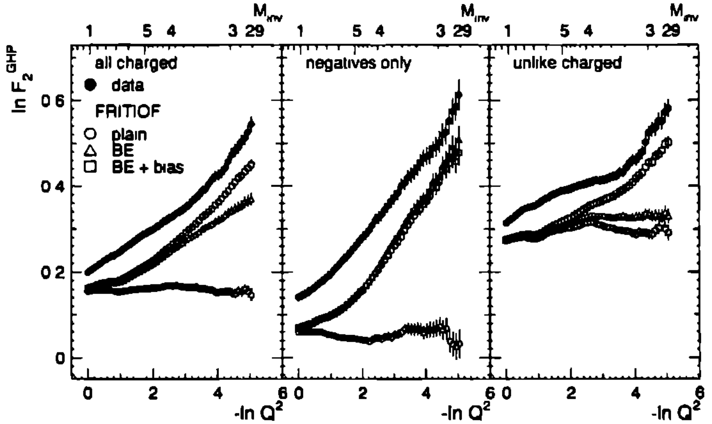

Figure 5.11: *The* $\ln F_2^{GHP}(Q^2)$ *in the data compared to FRITIOF2.0, FRITIOF2.0 + BE and FRITIOF2.0 + BE + a bias accounting for Dalitz decay and undetected* γ*-conversions.*

---

[1] Note that on figs. 5.11 and 5.12, as in Fig. 5.9, the data are shown for Q^2 down to 10^{-3}(GeV)^2, while in figs. 5.5 and 5 6, the smallest Q^2 is 0.0264 (GeV/c)^2.

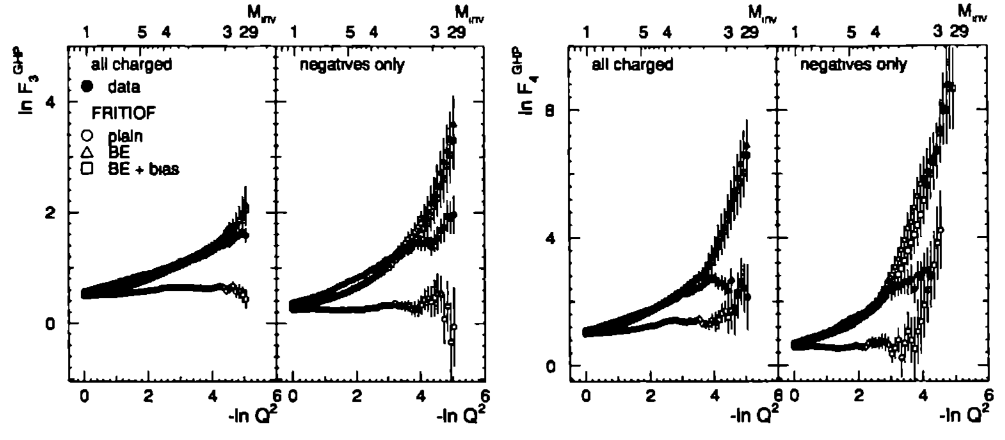

Figure 5.12: *Same as Fig. 5.11 for orders* $q = 3, 4$.

order. The predictions show no increase at all for $q = 2, 3$. For $q = 4$ an increase can be seen, especially for small Q^2-values ($-\ln Q^2 > 4$, i.e. $Q^2 < 0.018$ (GeV/c)^2). Remember that also for the three-dimensional F_4 and F_5 distributions FRITIOF2.0 plain yields an increase at small box volumes.

Including Bose-Einstein correlations, the model results for $F_2^{GHP}(--)$ differ from the data almost only by a shift. However, for higher orders the algorithm to include Bose-Einstein correlations into the model leads to an overestimation.

If, on top of the Bose-Eeinstein correlations, a bias is added in order to take into account Dalitz decay and (0.25%) undetected γ-conversions, the FRITIOF results for $F_2^{GHP}(cc)$ and $F_2^{GHP}(+-)$ show the same increase as the data, but the values stay too low. Naturally, this additional bias does not affect the GHP-integral determined for the negatively-charged sample. Conform to the analysis in the previous section, the effect of the bias cannot be seen for orders $q \geq 3$. However, for second-order, the effect is predicted to be visible at larger Q^2-values than estimated by the procedure described in sec. 5.2.2.3.

5.2.2.5 Bose-Einstein correlations: Gaussian or power law

For second order, the differential second-order GHP-integral $DF_2^{GHP}(Q^2)$ is closely related to the function $R(Q^2)$ used in pion-interferometry (see [NA22BE] for application to the NA22 data). The function $R(Q^2)$ differs from $DF_2^{GHP}(Q^2)$ in two ways:

1. The normalization factor: the event mixing occurs only between events belonging to the same multiplicity class in case of pion-interferometry, while no restrictions are made in case of the GHP-integral.
2. The binning: while a linear binning in $\ln Q^2$ is used for the determination of $DF_2^{GHP}(Q^2)$, a linear binning in Q^2 is used in order to determine $R(Q^2)$.

In Fig. 5.13 $DF_2^{GHP}(Q^2)$ is plotted versus Q^2 double logarithmically for different charge combinations. In order to increase statistics, the negatives-only and positives-only samples are combined into the like-charged sample. As in the case of $F_2^{GHP}(Q^2)$, the strongest increase is found for the like-charged sample. A cut for $(M_{inv} - 2m_\pi) \leq 0.002$ GeV does not influence the data shown in Fig. 5.13, since this corresponds to $Q^2 \lesssim 10^{-3}$ GeV^2.

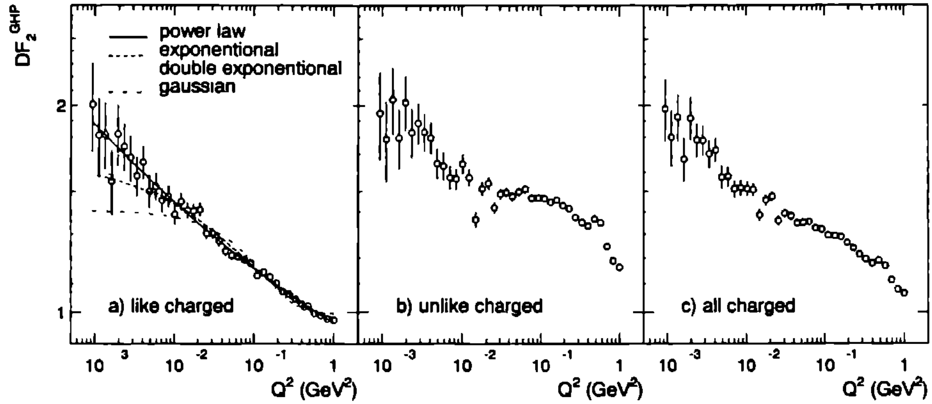

Figure 5.13: *The differential second-order GHP-integral in Q^2 for a) like-charged pairs, b) unlike-charged pairs and c) all-charged pairs.*

In an attempt to understand the role of BE-correlations in the steep rise of DF_2^{GHP} (like charged), the following functions are fitted to the data (see [UA1B92] for a similar analysis of UA1 data):

- power law
$$DF_2^{GHP}\left(Q^2\right) = a + b\left(Q^2\right)^{-\varphi} \quad , \tag{5.27}$$
- exponential
$$DF_2^{GHP}\left(Q^2\right) = a\,(1 + b\exp(-rQ)) \quad , \tag{5.28}$$
- double exponential
$$DF_2^{GHP}\left(Q^2\right) = a\left(1 + 2\lambda\,(1-\lambda)\exp(-rQ) + \lambda^2\exp(-2rQ)\right) \quad , \tag{5.29}$$
- Gaussian
$$DF_2^{GHP}\left(Q^2\right) = a\left(1 + b\exp\left(-Q^2/(2\sigma^2)\right)\right) \quad . \tag{5.30}$$

While the power law (5.27) would lead to intermittency, the exponential and mainly the Gaussian forms correspond to conventional parametrizations of Bose-Einstein correlations.

All fits are superposed on Fig. 5.13a, the values of the fit parameters are collected in Tab. 5.8[2] . The power-law fit gives the best result, but in the region where the distinction can be made the statistical errors are large.

Since a reflection from η'-decay is expected at low Q^2, the FRITIOF2.0 + BE run is done with and without η'-decay (Fig. 5.14). An effect of η' is present around $Q^2 = 10^{-2}$GeV^2, but not at smaller Q^2.

---

[2] The values of the parameters b and r of the exponential fit (5.28) are used to parametrize BE-correlations in FRITIOF2.0 throughout this thesis.

	$a + b\,(Q^2)^{-\varphi}$	
a	0.56 ± 0.09	
b	0.40 ± 0.09	
φ	0.17 ± 0.03	
χ^2/NDF	22.0/36	
	$a\,(1 + b\exp(-rQ))$	
a	0.97 ± 0.01	
b	0.72 ± 0.03	
r	$4.0 \pm 0.3\ (\mathrm{GeV})^{-1}$	0.79 ± 0.05 fm
χ^2/NDF	40.4/36	
	$a\,(1 + 2\lambda(1-\lambda)\exp(-rQ) + \lambda^2\exp(-2rQ))$	
a	0.96 ± 0.01	
λ	0.53 ± 0.03	
r	$3.3 \pm 0.2\ (\mathrm{GeV})^{-1}$	0.65 ± 0.04 fm
χ^2/NDF	35.7/36	
	$a\,(1 + b\exp(-Q^2/(2\sigma^2)))$	
a	0.996 ± 0.005	
b	0.41 ± 0.01	
σ	0.25 ± 0.01	
χ^2/NDF	123/36	

Table 5.8: *Results of fits to the data presented in Fig. 5.13a.*

If the power law is confirmed in the small Q^2-region by future experiments, this is in contradiction to the conventional Gaussian or Bessel-type parametrization of Bose-Einstein correlations. Furthermore, it is important to note that even in the larger Q^2-region ($0.006 < Q^2 < 1\ \mathrm{GeV}^2$) conventional Bose-Einstein parametrization and power law are indistinguishable. So, self-similarity of the correlation function is in fact even there an interpretation alternative to the conventional view of Bose-Einstein correlations (the latter relating the low-Q^2 enhancement to the *static* size of an interaction region).

Going beyond 1 GeV^2 (Fig. 5.15), the scaling law for the like-charged combinations is broken and an indication is seen for an oscillation of DF_2^{GHP} needing further investigation.

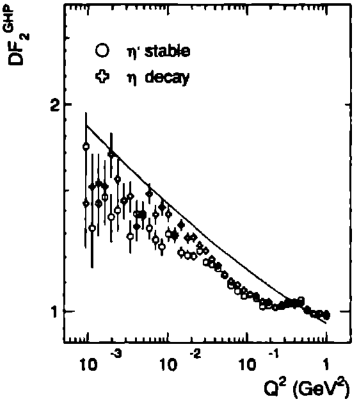

Figure 5.14: *FRITIOF2.0 + BE predictions for $F_2^{GHP}(Q^2)$ for like-charged pairs, with the η'-resonance kept stable (circles) and allowed to decay (crosses), respectively. The full line represents the power-law fit to the data*

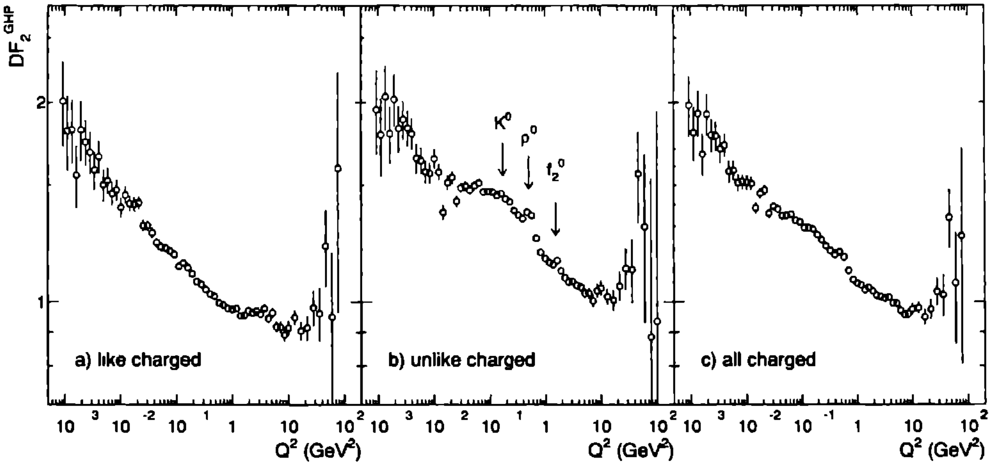

Figure 5.15: *Fig. 5.13 extented to the large Q^2-region.*

5.3 Star integral

5.3.1 Formalism

The mathematical formalism concerning the star integral can be found in [PLHE93b, PLHE94]. However, in these calculations, the authors do not account for event weights, which is unsatisfactory, at least from an experimental point of view. A full derivation is given below.

The condition for a q-tuple to be smaller than δ in the star-topology framework, can be expressed as

$$\prod_{j=2}^{q} \theta(\delta - d_{1,j}) = 1 \quad . \tag{5.31}$$

Whence, for the unnormalized density integral

$$\begin{aligned} \xi_q(\delta) &= \int \ldots \int \rho_q(p_1, \ldots, p_q) \prod_{k=2}^{q} \theta(\delta - d_{1,k}) \prod_{j=1}^{q} \frac{\mathrm{d}^3 p_j}{(2\pi)^3 2E_j} & (5.32)\\ &= \left\langle \sum_{i_1 \neq \cdots \neq i_q}^{n} \prod_{k=2}^{q} \theta(\delta - d_{i_1,i_k}) \right\rangle & (5.33)\\ &= \left\langle \sum_{i_1}^{n} \left(\sum_{i_2 \neq i_1}^{n} \theta(\delta - d_{i_1,i_2}) \right)^{[q-1]} \right\rangle & (5.34)\\ &= \left\langle \sum_{i_1} a^{[q-1]}(i_1) \right\rangle & (5.35) \end{aligned}$$

In the short-hand form (5.35), a is called the sphere count. It represents the number of particles within a sphere of radius δ around central particle i_1, with i_1 itself excluded from the count.

Denoting the weight of event e by w_e and the distance between particle i_k of event e_k and particle i_l of event e_l by $d^{e_k,e_l}_{i_k,i_l}$, one obtains for the normalization factor $\xi^{(\mathrm{n})}_q(\delta)$

$$\begin{aligned} \xi^{(\mathrm{n})}_q(\delta) &= \int \ldots \int \rho_1(p_1) \ldots \rho_1(p_q) \prod_{k=2}^{q} \theta(\delta - d_{1,k}) \prod_{j=1}^{q} \frac{\mathrm{d}^3 p_j}{(2\pi)^3 2E_j} & (5.36)\\ &= \frac{1}{\sum_{e_1} w_{e_1}} \cdots \frac{1}{\sum_{e_q} w_{e_q}} \sum_{e_1} w_{e_1} \sum_{i_1} \cdots \sum_{e_q} w_{e_q} \sum_{i_q} \prod_{k=2}^{q} \theta\left(\delta - d^{e_1,e_k}_{i_1,i_k}\right) & (5.37)\\ &= \frac{1}{\sum_{e_1} w_{e_1}} \sum_{e_1} w_{e_1} \sum_{i_1} \left(\frac{1}{\sum_{e_2} w_{e_2}} \sum_{e_2} w_{e_q} \sum_{i_q} \theta\left(\delta - d^{e_1,e_2}_{i_1,i_2}\right) \right)^{q-1} & (5.38)\\ &= \left\langle \sum_{i_1} \left\langle \sum_{i_2} \theta\left(\delta - d^{e_1,e_2}_{i_1,i_2}\right) \right\rangle^{q-1} \right\rangle & (5.39)\\ &= \left\langle \sum_{i_1} \langle b(i_1) \rangle^{q-1} \right\rangle & (5.40) \end{aligned}$$

Here, the mixed-event sphere count b has been introduced. It equals the number of particles of event e_2 around the central i_1 of event e_1 within distance δ.

However, in going from (5.36) to (5.37), the fact of the finite number of events has been neglected. While $\rho_1(x)$ in (5.36) is a true value, i.e. the value in case of an infinite number of events, the sums in (5.37) run only over a finite number of events. Actually the correct version of (3.42) is

$$\rho_q(p_1,\ldots,p_q) = \mathrm{E}\left[\left\langle \sum_{i_1\neq\ \neq i_q} \delta(p_1-p_{i_1})\ldots\delta(p_q-p_{i_q})\right\rangle\right] \quad , \tag{5.41}$$

where E[x] denotes the expectation value of x. Clearly,

$$\rho_1(p_1)\ldots\rho_1(p_q) \;=\; \mathrm{E}\left[\left\langle\sum_{i_1}\delta(p_1-p_{i_1})\right\rangle\right]\ldots\mathrm{E}\left[\left\langle\sum_{i_q}\delta(p_1-p_{i_q})\right\rangle\right] \tag{5.42}$$

$$\neq\; \mathrm{E}\left[\left\langle\sum_{i_1}\delta(p_1-p_{i_1})\right\rangle\ldots\left\langle\sum_{i_q}\delta(p_q-p_{i_q})\right\rangle\right] \tag{5.43}$$

As will be shown below for $q = 2$, the estimator in the r.h.s. of (5.43) is biased. First define the average event weight $\langle w\rangle_N$ for the full sample of N events

$$\langle w\rangle_N = \frac{1}{\sum_{e=1}^N w_e}\sum_{e=1}^{N} w_e \qquad \text{and} \qquad \sum_{e=1}^{N} w_e = N\langle w\rangle_N \quad . \tag{5.44}$$

For not too small a subsample of N' events, one has approximately

$$\sum_{e=1}^{N'} w_e = N'\langle w\rangle_N \quad . \tag{5.45}$$

Eq. (5.43) can be written as

$$\begin{aligned}
&\mathrm{E}\left[\left\langle\sum_{i_1}\delta(p_1-p_{i_1})\right\rangle\left\langle\sum_{i_2}\delta(p_2-p_{i_2})\right\rangle\right]\\
&= \mathrm{E}\left[\left(\frac{1}{N\langle w\rangle_N}\sum_{e_1}w_{e_1}\sum_{i_1}\delta(p_1-p_{i_1})\right)\left(\frac{1}{N\langle w\rangle_N}\sum_{e_2}w_{e_2}\sum_{i_2}\delta(p_2-p_{i_2})\right)\right]\\
&= \mathrm{E}\left[\frac{1}{N^2\langle w\rangle_N^2}\sum_{e_1\neq e_2}w_{e_1}w_{e_2}\sum_{i_1,i_2}\delta(p_1-p_{i_1})\delta(p_2-p_{i_2})\right]\\
&\quad +\mathrm{E}\left[\frac{1}{N^2\langle w\rangle_N^2}\sum_{e_1}w_{e_1}^2\sum_{i_1,i_2}\delta(p_1-p_{i_1})\delta(p_2-p_{i_2})\right]\\
&= \frac{N-1}{N}\rho_1(p_1)\rho_1(p_2)+\frac{1}{N}\mathrm{E}\left[\left\langle\frac{w_e}{\langle w\rangle_N}\sum_{i_1,i_2}\delta(p_1-p_{i_1})\delta(p_2-p_{i_2})\right\rangle\right]
\end{aligned} \tag{5.46}$$

Whence, for $N \to \infty$

$$\rho_1(p_1)\rho_1(p_2) = \mathrm{E}\left[\left\langle\sum_{i_1}\delta(p_1-p_{i_1})\right\rangle\left\langle\sum_{i_2}\delta(p_2-p_{i_2})\right\rangle\right] \quad , \tag{5.47}$$

and for finite N

$$\rho_1(p_1)\rho_1(p_2) = \mathrm{E}\left[\frac{1}{N(N-1)\langle w\rangle_N^2}\sum_{e_1\neq e_2} w_{e_1}w_{e_2}\sum_{i_1,i_2}\delta(p_1-p_{i_1})\delta(p_2-p_{i_2})\right] \tag{5.48}$$

Generally,

$$\rho_1(p_1)\dots\rho_1(p_q) = \mathrm{E}\left[\frac{1}{N^{[q]}\langle w\rangle_N^q}\sum_{e_1\neq\dots\neq e_q} w_{e_1}\dots w_{e_q}\sum_{i_1,\dots,i_q}\delta(p_1-p_{i_1})\dots\delta(p_q-p_{i_q})\right] \quad , \tag{5.49}$$

i.e. the sums run only over different events.

To estimate experimentally $\rho_1(p_1)\dots\rho_q(p_q)$, intuition suggests to compose q-tuples from tracks in different events, thus automaticly excluding correlations. Expression (5.49) demonstrates that this is indeed the correct way to proceed. It furthermore proves that the normalization used for the GHP-integral (Sect. 5.2) indeed leads to unbiased estimates. Note, however, that the normalization $\langle n_m\rangle^q$ of the factorial moments and the factorial cumulant moments *are* biased:

$$\begin{aligned}\int_{\Omega_m^q}\rho_1(p_1)\dots\rho_1(p_q)\prod_{j=1}^{q}\frac{\mathrm{d}^3p_j}{(2\pi)^3 2E_j} &= \mathrm{E}\left[\frac{1}{N^{[q]}\langle w\rangle_N^q}\sum_{e_1\neq\dots\neq e_q} w_{e_1}\dots w_{e_q}\right] n_m^{(e_1)}\dots n_m^{(e_q)} && (5.50)\\ &\neq \langle n_m\rangle^q \quad ; && (5.51)\end{aligned}$$

except for N going to infinity.

In the star topology, the unbiased normalization factor $\xi_q^{(\mathrm{n})}$ is experimentally dertermined as

$$\begin{aligned}\xi_q^{(\mathrm{n})} &= \frac{1}{N\langle w\rangle_N}\sum_{e_1} w_{e_1}\sum_{i_1}\left(\frac{N}{N^{[q]}\langle w\rangle_N^{q-1}}\underbrace{\sum_{e_2\neq\cdot\neq e_q}}_{\neq e_1} w_{e_2}\dots w_{e_q}\sum_{i_2,\dots,i_q}\prod_{k=2}^{q}\theta\left(\delta-d_{i_1,i_k}^{e_1,e_k}\right)\right) && (5.52)\\ &= \left\langle\sum_{i_1}\hat{\xi}_q^{(\mathrm{n})}(i_1)\right\rangle \quad . && (5.53)\end{aligned}$$

In order to obtain more compact expressions for $\xi_q^{(\mathrm{n})}$, the following notations are introduced

$$\hat{n}^{12} = \sum_{i_2}\theta\left(\delta-d_{i_1,i_2}^{e_1,e_2}\right) \tag{5.54}$$

and

$$\langle x\rangle_{W_M^q} = \frac{1}{\left(\sum_{e=1}^{M} w_e\right)^q}\sum_{e=1}^{M} x w_e^q \quad . \tag{5.55}$$

In this notation, the unnormalized density integral and the normalization factor become

$$\xi_q = \left\langle\sum_{i_1} a^{[q-1]}(i_1)\right\rangle_{W_N} \qquad \text{and} \qquad \xi_q^{(\mathrm{n})} = \left\langle\sum_{i_1}\hat{\xi}_q^{(\mathrm{n})}(i_1)\right\rangle_{W_N} \quad , \tag{5.56}$$

respectively. In the following it is assumed that no event ever equals e_1, except when mentioned explicitly. For $q = 2$, one obtains

$$\begin{aligned}
\hat{\xi}_2^{(\mathrm{n})}(i_1) &= \frac{1}{(N-1)\,\langle w \rangle_N} \sum_{e_2} w_{e_2} \hat{n}^{12} && (5.57)\\
&= \langle b(i_1) \rangle_{W_{N-1}} \quad , && (5.58)
\end{aligned}$$

and for $q = 3$

$$\begin{aligned}
\hat{\xi}_3^{(\mathrm{n})}(i_1) &= \frac{1}{(N-1)(N-2)\,\langle w \rangle_N} \sum_{e_2 \neq e_3} w_{e_2} w_{e_3} \hat{n}^{12} \hat{n}^{13} && (5.59)\\
&= \frac{N-1}{N-2} \left(\frac{1}{(N-1)^2 \langle w \rangle_N^2} \left(\sum_{e_2} w_{e_2} \hat{n}^{12} \right)^2 - \frac{1}{(N-1)^2 \langle w \rangle_N^2} \sum_{e_2} \left(w_{e_2} \hat{n}^{12} \right)^2 \right) \\
&= \frac{N-1}{N-2} \left(\langle b(i_1) \rangle_{W_{N-1}}^2 - \left\langle b^2(i_1) \right\rangle_{W_{N-1}^2} \right) \quad . && (5.60)
\end{aligned}$$

Higher orders can be derived in an analogous manner. For $q = 4$ and $q = 5$ one obtains in a slightly modified notation

$$\begin{aligned}
\hat{\xi}_4^{(\mathrm{n})} &= \frac{(N-1)^2}{(N-2)(N-3)} \left(\langle b \rangle_{W_{N-1}}^3 - 3 \left\langle b^2 \right\rangle_{W_{N-1}^2} \langle b \rangle_{W_{N-1}} + 2 \left\langle b^3 \right\rangle_{W_{N-1}^3} \right) && (5.61)\\
\hat{\xi}_5^{(\mathrm{n})} &= \frac{(N-1)^3}{(N-2)(N-3)(N-4)} \left(\langle b \rangle_{W_{N-1}}^4 - 6 \left\langle b^2 \right\rangle_{W_{N-1}^2} \langle b \rangle_{W_{N-1}}^2 \right. \\
&\quad \left. +8 \left\langle b^3 \right\rangle_{W_{N-1}^3} \langle b \rangle_{W_{N-1}} + 3 \left\langle b^2 \right\rangle_{W_{N-1}^2}^2 - 6 \left\langle b^4 \right\rangle_{W_{N-1}^4} \right) && (5.62)
\end{aligned}$$

Now, the necessary formulae have been gathered to allow an unbiased determination of the unnormalized cumulants. For second order one has

$$\begin{aligned}
\zeta_2(\delta) &= \iint C_2(p_1, p_2) \theta(\delta - d_{1,2}) \frac{\mathrm{d}^3 p_1}{(2\pi)^3 2E_1} \frac{\mathrm{d}^3 p_2}{(2\pi)^3 2E_2} \\
&= \iint \rho_2(p_1, p_2) \theta(\delta - d_{1,2}) \frac{\mathrm{d}^3 p_1}{(2\pi)^3 2E_1} \frac{\mathrm{d}^3 p_2}{(2\pi)^3 2E_2} \\
&\quad + \iint \rho_1(p_1) \rho_1(p_2) \theta(\delta - d_{1,2}) \frac{\mathrm{d}^3 p_1}{(2\pi)^3 2E_1} \frac{\mathrm{d}^3 p_2}{(2\pi)^3 2E_2} \\
&= \left\langle \sum_{i_1} a(i_1) \right\rangle_{W_N} - \left\langle \sum_{i_1} \hat{\xi}_2^{(\mathrm{n})}(i_1) \right\rangle_{W_N} \\
&= \left\langle \sum_{i_1} \left(a(i_1) - \hat{\xi}_2^{(\mathrm{n})}(i_1) \right) \right\rangle_{W_N} && (5.63)
\end{aligned}$$

For third order the situation is a little more complex. However, one obtains straightforwardly

$$\begin{aligned}
\zeta_3(\delta) &= \iint C_3(p_1,p_2,p_3)\theta(\delta-d_{1,2})\,\theta(\delta-d_{1,3})\prod_{j=1}^{3}\frac{\mathrm{d}^3p_j}{(2\pi)^3 2E_j} \\
&= \iint \rho_3(p_1,p_2,p_3)\theta(\delta-d_{1,2})\,\theta(\delta-d_{1,3})\prod_{j=1}^{3}\frac{\mathrm{d}^3p_j}{(2\pi)^3 2E_j} \\
&\quad -2\iint \rho_2(p_1,p_2)\rho_1(p_3)\theta(\delta-d_{1,2})\,\theta(\delta-d_{1,3})\prod_{j=1}^{3}\frac{\mathrm{d}^3p_j}{(2\pi)^3 2E_j} \\
&\quad -\iint \rho_1(p_1)\rho_2(p_2,p_3)\theta(\delta-d_{1,2})\,\theta(\delta-d_{1,3})\prod_{j=1}^{3}\frac{\mathrm{d}^3p_j}{(2\pi)^3 2E_j} \\
&\quad +2\iint \rho_1(p_1)\rho_1(p_2)\rho_1(p_3)\theta(\delta-d_{1,2})\,\theta(\delta-d_{1,3})\prod_{j=1}^{3}\frac{\mathrm{d}^3p_j}{(2\pi)^3 2E_j} \\
&= \left\langle\sum_{i_1} a^{[2]}(i_1)\right\rangle_{W_N} - 2\frac{1}{N^{[2]}\left\langle w\right\rangle_N^2}\sum_{e_1\neq e_2}\sum_{i_1,i_2}\sum_{i_3}\theta\Big(\delta-d^{e_1,e_1}_{i_1,i_2}\Big)\,\theta\Big(\delta-d^{e_1,e_2}_{i_1,i_3}\Big) \\
&\quad -\frac{1}{N^{[2]}\left\langle w\right\rangle_N^2}\sum_{e_1\neq e_2}\sum_{i_1}\sum_{i_2\neq i_3}\theta\Big(\delta-d^{e_1,e_2}_{i_1,i_2}\Big)\,\theta\Big(\delta-d^{e_1,e_2}_{i_1,i_3}\Big) + 2\left\langle\sum_{i_1}\hat{\xi}_3^{(\mathrm{n})}(i_1)\right\rangle_{W_N} \\
&= \left\langle\sum_{i_1}\left(a^{[2]}(i_1) - 2a(i_1)\hat{\xi}_2^{(\mathrm{n})} - \left\langle b^{[2]}(i_1)\right\rangle_{W_{N-1}} + 2\hat{\xi}_3^{(\mathrm{n})}(i_1)\right)\right\rangle_{W_N}
\end{aligned} \tag{5.64}$$

Generally

$$\zeta_q = \left\langle\sum_{i_1}\hat{\zeta}_q(i_1)\right\rangle_{W_N} \quad , \tag{5.65}$$

where, for $q = 2, \ldots, 5$, the $\hat{\zeta}_q$ are given by (the indication (i_1) is omitted)

$$\hat{\zeta}_2 = a - \hat{\xi}_2^{(\mathrm{n})} \tag{5.66}$$

$$\hat{\zeta}_3 = a^{[2]} - \left\langle b^{[2]}\right\rangle_{W_{N-1}} - 2a\hat{\xi}_2^{(\mathrm{n})} + 2\hat{\xi}_3^{(\mathrm{n})} \tag{5.67}$$

$$\begin{aligned}
\hat{\zeta}_4 &= a^{[3]} - \left\langle b^{[3]}\right\rangle_{W_{N-1}} - 3a\left\langle b^{[2]}\right\rangle_{W_{N-1}} - 3a^{[2]}\hat{\xi}_2^{(\mathrm{n})} + 6a\hat{\xi}_3^{(\mathrm{n})} - 6\hat{\xi}_4^{(\mathrm{n})} \\
&\quad +\frac{6(N-1)}{N-2}\left(\left\langle b\right\rangle_{W_{N-1}}\left\langle b^{[2]}\right\rangle_{W_{N-1}} - \left\langle bb^{[2]}\right\rangle_{W_{N-1}^2}\right)
\end{aligned} \tag{5.68}$$

$$\begin{aligned}
\hat{\zeta}_5 &= a^{[4]} - 4a^{[3]}\hat{\xi}_2^{(\mathrm{n})} - 6a^{[2]}\left\langle b^{[2]}\right\rangle_{W_{N-1}} - 4a\left\langle b^{[3]}\right\rangle_{W_{N-1}} - \left\langle b^{[4]}\right\rangle_{W_{N-1}} + 12a^{[2]}\hat{\xi}_3^{(\mathrm{n})} \\
&\quad -24a\hat{\xi}_4^{(\mathrm{n})} + 24\hat{\xi}_5^{(\mathrm{n})} + \frac{6(N-1)}{N-2}\left(\left\langle b^{[2]}\right\rangle_{W_{N-1}}^2 - \left\langle b^{[2]}b^{[2]}\right\rangle_{W_{N-1}^2}\right) \\
&\quad +\frac{8(N-1)}{N-2}\left(\left\langle b\right\rangle_{W_{N-1}}\left\langle b^{[3]}\right\rangle_{W_{N-1}} - \left\langle bb^{[3]}\right\rangle_{W_{N-1}^2}\right) \\
&\quad +\frac{24a(N-1)}{N-2}\left(\left\langle b^{[2]}\right\rangle_{W_{N-1}} - \left\langle b\right\rangle_{W_{N-1}} - \left\langle bb^{[2]}\right\rangle_{W_{N-1}^2}\right) \\
&\quad -\frac{36(N-1)^2}{(N-2)(N-3)}\left(\left\langle b\right\rangle_{W_{N-1}}^2 - \left\langle b^{[2]}\right\rangle_{W_{N-1}} - \left\langle b^2\right\rangle_{W_{N-1}^2}\left\langle b^{[2]}\right\rangle_{W_{N-1}}\right. \\
&\quad \left. -2\left\langle b\right\rangle_{W_{N-1}}\left\langle bb^{[2]}\right\rangle_{W_{N-1}^2} + 2\left\langle b^2b^{[2]}\right\rangle_{W_{N-1}^3}\right) \quad .
\end{aligned} \tag{5.69}$$

5.3.2 Experimental results

5.3.2.1 Size of the subsample

Ideally, $\hat{\xi}_q^{(n)}$ and $\hat{\zeta}_q$ (defined via (5.56) and (5.65), respectively) should be determined from a subsample consisting of the $N' = N - 1$ events different from event e_1 considered in the main event loop. In practice, however, this demands far to much computing time. Therefore, a smaller subsample of size N' large enough to obtain results independent of N', has to be used.

In the above derivation of the star formulae, it was necessary to make the approximation (5.45). This implies a second restriction on the minimum number of events N' to be used in the second event loop.

In order to determine a reasonable value for N', two tests are performed. Firstly, a window of N' events has been shifted through the full sample and a distribution of $\langle w \rangle_{N'}$ is made[3]. For $N' = 1, 25, 100$ and 200, this distribution is shown in Fig. 5.16. The RMS for the obtained distributions is denoted on the figure. Relative to the mean value, RMS = 8.2%, 4.7%, 3.7% for $N' = 25, 100, 200$, respectively.

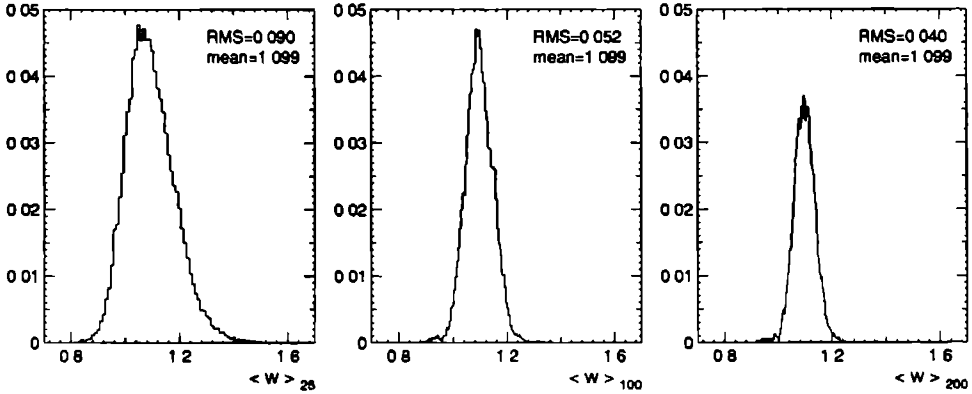

Figure 5.16: *The distribution of* $\langle w \rangle_{N'}$ *for different values of* N'.

A second check consists of testing the relations between $F_q^*(Q^2)$ and $K_q^*(Q^2)$ that hold for $Q^2 \to \infty$. These relations, as obtained from 3.47, are

$$\begin{aligned}
K_2^* &= F_2^* - 1\\
K_3^* &= F_3^* - 3F_2^* + 2\\
K_4^* &= F_4^* - 4F_3^* - 3\,(F_2^*)^2 + 2F_2^* - 6\\
K_5^* &= F_5^* - 5F_4^* - 10F_2^*F_3^* + 20F_3^* + 30\,(F_2^*)^2 - 15F_2^* + 24 \quad . \qquad (5.70)
\end{aligned}$$

In Tab. 5.9 K_q^* obtained directly from the data is compared with the values obtained via formulae (5.70) (denoted $K_q^*(F_q^*)$) for $Q^2 \to \infty$. The agreement improves when N' is increased[4].

---

[3] $\langle\ \rangle_{N'}$ denotes an unweighted average over N' events

[4] It has been tested that if no event weights are used, relations 5.70 are already fullfiled for $N' = 25$.

Together with the results the previous test, Tab. 5.9 suggests that $N' = 200$ will be sufficiently large to obtain reliable results.

	$N' = 25$		$N' = 100$		$N' = 200$	
order	K_q^*	$K_q^*(F_q^*)$	K_q^*	$K_q^*(F_q^*)$	K_q^*	$K_q^*(F_q^*)$
2	0.185 ± 0.006	0.185	0.180 ± 0.006	0.180	0.180 ± 0.006	0.180
3	-0.011 ± 0.008	0.041	0.010 ± 0.007	0.022	0.015 ± 0.007	0.019
4	-0.009 ± 0.011	0.002	-0.007 ± 0.009	-0.005	-0.004 ± 0.009	-0.006
5	-0.017 ± 0.022	-0.011	-0.017 ± 0.011	-0.010	-0.010 ± 0.011	-0.010

Table 5.9: *Comparison of K_q^* and $K_q^*(F_q^*)$ for $Q^2 \to \infty$ at different N' values.*

5.3.2.2 Star integrals in terms of Q^2 and M_{inv}^2

In this section preliminary results on the star integral are presented. For second order the GHP-topology and the star topology are the same. However, approximations, inherent to the different approaches in the determination of the normalization factor, lead to small differences between F_2^{GHP} and F_2^*. If in the case of the GHP-integral the multiplicity distribution of the mixed events would be an exact Poissonian and if in the case of the star integral the subsample would be of size $N' = N - 1$, these differences would be zero.

From the derivation in Sect. 5.3.1 it is clear that for the application of the star formalism one only has to count pairs. This number is the input for the calculation of the higher orders. As a consequence, only pair-wise characteristics can be considered. The particles of a pair can have either the same charge or the opposite charge. For higher orders this results in a central particle surrounded by particles carrying the same or the opposite charge of the central particle, respectively. The pair-wise distances considered in this section are

i) the four-momentum difference squared

$$Q^2 = (p_1 - p_2)^2 \quad , \tag{5.71}$$

ii) the invariant mass squared of the pair[5]

$$M_{inv}^2 = (p_1 + p_2)^2 \quad . \tag{5.72}$$

In Figs. 5.17 and 5.18 $\ln F_q^*$ is plotted versus $-\ln Q^2$ and $-\ln M_{inv}^2$, respectively; for various orders and charge combinations. Compared to Fig. 5.17, the large Q^2-values are stretched and the small Q^2-values are compressed in Fig. 5.18. The NA22 data are represented by the black bullets.

The increase of $\ln F_2^*$ for all-charged combinations below $-\ln Q^2 = 5$ ($-\ln M_{inv}^2 = 2.4$) is mainly due to the steep rise of $\ln F_2^*$ for like-charged (positives only and negatives only) combinations. Above $-\ln Q^2 = 5$ ($-\ln M_{inv}^2 = 2.4$) the unlike-charged combinations are

---

[5] Note that for $q \geq 3$ the size of a q-tuple is *not equal* to the invariant mass squared of the q-tuple.

contaminated by Dalitz misidentification and undetected γ-conversions. Applying a cut on the unlike-charged pairs, according to the procedure described in Sect. 5.2.2.3, yields smaller values of F_2^* in the small Q^2 (M_{inv}^2) region (open stars in Figs. 5.17 and 5.18). For higher orders, data with and without cut are the same within errors (not shown). The difference between like-charged combinations and unlike-charged combinations ($-$ around $+$ and $+$ around $-$) diminishes for higher orders: the correlations between like charged particles becomes more dominating.

The data are compared with the predictions of FRITIOF2.0 + BE and FRITIOF2.0 + BE + a bias accounting for Dalitz decay and undetected γ-conversions (only for $q = 2$ and 3). Except for some minor differences, the second-order star integrals for like-charged combinations are well described by FRITIOF2.0 + BE. However, for higher orders the predicted increase of F_q^* is too strong. In case of F_2^* for the unlike-charged combinations, Dalitz decay and γ-conversions are clearly needed to reproduce the increase of the data for $-\ln Q^2 \geq 5$ ($-\ln M_{inv}^2 \geq 2.4$). Applying the cut described in Sect. 5.2.2.3 yiels approximately the same results for FRITIOF2.0 + BE + bias as for the data. The values predicted by FRITIOF2.0 + BE without bias are not reached. Note, however, that in the region $2.4 \leq -\ln Q^2 \leq 5.$ ($1.5 \leq -\ln M_{inv}^2 \leq 2.4$), FRITIOF2.0 + BE + bias overestimates $F_2^*(+-)$, suggesting that the mass distribution used to implement the bias into the model is too wide. For orders $q \geq 4$, FRITIOF2.0 + BE with and without bias coincide within errors (not shown).

The smooth curves with the small error bars on Figs. 5.17 and 5.18 are, however, somewhat misleading. The data points for different Q^2 (M_{inv}^2) values are fully correlated. A cleaner analysis is the study of the differential star integrals. These are shown in Figs. 5.19 and 5.20 in terms of Q^2 and M_{inv}^2, respectively. The data points do not form smooth curves anymore and the errors have increased, especially at small Q^2 and M_{inv}^2 values. There is still a clear dependence on the charge combination. In the $\ln DF_2^*$ vs. $-\ln M_{inv}^2$ plot for unlike-charged combinations, a strong peak due to the ρ-resonance shows up. A cut to remove the influence of undetected Dalitz pairs and γ-conversions is not shown, because it acts on $\ln DF_q^*$ for Q^2 (M_{inv}^2) values smaller than investigated here. The FRITIOF2.0 + BE is in surprising agreement with the data.

It has already been pointed out that the density functions contain contributions from lower-order correlations. The correlation functions are much better suited for a proper analysis of the genuine q-particle correlations. Integrals over these correlation functions in the form of normalized factorial cummulants suffer, unfortunately, from statistical problems. In the star integral formalism, however, one makes optimal use of the available statistics.

The star integral cumulants as function of Q^2 and M_{inv}^2 are presented in Figs. 5.21 and 5.22, respectively. Genuine higher-order correlations can now be established for all charged particles up to order five. For reasons of statistics the negatives-only and positives-only q-tuples and the $-$ around $+$ and $+$ around $-$ q-tuples are for fourth order combined to like-charged combinations and unlike-charged combinations, respectively. The second-order star integrals for $++$ and $--$ pairs follow approximately a power law as function of Q^2. For higher orders one observes a downward curvature. Furthermore, $K_{q\geq3}^*$ sometimes takes negative values, most often at large Q^2 (M_{inv}^2) values. It is obvious that these cannot be plotted on a double logarithmic plot as Figs. 5.21 and 5.22.

The small differences between the data and FRITIOF2.0 + BE seen for F_2^* at large Q^2 (M_{inv}^2) values are enlarged for K_2^*, most strikingly for the positively-charged pairs. For higher orders, FRITIOF predicts the star integral cummulants to curve upwards, while the data

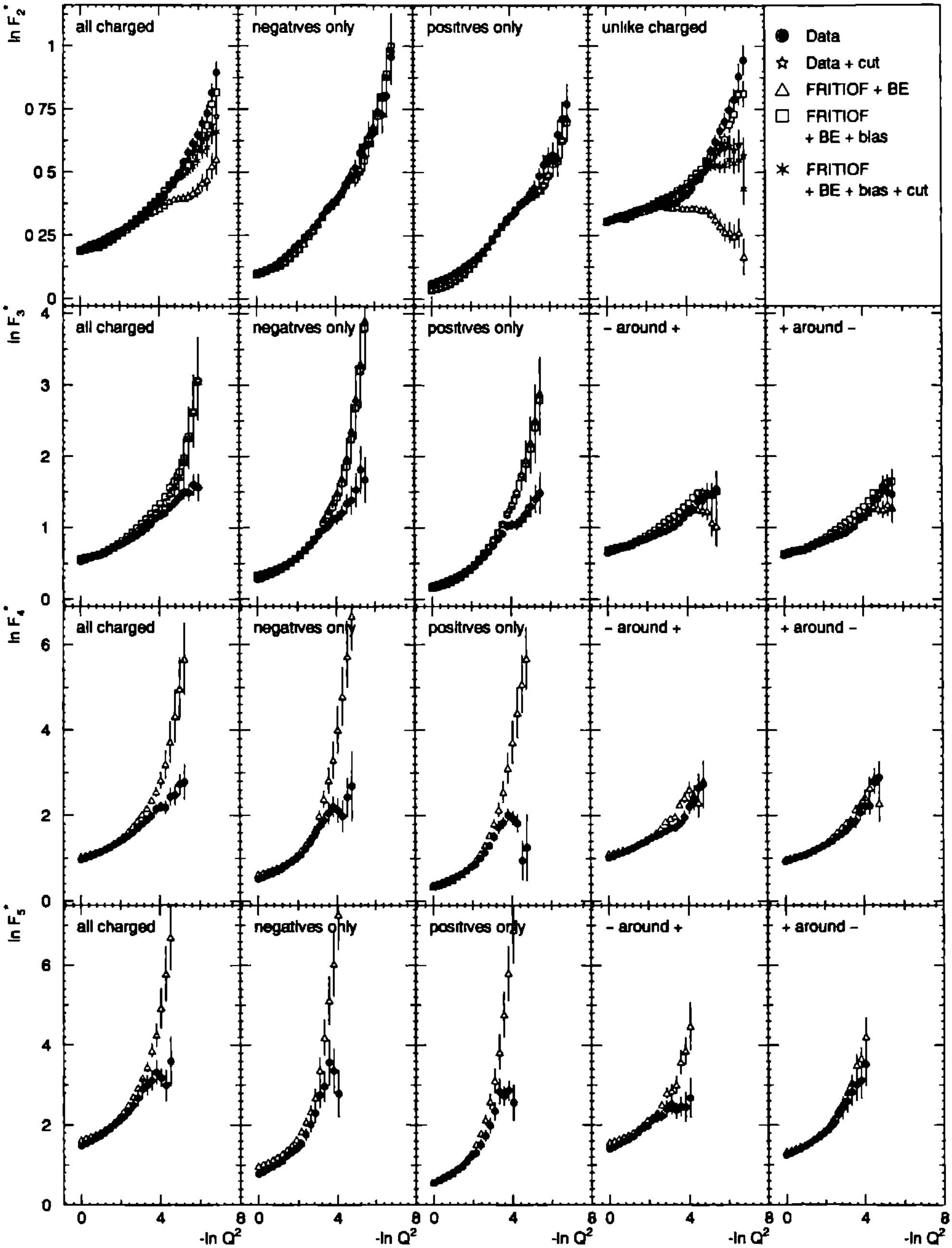

Figure 5.17: *The star integral in terms of Q^2 compared with FRITIOF2.0 + BE and FRITIOF2.0 + BE + a bias accounting for Dalitz decay and undetected γ- conversions (for $q \leq 3$). For $q = 2$ results obtained with a cut, according to the procedure described in Sect. 5.2.2.3, are included.*

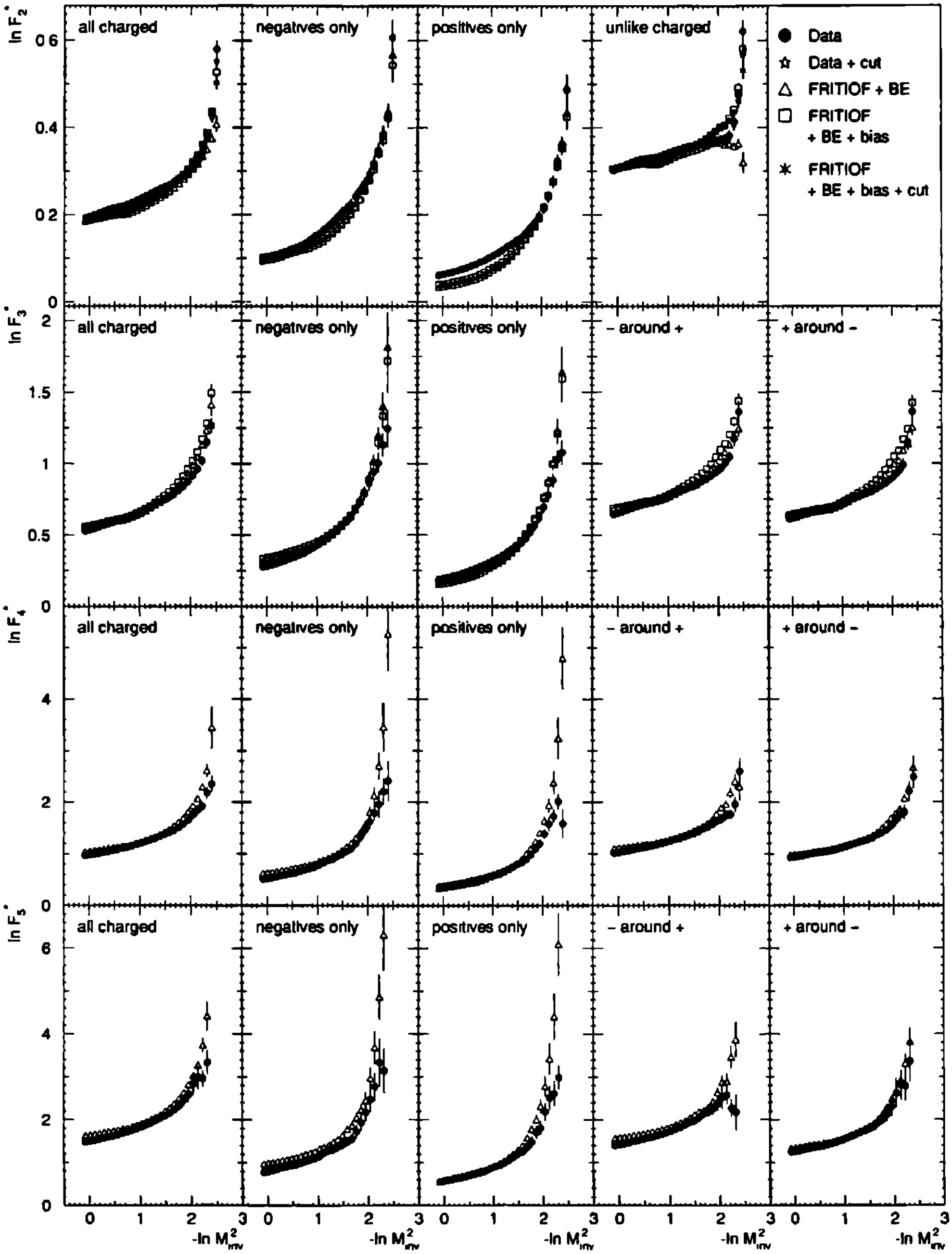

Figure 5.18: *The star integral in terms of* M^2_{inv} *compared with FRITIOF2.0 + BE and FRITIOF2.0 + BE + a bias accounting for Dalitz decay and undetected* γ*-conversions (for* $q \leq 3$*). For* $q = 2$ *results obtained with a cut, according to the procedure described in Sect. 5.2.2.3, are included.*

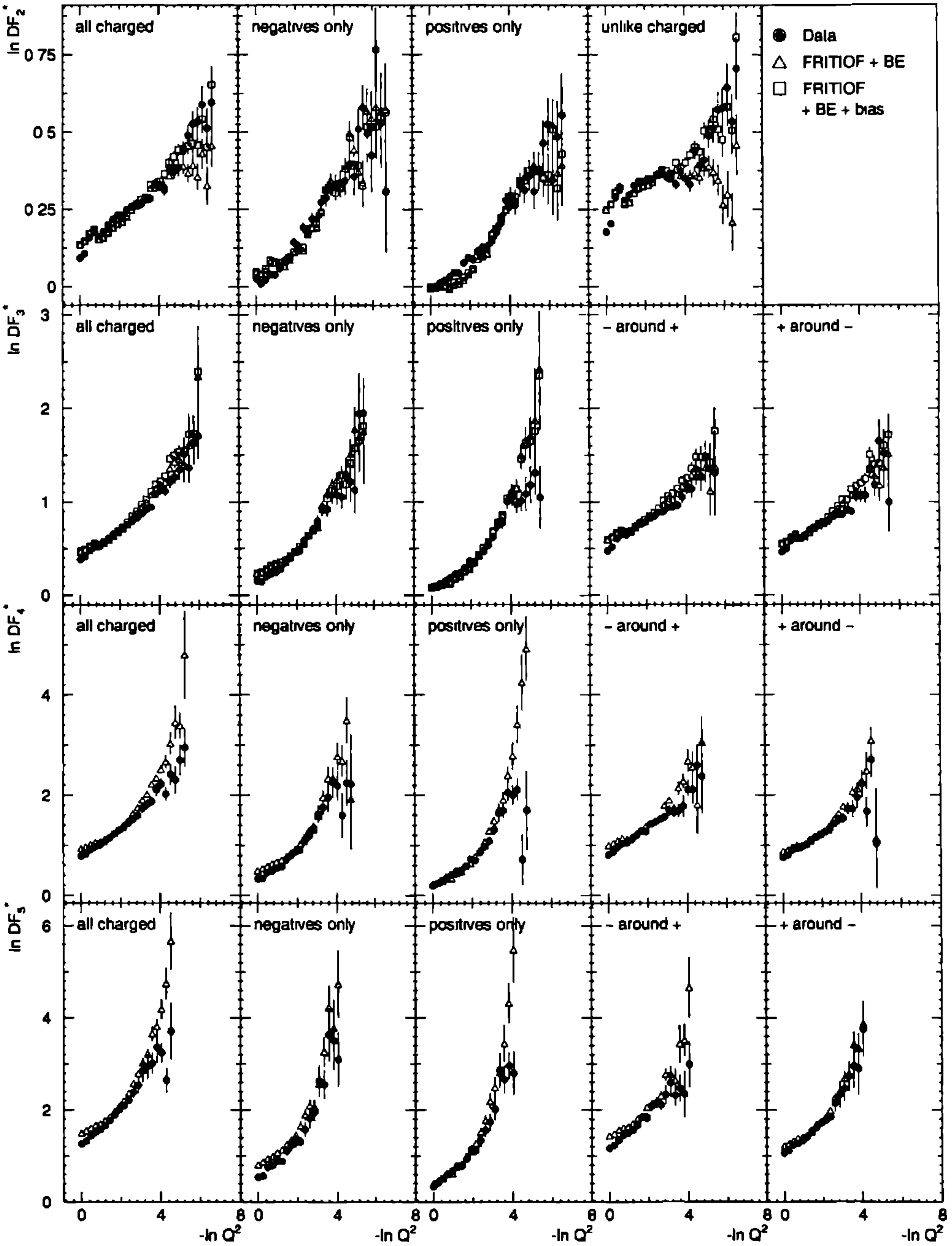

Figure 5.19: *The differential star integral in terms of Q^2 compared with FRITIOF2.0 + BE and FRITIOF2.0 + BE + a bias accounting for Dalitz decay and undetected γ-conversions (for $q \leq 3$).*

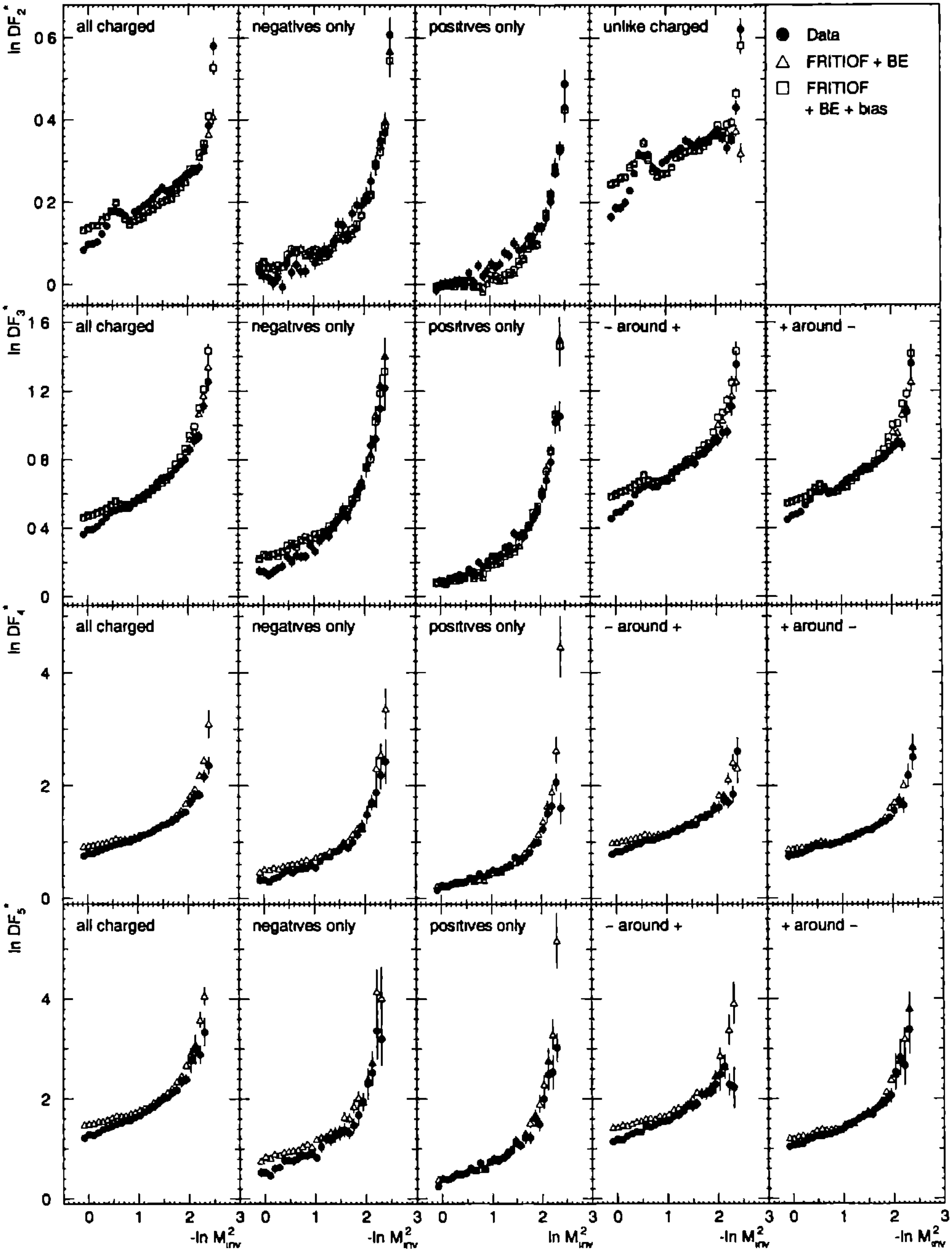

Figure 5.20: *The differential star integral in terms of* M_{inv}^2 *compared with FRITIOF2.0 + BE and FRITIOF2.0 + BE + a bias accounting for Dalitz decay and undetected* γ*-conversions (for* $q \leq 3$*).*

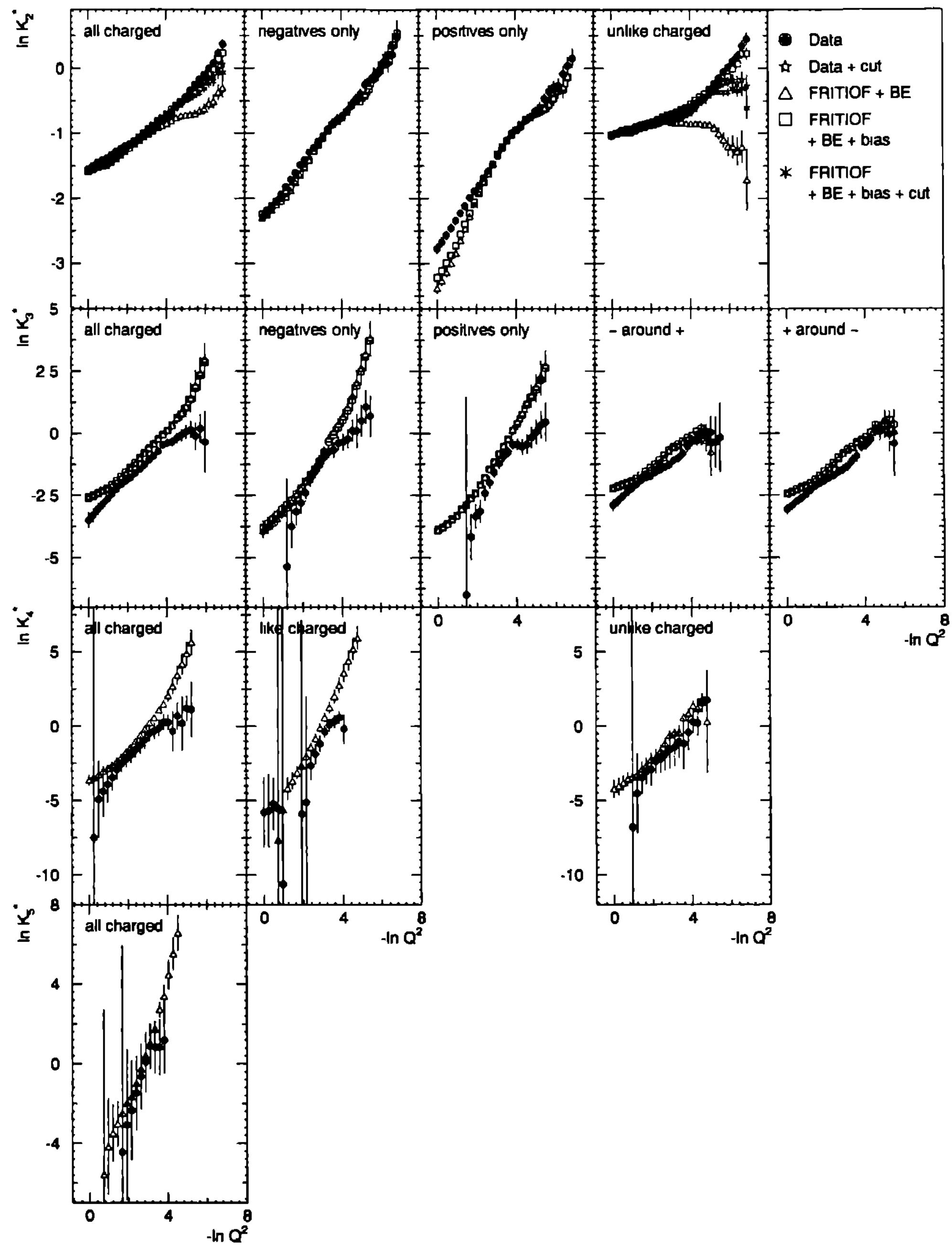

Figure 5.21: *The star integral cumulants in terms of Q^2 compared with FRITIOF2.0 + BE and FRITIOF2.0 + BE + a bias accounting for Dalitz decay and undetected γ-conversions (for $q \leq 3$). For $q = 2$ results obtained with a cut, according to the procedure described in Sect. 5.2.2.3, are included.*

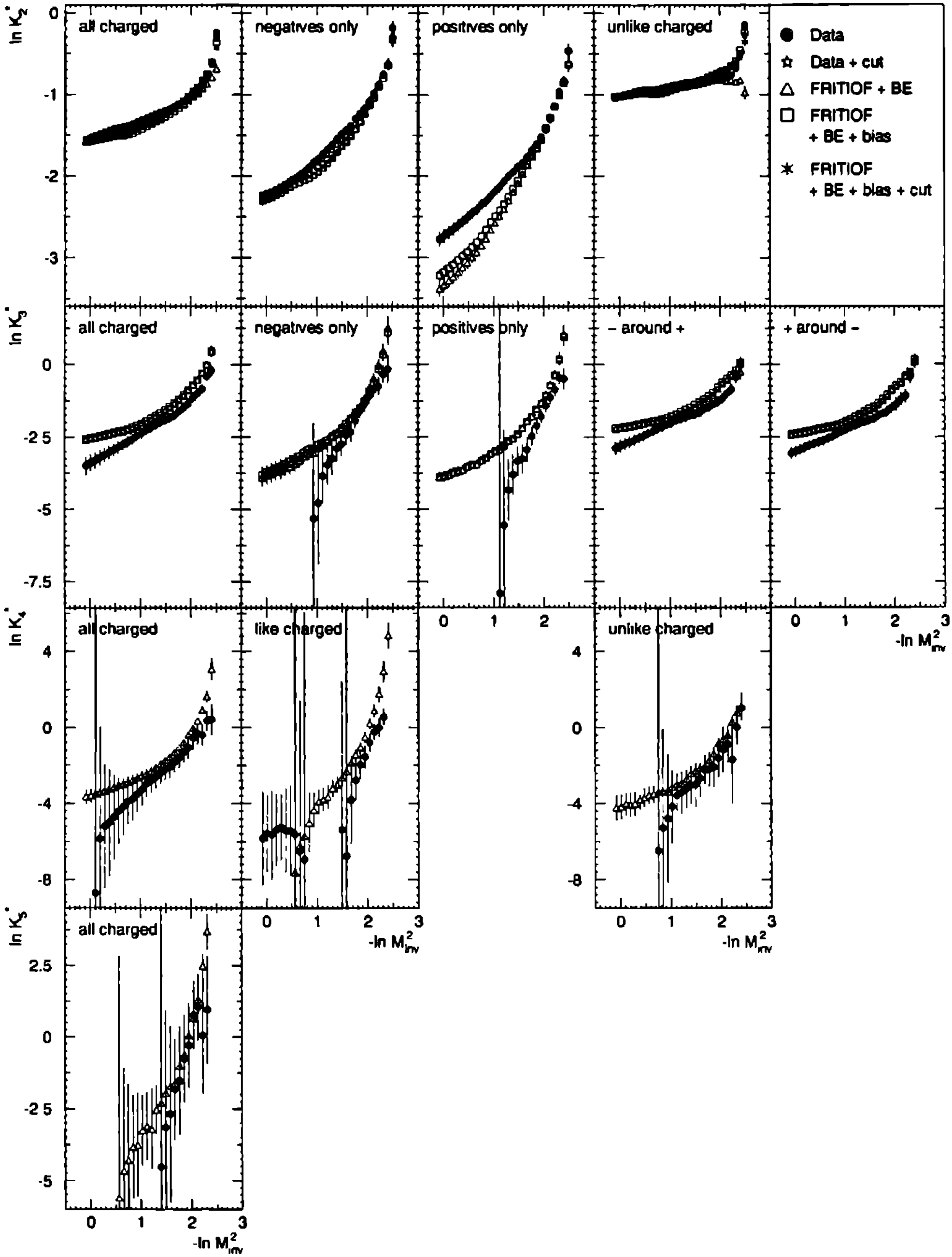

Figure 5.22: *The star integral cumulants in terms of* M_{inv}^2 *compared with FRITIOF2.0 + BE and with FRITIOF2.0 + BE + a bias accounting for Dalitz decay and undetected* γ*-conversions (for* $q \leq 3$*). For* $q = 2$ *results obtained with a cut, according to the procedure described in Sect. 5.2.2.3, are included.*

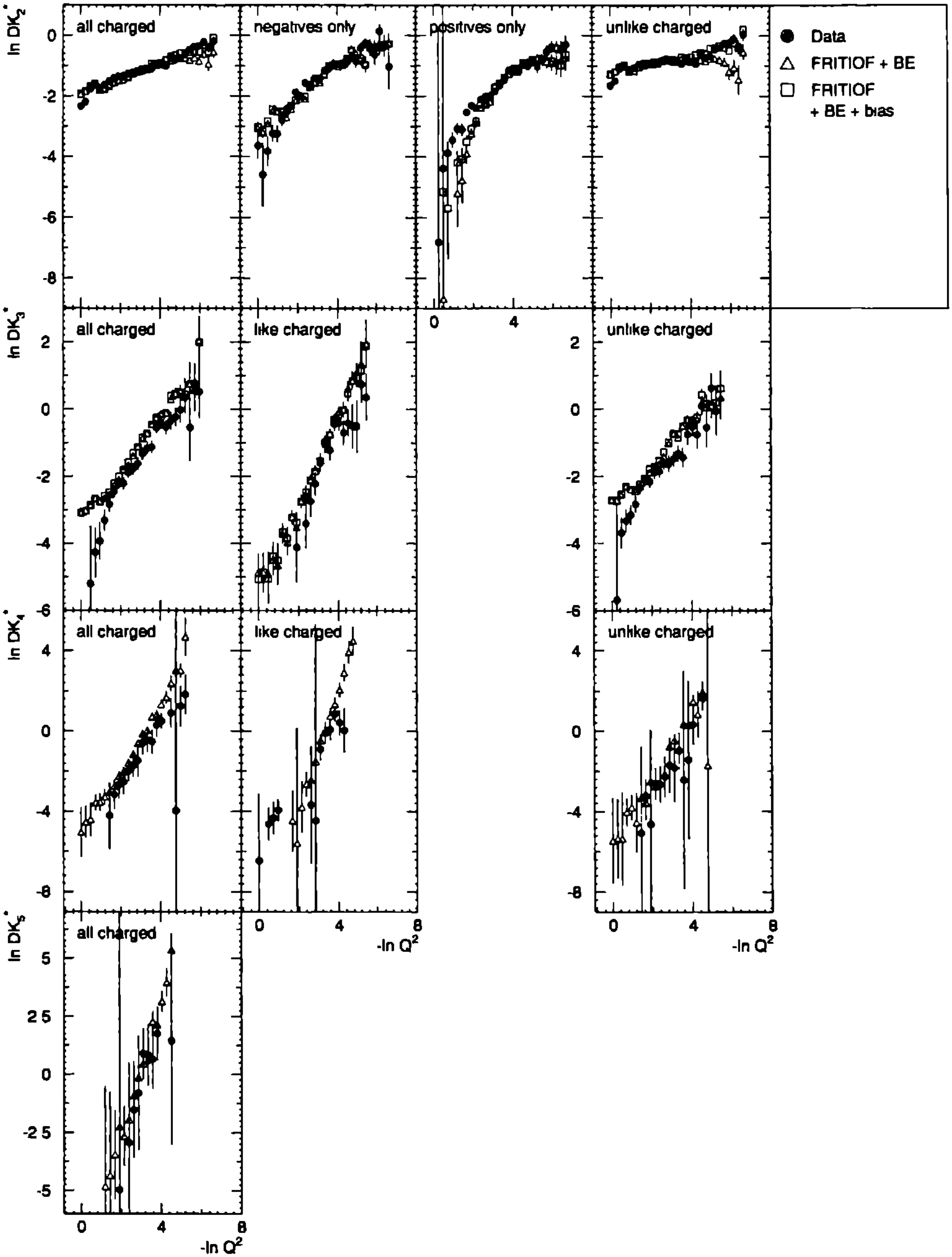

Figure 5.23: *The differential star integral cumulants in terms of Q^2 compared with FRITIOF2.0 + BE and with FRITIOF2.0 + BE + a bias accounting for Dalitz decay and undetected γ-conversions (for $q \leq 3$).*

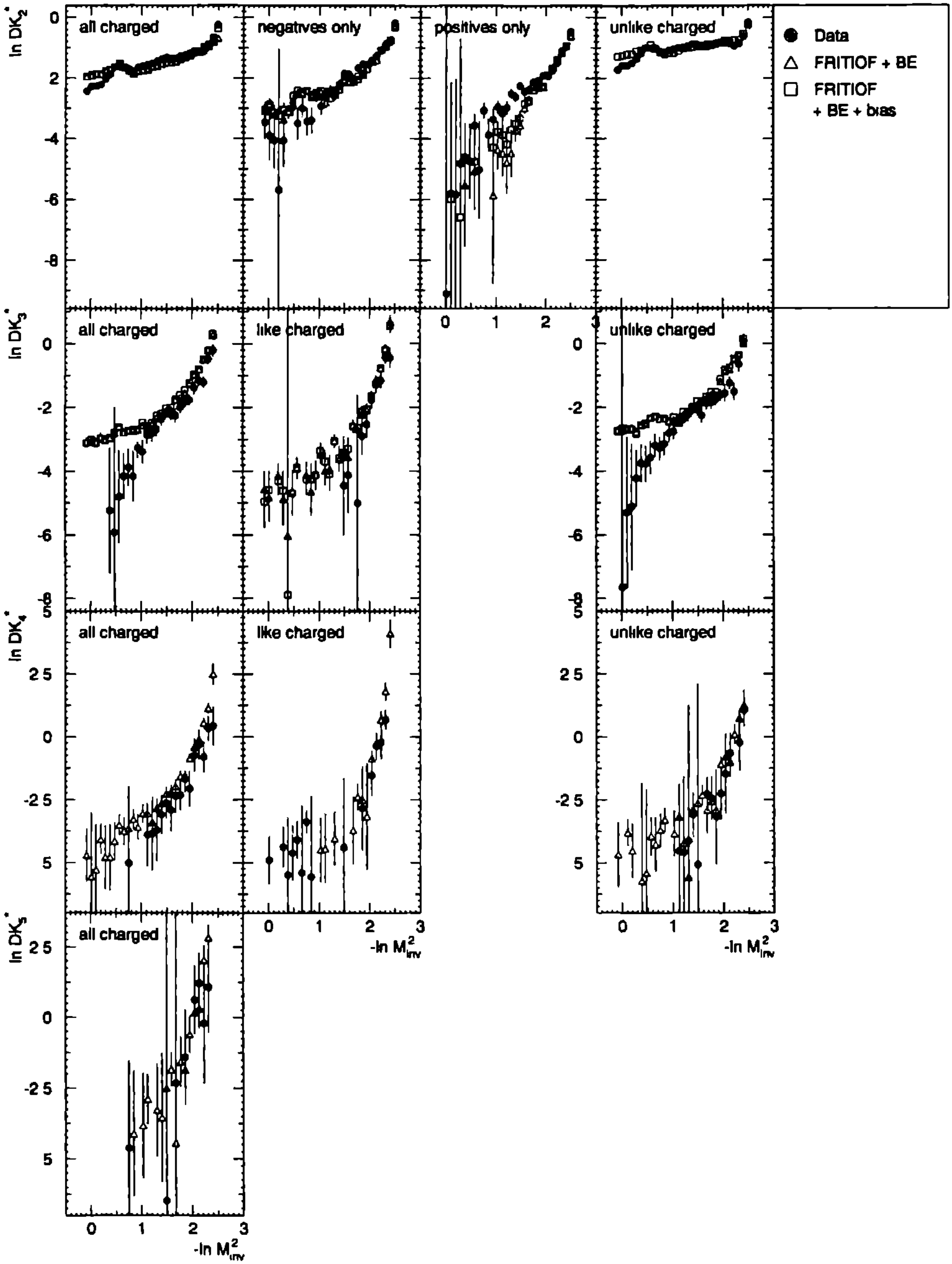

Figure 5.24: *The differential star integral cumulants in terms of M^2_{inv} compared with FRITIOF2.0 + BE and with FRITIOF2.0 + BE + a bias accounting for Dalitz decay and undetected γ-conversions (for $q \le 3$).*

tend to curve downwards.

As is the case for the F_q^*, also the K_q^* are strongly correlated at different Q^2 (M_{inv}^2) values. The differential versions are shown in Figs. 5.23 and 5.24 in terms of Q^2 and M_{inv}^2, respectively. The $\ln DK_2^*(--)$ and $\ln DK_2^*(++)$ exhibit an approximate linear increase with $-\ln M_{inv}^2$. For unlike-charged combinations DK_2 is almost constant, except for the ρ-signal. For third order the behavior of $DK_q(\pm,\pm,\pm)$ with decreasing M_{inv}^2 is consistent with a power law. One should, however, be careful with strong statements since only a few data points are available and some of them have very large errors.

Historically speaking, it should be noted that another differential form of the density integral technique was introduced and used a long time ago by Berger et al. [EBER77, GTHO77] in a study of the invariant-mass dependence of the two-pion inclusive correlation function. Using data from a 205 GeV/c pp experiment at FNAL, these authors have shown that the $(+-)$ and $(--)$ correlation function is significantly different from zero only for invariant masses below 1.5 and 0.6 GeV/c^2, respectively. Moreover, at small invariant mass, the differential second-order cumulants $DK_2^D(+-)$ and $DK_2^D(--)$ show power-law behavior in M_{inv}^2, with

$$\frac{DK_2^D(--)}{DK_2^D(+-)} \propto \left(\frac{1}{M_{inv}^2}\right) \tag{5.73}$$

The results were interpreted in the Mueller-Regge picture as well as in an "exclusive" picture, where most of the correlation in the threshold region is explained from resonance decays into three or more pions [GTHO77].

These early results agree qualitatively and quantitatively with the data presented here and confirm that the strong rise of density integrals with decreasing Q^2 (M_{inv}^2) must be attributed to like-charged pion effects, an obvious candidate being a low-mass enhancement caused by B.E. symmetrization. The latter conclusion may support the view recently developed in [ABIA92]. There, intermittency is explained from Bose-Einstein correlations between (like-charged) pions with the power-law behavior obtained from fluctuations in the size and/or the shape of the source. This latter effect can be explained e.g. from the self-organized criticality of parton-avalanches. Though at this moment only speculative, it is an interesting new view. It explaines intermittency as a final-state interaction.

5.4 Conclusions

- The density integrals make use of the available statistics in an optimal way and avoid the artificial splitting of dense particle groups. This results in reduced errors and smaller fluctuations in comparison with the factorial moments. Moreover, analyses in terms of Lorentz-invariant variables such as Q^2 and M_{inv}^2 are possible.

- An evaluation of the GHP-integral in a restricted Q^2-region (0.027 GeV^2 $\leq Q^2 \leq$ 1 GeV^2) for different charge combinations yields intermittency indices a factor 1.2 (ϕ_5) to 1.6 (ϕ_2) larger for the negatives-only sample than for the all-charged sample.

  Investigating the p_T-dependence for the different charge combinations learns that the results earlier obtained for the all-charged rapidity analysis are somewhat misleading due to their uncompleteness. One cannot claim that the intermittency effect is stronger for low-p_T particles.

The Ochs-Wosiek relation is obeyed within errors in the full region considered (0.027 GeV$^2 \leq Q^2 \leq 1$ GeV^2). The Lévy index μ and the Ginzburg-Landau parameter ν, determined from the slopes in the Ochs-Wosiek plot, are both incompatible with a second-order phase transition.

The Monte-Carlo model FRITIOF2.0 + BE describes the second-order GHP-integral for the negatives-only sample qualitatively well. For the unlike-charged pairs, a bias accounting for Dalitz decay and undetected γ-conversions has to be incorporated into the model in order to reproduce the increase of $\ln F_2^{GHP}$ with $-\ln Q^2$ observed for the data. The increase of the higher orders (all charged and negatives only) is overestimated by FRITIOF2.0 + BE.

It is not possible to determine whether Bose-Einstein correlations are Gaussian or power law from the behavior of the GHP-integral as function of Q^2 for like-charged pairs. In the region where a Gaussian and a power-law fit can be distinguished (10^{-3}GeV$^2 \leq Q^2 \leq 6 \times 10^{-3}$), the statistical errors on the data points are too large to make a strong statement. The power-law fit, however, yields the smallest χ^2.

- The star integral provides a convenient algorithm for the determination of cumulants and differential cumulants. Genuine multiparticle correlations are established up to fifth order for all-charged combinations and up to fourth order for like-charged and unlike-charged combinations. They increase with decreasing Q^2 and M_{inv}^2 and show a strong dependence on the charge combination. The correlations are dominated by like-charge correlations, presumably Bose-Einstein correlations.

  The four quantities F_q^*, DF_q^*, K_q^*, DK_q^* reveal different discrepancies between the FRITIOF2.0 + BE (+ bias) predictions and the data. However, apart from some overestimation of the orders $q \geq 3$, the FRITIOF predictions are generally rather satisfactory.

Bibliography

[ABIA92] A. Białas, Nucl. Phys. **A545** (1992) 285.
A. Białas, Acta Phys. Pol. **B23** (1992) 561.

[EBER77] E. Berger et al, Phys. Rev.**D15** (1977) 206.

[EDWP92] E.A. De Wolf, Proc. XXII Int. Symp. on Multiparticle Dynamics, Santiago de Compostela, Spain, July 1992, edt. C. Pajares, (World Scientific, Singapore 1993) p.263.

[FBTH92] F. Botterweck, Ph.D. Thesis, Univ. of Nijmegen (1992).

[IDRE88] I. Dremin, Mod. Phys. Lett. **A3** (1988) 1333.

[IDRE89] I. Dremin, Mod. Phys. Lett. **A5** (1989) 1072.

[MGYU92] M. Gyulassy: Festschrift L. Van Hove, A. Giovannini and W. Kittel (eds.), P.479, Singapore: World Sientific 1992.

[NA2294] I. Ajinenko et al. (NA22), Invariant Mass Dependence of Particle Correlations in π^+p and K^+p Interactions at 250 GeV/c, IIHE-93.05.

[NA22BE] M. Adamus et al. (NA22), Z. Phys. **C37** (1988) 347,
N. Agababyan et al. (NA22), Z. Phys. **C59** (1993) 195.

[NA35PC] G. Jancso, private communication.

[GHP283] P. Grassberger, Phys. Lett. **A97** (1983) 227.
H. Hentschel and I. Procaccia, Physica **D8** (1983) 435.

[GTHO77] G.H. Thomas, Phys. Rev. **D15** (1977) 2636.

[PCAR91] P. Carruthers, Ap J. **380** (1991) 24.

[PLHE92] P. Lipa et al., Phys. Lett. **B285** (1992) 300.

[PLHE93a] H. Eggers et al., Phys. Lett. **B301** (1993) 298.

[PLHE93b] H. Eggers et al., Phys. Rev. **D48** (1993) 2040.

[PLHE94] H. Eggers and P. Lipa, Unbiased estimators for correlation measurements, TPR-93-22, AZPH-TH/93-22, HEPHY-PUB-600/93.

[UA1B92] B. Buschbeck et al. (UA1-MB): Proc. XXII Int. Symp. on Multiparticle Dynamics, Santiago de Compostela, Spain, July 1992, edt. C. Pajares, (World Scientific, Singapore 1993) p.246.

6

Summary

After the discovery of events with a group of particles densely clustered in (pseudo)rapidity (so-called spike events), both theoreticians and experimentalists had very ambitious ideals. A search for "new physics", which was supposed to explain the occurrence of spike events, started. Factorial moments were expected to exhibit strict power laws when analyzed in (pseudo)rapidity bins of decreasing size. This behavior of the factorial moments was the definition of intermittency as given by Białas and Peschanski. It would be the reflection of self-similarity in the multiparticle production process. Later on intermittency acquired a broader meaning and referred to the increase of factorial moments with decreasing phase-space intervals. Along with factorial moments, some other quantities like factorial cumulant moments, factorial correlators and G-moments were examined.

For factorial moments, the power law is valid only approximately and in a restricted region of rapidity-bin sizes. Factorial moments, probing density fluctuations, contain contributions of lower-order correlations. Genuine multiparticle correlations can be measured via the factorial cumulant moments. Unfortunately, they are dominated by large errors and one can only state that their behavior with decreasing bin sizes is not inconsistent with a power law. The factorial correlators, measuring the correlation between density fluctuations in two non-overlapping bins within one event, are independent of the bin size and increase with decreasing bin distance. They do not obey a power law. With the technique of G-moments, one aimed at revealing the multifractal properties of the multiparticle process. Their behavior is, however, dominated by statistical noise and no information can be gained from them at present energies.

The one-dimensional intermittency analysis turns out to be far from satisfactory. Soon it was realized that, if present, self-similarity in the multiparticle production process would naturally occur in three dimensions. Model calculations, performed by Ochs, Wosiek, Białas and Seixas, confirmed the suspicion that investigations of the factorial moments in one- and two-dimensional phase spaces lead to deviations from a power-law behavior (so-called projection effect). Indeed, also in two-dimensional analyses of the data, the factorial moments still bend over when evaluated as function of decreasing phase-space cells. However, in three dimensions, they show an upward curvature. This behavior of the factorial moments revived the interest in the factorial cumulant moments, despite the large errors. For orders larger than two, their behavior is consistent with a power law. The second-order factorial cumulant moment increases faster than a power law. Fiałkoski then proposed to add a constant to the power law to take into account possible non-singular long-range correlations. This modified parametrization describes the behavior of the second-order factorial cumulant moment very well. Moreover, the power turns out to be independent of the process. Intermittency might be a final-state interaction.

Although the factorial moments do not exhibit the originally suggested power-law behavior, they follow the modified power law proposed by Ochs and Wosiek. This law can be rewritten as a linear dependence of the logarithm of the higher-order factorial moments on the logarithm of the second-order factorial moment. The slopes serve as input for the determination of the Lévy index and the Ginzburg-Landau parameter, which characterize the process involved. The values found exclude a second-order phase transition.

Factorial moments and especially factorial cumulant moments suffer from low statistics and artificial binning inherent to the method. In order to use the available statistics in an optimal way and to avoid the artificial binning, Carruthers introduced a new tool, called density integrals. Due to the particular formalism, the correlation analysis can now be performed in terms of the four-momentum difference squared and the invariant mass squared of groups of particles. Furthermore, it is possible to investigate the dependence of the correlations on the charge combination of the q-tuple. From this analysis it becomes clear that the increase of factorial moments, or generally of correlations, with decreasing phase-space volume is essentially due to correlations between like-charged particles. A probable candidate for these like-sign correlations is the Bose-Einstein interference, a final-state interaction among like-charged pions. Conventionally, Bose-Einstein correlations are fitted by a Gaussian in four-momentum difference, but it turns out they can alternatively be parametrized by a power law in four-momentum difference squared.

All data are compared with model predictions of FRITIOF version 2.0. Without the inclusion of Bose-Einstein correlations, FRITIOF is not able to reproduce the data. When Bose-Einstein correlations are added, the agreement with the data varies from bad to satisfactory, depending on the quantity and the phase-space variable(s) in which the analysis is performed. However, one should be careful with claiming that the discrepancies between the FRITIOF predictions and the data are due to "new physics". The fact is that FRITIOF exhibits some defects. The overproduction of some resonances, e.g., is a problem that cannot be solved solely by adjusting some model parameters. Experts, working on the model, state that the experimentally observed amount of resonances is inconsistent with some first principles of the model. Bose-Einstein correlations are an other problem to deal with. The algorithm used in the model only considers two-particle interactions. The inclusion of higher-order particle correlations is certainly necessary. After the elimination of these defects, one can try to determine if "new physics" is needed to explain the observed behavior of multiparticle correlations.

Intermittency investigations slowly changed from a search for perfect power-law behavior to general correlation studies. One of the greatest merits of the intermittency studies is the development of tools very well suited for a systematic approach to correlation phenomena and for confronting models with data.

Samenvatting

Na de ontdekking van gebeurtenissen waarbij een groep deeltjes in een zeer nauw (pseudo-) rapiditeitsinterval geproduceerd werd, hadden zowel theoretici als experimentatoren hoge idealen. Er startte een zoektocht naar "nieuwe fysica" die hun noodzakelijk scheen om de aanwezigheid van deze "spike events" te verklaren. Men veronderstelde dat factoriële momenten zouden stijgen volgens een strikte machtswet als ze bepaald werden voor steeds kleinere (pseudo)rapiditeitsintervallen. Dit gedrag werd door Białas en Peschanski intermittentie genoemd en zou de reflectie zijn van zelfgelijkenis in het veeldeeltjesproductieproces. In de loop der tijd werd de definitie van intermittentie versoepeld en de term verwees naar de stijging van de factoriële momenten met dalende grootte van de faseruimtecellen. Tegelijk met de factoriële momenten werden ook enkele andere grootheden, zoals factoriële cumulantmomenten, factoriële correlatoren en G-momenten, bestudeerd.

De machtswet blijkt voor de factoriële momenten enkel bij benadering geldig en wordt bovendien enkel in een beperkt gebied van rapiditeitsintervalgrootten waargenomen. Factoriële momenten peilen de dichtheidsfluctuaties, zodoende bevatten zij bijdragen van correlaties van lagere orde. De pure veeldeeltjescorrelaties kunnen gemeten worden met behulp van de factoriële cumulantmomenten. Jammer genoeg worden dezen gedomineerd door grote fouten. Men kan enkel vaststellen dat hun gedrag niet inconsistent is met een machtswetgedrag. De factoriële correlatoren meten de correlatie tussen dichtheidsfluctuaties in twee gescheiden intervallen binnen een enkele gebeurtenis. De factoriële correlatoren blijken onafhankelijk te zijn van de grootte van de intervallen en te stijgen als de afstand tussen de intervallen daalt. Met de techniek van de G-momenten hoopte men de multifractale eigenschappen van het veeldeeltjesproductieproces bloot te leggen. In de praktijk wordt het gedrag van de G-momenten echter gedomineerd door statistische ruis en leveren ze bij de huidige energieën geen bruikbare informatie op.

De eendimensionale intermittentieanalyse is alles behalve bevredigend. Vrij vlug realiseerde men zich dat indien zelfgelijkenis aanwezig is in het veeldeeltjesproductieproces, dit zich zal manifesteren in drie dimensies. Modelberekeningen, uitgevoerd door Ochs, Wosiek, Białas en Seixas, bevestigden het vermoeden dat analyses van factoriële momenten in een- of tweedimensionale faseruimten een verstoord machtswetgedrag opleveren. Deze afwijking wordt het projectieëffect genoemd. In de tweedimensionale analyses van de experimentele gegevens vindt men inderdaad dat de factoriële momenten naar beneden buigen als ze geëvalueerd worden als functie van verkleinende faseruimtecellen. De driedimensionele factoriële momenten stijgen echter sterker dan een machtswet. Dit gedrag deed de interesse in de factoriële cumulantmomenten herleven. Voor orden groter dan twee is hun gedrag consistent met een machtswet. Voor tweede orde is de stijging echter sterker dan een machtswet. Fiałkowski interpreteerde dit als zijnde het gevolg van niet-singuliere langeafstandscorrelaties, die eenvoudig in rekening te brengen zijn door aan de machtswet een constante term toe te voegen. Met deze aangepaste parametrisatie zijn de cumulantmomenten van tweede orde inderdaad zeer goed te beschrijven. Daarbij blijkt dat de macht onafhankelijk is van het proces. Dit suggereert dat intermittentie een eindtoestandsinteractie zou kunnen zijn.

Hoewel de factoriële momenten niet het oorspronkelijk gesuggereerde machtswetgedrag vertonen, volgen ze wel de gemodificeerde machtswet voorgesteld door Ochs en Wosiek. Deze wet kan herschreven worden als een lineaire afhankelijkheid van het logaritme van de factoriële momenten van hogere orde als functie van het logaritme van het factoriëel moment van tweede orde. De richtingscoëfficiënten werden gebruikt om de Lévy index en de Ginzburg-Landau parameter te bepalen. Deze getallen kenmerken het betrokken proces. De gevonden waarden sluiten een faseovergang van tweede orde uit.

De factoriële momenten en vooral de factoriële cumulantmomenten gaan gebukt onder lage statistiek en kunstmatige onderverdeling van het oorspronkelijke interval. Om de voorradige statistiek optimaal te kunnen gebruiken en om de kunstmatige onderverdeling te vermijden, introduceerde Carruthers een nieuwe grootheid, genaamd dichtheidsintegraal. Met deze grootheid is het mogelijk om de correlatieanalyse uit te voeren in termen van viermomentumverschil en invariante massa. Bovendien kan de ladingsafhankelijkheid van de correlaties onderzocht worden. Deze analyse toont aan dat de stijging van factoriële momenten, of van correlaties in het algemeen, bij verkleining van de faseruimte vooral veroorzaakt wordt door correlaties tussen deeltjes met gelijke lading. Een waarschijnlijke kandidaat hiervoor zijn de Bose-Einstein correlaties, dit is een eindtoestandsinteractie tussen pionen met gelijke lading. Bose-Einstein correlaties worden conventioneel gefit met een Gaussische functie in het viermomentumverschil Q, maar het blijkt dat een machtswet in Q^2 een acceptabel alternatief is.

Alle data zijn vergeleken met voorspellingen van het FRITIOF model, versie 2.0. Dit model is niet in staat om de data te reproduceren. Een gemodificeerde versie met Bose-Einstein correlaties beschrijft de data variërend van slecht tot bevredigend, al naar gelang de beschouwde grootheid en de faseruimteverandelijke(n) waarvoor de analyse wordt uitgevoerd. Men kan echter niet zomaar beweren dat de verschillen tussen de FRITIOF voorspellingen en de data hun oorzaak vinden in "nieuwe fysica". Het feit is dat FRITIOF enkele defecten vertoont, bijvoorbeeld de overproductie van sommige resonanties. Dit probleem kan niet opgelost worden door simpelweg de parameters van het model te veranderen. Experten, die aan het model werken, beweren dat de hoeveelheid resonanties die experimenteel wordt vastgesteld, niet consistent is met enkele fundamentele principes van het model. Ook het algoritme dat de Bose-Einstein correlaties genereert is voor verbetering vatbaar, daar het enkel tweedeeltjesinteracties beschouwt. Het insluiten van correlaties van hogere orde is een absolute noodzaak. Pas als deze gebreken uit FRITIOF verwijderd zijn, kan men proberen te bepalen of er "nieuwe fysica" nodig is om het gedrag van de veeldeeltjescorrelaties te verklaren.

Het intermittentieonderzoek is langzaam geëvolueerd van een speurtocht naar machtswetten naar een meer algemene studie van correlaties. Een van de grootste bijdragen van de intermittentiestudies is de ontwikkeling van instrumenten die geschikt zijn voor een systematisch onderzoek naar correlatiefenomenen en om modellen met data te confronteren.

Curriculum Vitae

Martine Charlet

Zij werd op 27 oktober 1966 geboren te Deurne (België). Aan het Koninklijk Lyceum Antwerpen (thans Koninklijk Atheneum Antwerpen II) behaalde zij achtereenvolgens het getuigschrift lager secundair onderwijs (30 juni 1981) en het getuigschrift hoger secundair onderwijs, optie wiskunde (18 juni 1984).

Op 1 oktober 1984 toog zij naar het Rijksuniversitair Centrum Antwerpen (RUCA), alwaar zij op 9 juli 1987 het kandidaatsdiploma natuurkunde verkreeg. Zij voltooide haar studies aan de Universitaire Instelling Antwerpen (UIA). Op 30 juni 1989 werd haar het licentiaatsdiploma natuurkunde uitgereikt. Onderzoek voor haar licentiaatsverhandeling, getiteld "Multipliciteitsverdelingen in meson-kern interacties in rapiditeitsintervallen", verrichtte ze o.l.v. Prof. Dr. F. Verbeure in de groep "elementaire deeltjes" op de UIA. Op basis van deze verhandeling verscheen een artikel in het wetenschappelijke tijdschrift "Zeitschrift für Physik C".

In afwachting van een EEG beurs volgde zij van 1 oktober 1989 tot 31 december 1989 de bijzondere licentie "Informatica en Bedrijfswiskunde". De eerste vijf maanden van 1990 kon zij d.m.v. een IIKW beurs op de UIA onderzoek verrichten naar Bose-Einstein correlaties en factorial moments in 250 GeV/c K^+ en π^+ interacties op Al en Au.

De EEG beurs werd toegekend voor drie jaar (1 juni 1990 tot 31 mei 1993) en werd gebruikt om aan de Katholieke Universiteit Nijmegen (KUN) in de groep "experimentele hoge energie fysica" analyses uit te voeren in het kader van een doctoraatsthesis.

Op 23 november 1992 werd haar het Dr. I.B.M. Fryestipendium toegekend. Deze prijs wordt jaarlijks uitgereikt aan veelbelovende vrouwelijke doctoraatsstudenten in hun derde jaar. Het stipendium werd geconsummeerd in de USA in de periode van 12 september tot 4 oktober 1993. Daar woonde zij een congres bij (te Aspen, Colorado) en bezocht twee groepen waarmee al eerder, via electronic mail, was samengewerkt (de groep van Prof. R. Hwa aan de University of Oregon in Eugene en de groep van Prof. I. Sarcevic aan de Johns Hopkins University in Baltimore).

Om de gelegenheid te bieden het onderzoek af te ronden en de verkregen resultaten om te zetten in een proefschrift, verlengde de faculteit natuurwetenschappen van de KUN op eigen kosten het contract tot 31 mei 1994. Gedurende dit jaar gaf zij bovendien werkcolleges kernfysica en structuur der materie.